ANTHROBOTS: SELF-CONSTRUCTING LIVING ARCHITECTURES BY DESIGN

A dissertation
submitted by

Gizem Gumuskaya

In partial fulfillment of the requirements
for the degree of

Doctor of Philosophy

in

Biology

TUFTS UNIVERSITY

February 2024

Advisor: Michael Levin, Ph.D.

Abstract

Biological structures encode target shape not in the form of descriptive blueprints (static instructions) like those that human architects and engineers use, but rather in the form of generative rules (if-then statements) that are dynamically called upon based on different inputs to the system during the developmental process. This distinction is important because it is not only the existential dichotomy between top-down (e.g., human-constructed architectures of culture) vs. bottom up (e.g., self-constructing architectures of nature) fabrication; but is also the fundamental mechanism by which morphogenetic plasticity arises in nature. Because biological form develops as a result of a series of embodied if-then rules guiding the morphogenetic process down a specific developmental path, in this Dissertation I hypothesize that for any given biological system, there could be other branches of the if-then tree, adjacent to the beaten path of the default morphology. These alternative developmental paths may be accessible by providing the system with non-default inputs, thereby invoking radical morphological reconfiguration towards alternate anatomies. Tuning of the environmental system inputs in this way (while keeping the genome wild type) and steering the developmental process into previously unexplored latent branches may lead to the exploration of novel stable synthetic morphologies inherent in the biological system itself, all without performing direct genetic editing. To illustrate this approach, here we demonstrate that normal, non-genetically modified human tracheal cells can be induced to form a new morphology by design - Anthrobots - which exhibit spontaneous behavior, swimming around in one of several patterns, demonstrating plasticity for novel form and function

inherent in even elderly human somatic cells. Moreover, Anthrobots are able to traverse over cultured neurons, settling down and causing repair under them: the nerves knit together across the wound gap due to the presence of the Anthrobot. A patient's own cells can be harnessed to make a motile biological robot that can traverse human tissue and induce repair. In the future, this platform can deliver pro-regenerative therapeutics for a range of biomedical applications that will not trigger rejection or require immune suppression.

Acknowledgements

“You cannot swim for new horizons until you have courage to lose sight of the shore,” said American writer William Faulkner who won the 1949 Nobel Prize for Literature. I had this quote on a small post-it note hung up at my office desk for many years, to help me remember the importance of continuing to follow your dreams, even if -or especially when- you are not sure if the path will lead you where you think it will. This is already a familiar feeling in the scientific process, wherein by definition we are striving for something that has never been accomplished before. It becomes even more prominent if you decide to forge a new path altogether by combining seemingly distant disciplines, such as, in my case, architecture and biology. Taking more considerable risks does mean having to take more responsibility, hence having to work extra hard; but in retrospect, beyond risk-taking and hardworking, what really has helped me forge this new path forward were the humans in my life who supported me along the way.

First and foremost, I would like to thank my PhD advisor Prof. Michael Levin for believing in me and giving me the freedom and opportunity to forge this unconventional path in the synthetic morphogenesis space rigorously. When I began exploring synthetic biology as an architect eight years ago, doing a PhD in Biology was the last thing I thought I could do because I was worried that this would mean having to leave behind my identity as a designer and mold into a traditional scientist role. At the same time, I really did want to get under the hood and into the weeds of biology to genuinely try to understand the cruxes of the morphogenetic code and how living architectures develop in nature, so we could start growing them toward novel designs devised by us. The only way I could have pursued a PhD in Biology while maintaining my background and perspective as a designer was to do this with a PhD advisor who themselves can think

across many disciplines and scales at once, go after questions that no one else would even begin think about for many decades to come, and have the knowledge and courage to wrestle them meticulously. For me, this advisor was Mike, and I am deeply grateful for his guidance and confidence throughout what has been the most challenging and rewarding journey of my life so far.

During this time, another crucial source of support for me has been my PhD committee members Prof. Kelly McLaughlin and Prof. Barry Trimmer, as well as my external committee member Prof. Leonardo Morsut. I am grateful for their open-mindedness, encouragement, and help with navigating the twists and turns of a PhD. All three of them are not only pioneers in their respective fields but they were also able to extend their expertise into the transdisciplinary domain to relate and support my vision. I count myself very fortunate to have had the opportunity to receive the guidance of such inspirational academics. I would also like to thank Profs Ron Weiss and George Stiny, who were the co-advisors of my dual master's thesis at MIT where I first started exploring the intersection of architecture and biology, for their continued mentorship and encouragement to continue forging this path through a PhD in Biology.

Next, I would like to thank all my fellow Levin Lab members, especially Drs Douglas Blackiston, Santosh Manicka, Juanita Matthews, Franz Kuchling, Devon Davidian, Vaibhav Pai, and Patrick McMillen, as well as Julia Poirier, Jayati Mandal, Rakela Colón, Anna Kane, Joshua Finkelstein, Emma Taddeo for all their support during the last five years. I would like to further extend my appreciation to my co-authors on the first Anthrobots paper Pranjal Srivastava, Ben Cooper, Hannah Lesser, and Ben Semegran, as well as our supporting PI Prof. Simon Garnier from NJIT. When I created my first Anthrobot in September of 2019, the first emotion, after a brief moment of

ecstasy, was sheer panic—there were so many of them (Anthrobots), all in different shapes, sizes, and motility patterns. How was I ever going to sort through this variety and diversity to arrive at a coherent understanding and representation of Anthrobots? The following six months where I continued to work alone proved that this was not just a transient feeling at the moment, but an actual need to finally form a team to help scale up production and further explore the implications and applications of Anthrobots. I couldn't have asked for a more intelligent and diligent team to co-create our first paper.

Additionally, even though the two follow-up papers on Anthrobots that will be published in 2024 are not technically a part of this dissertation, I would still like to acknowledge and thank my extended team and co-authors in those publications as well: Nikolai Davey, Zoe Weiner, Serena Meng, Cindy Zhu, Andrew Bender, Douglas Hazel, as well as my collaborators Caitlin Grasso, Piper Welch, and Prof. Josh Bongard. It has been such a pleasure to work with this brilliant and inspiring group of people.

Next, I would like to thank all my amazing and inspiring fellow scientist, engineer, artist, designer, maker friends and mentors whom I met across different graduate school chapters of mine. Although too many to name here individually, I appreciate all of you as you supported and inspired me with many great conversations throughout the years. I would specifically like to thank my best friend and partner Steven Hyde, as well as the rest of Hyde and Smith families, for cheering me on along the way and at the finish line.

Finally, I would like to thank my loving parents Hayrettin and Betul Gumuskaya, my wonderful siblings Eren and Merve (Mavi) Gumuskaya, my dear brother-in-law Anil Mavi, as well as the extended Gumuskaya and Alinca families for their endless confidence and belief in me. Thank you all sincerely!

Table of Contents

List of Figures

List of Abbreviations

NMJs	Neuromuscular Junctions
NHBE	Normal Human Bronchial Epithelial (cells)
ALI	Air-liquid-interface
RSPO2	R-Spondin-2
ECM	Extra Cellular Matrix
ICC/IF	Immunocytochemistry / Immunofluorescence
ZO-1	Zonula Occludens-1
DAPI	4’,6-diamidino-2-phenylindole
PCA	Principle Component Analysis
hiNSCs	Human induced Neural Stem Cells
PDMS	polydimethylsiloxane
Tuj1	Beta III Tubulin
HEK	Human Embryonic Kidney (cells)
BEGM	Bronchial Epithelial Growth Medium
DMEM	Dulbecco’s Modified Eagle Medium
RA	Retinoic Acid
D-PBS	Dulbecco’s Phosphate Buffered Saline
PBS	Phosphate Buffered Saline
BSA	Bovine Serum Albumin
FLIM	Fluorescence Lifetime Imaging Microscopy
LIF	Laser Induced Fluorescence
MEF	Mouse Embryonic Fibroblast
FBS	Fetal Bovine Serum
KOSR	KnockOut Serum Replacement
PDL	Poly-d-lysine

Summary of Chapters

Chapter 1 introduces perspectives on engineering biological structures towards designed ends. It discusses the dichotomy between bottom-up self-construction in biology vs the top-down building activities of human-made structures and argues that by bringing together these two seemingly contradictory approaches, we may be able to pave the way for building self-constructing living architectures by design.

Chapter 2 details the experiments for testing the specific hypothesis of whether guiding the WT chassis Normal Human Bronchial Epithelial (NHBE) cells through the morphogenetic functions of self-construction (monoclonal expansion, proliferation, differentiation) and mechanical eversion will enable it to become a self-constructing, cilia out, motile organism, i.e., Anthrobot. This chapter also includes the morphological and behavioral characterization and correlation experiments conducted on Anthrobots. This chapter further elaborates on the neuronal traversal and healing experiments conducted with the Anthrobots.

Chapter 3 introduces a study that offers perspectives for how exploiting morphogenetic plasticity may constitute an alternative but complementary approach to the genetic circuit mediated approaches for synthetic morphogenesis. It offers a methodical approach through the construction of morphospatial landscape and discusses Anthrobots as a proof-of-concept embodiment of this alternative approach for creating synthetic multicellular constructs.

Chapter 4 revisits the concept of self-organization by design established in the first chapter under the light of the advances introduced in this Dissertation. It offers

perspectives for future direction and work towards building self-constructing living architectures by design.

Contributions

Research and experimental work introduced in this Dissertation was conducted in Tufts University Department of Biology Levin Laboratory. The experimental design, methods, and protocols for producing Anthrobots introduced in Chapter 2 were developed by Gizem Gumuskaya under the advisement of Prof. Michael Levin.

Upon the establishment of these protocols, sample collection for the morphological and behavioral analyses of 400 Anthrobots (in the form of confocal imaging of immunological stains and timelapse microscopy videos) were conducted by Gizem with the help in part-time capacity of Levin Lab technician Ben Cooper. Tracking of these timelapse videos using the TrackR software was carried out by Gizem and two undergraduate students in Biology trained and supervised by her: Benjamin Semegran and Hannah Lesser. Analysis of data collected from the confocal imaging and timelapse tracking were analyzed by a classification pipeline developed by Prof. Simon Garnier (NJIT), Gizem, as well as an undergraduate student supervised by Simon and Gizem together: Pranjal Srivastava. For the neuronal traversal and healing work, experimental design was developed by Gizem Gumuskaya and Prof. Michael Levin. For the data collection of replicates towards increasing the Ns, the help of Ben Cooper, Hannah Lesser, and Benjamin Semegran was additionally enlisted. All these contributors are listed as co-authors in the paper entitled “Motile Living Biobots Self-Construct from Adult

Human Somatic Progenitor Seed Cells” that has been published in the journal *Advanced Science*.

Additionally, I would like to acknowledge Santosh Manicka for his technical input on Multivariate Classification, as well as Profs Roger Kamm and David Kaplan for the discussions on in-vitro tissue-bot interactions. Furthermore, for the supplemental portion of this work also detailed in Chapter 2, I would like to acknowledge the contributions of Benjamin Sweigart to the statistical analysis of change in motility as a function of varying starting seeding conditions, and that of Nik Davey to the imaging and cell culture technical assistance. Finally, I would like to also thank Douglas Blackiston, Joshua Bongard, Caitlin Grasso and Sam Kriegman for high-level scientific discussions on the biobots field, Cindy Zhu, Zoe Weiner, and Serena Meng for image acquisition automation and processing help, and Julia Poirier for helpful comments on the manuscript.

Finally, perspectives introduced in Chapter 3 were developed by Gizem Gumuskaya, under the advisement of Prof. Michael Levin, and are currently under preparation for preprinting, following the publication of the Advanced Science paper.

CHAPTER I

Self-constructing Living Architectures by Design

“Even a brick wants to be something.”

Architect Louis Kahn, 1973

Construction in nature is a self-organizing process governed by a set of building rules embodied within the builders themselves (cells, termites, wasps...) that unfold as these builders interact with one another and their environment. Furthermore, these builders can self-replicate, and in the process, they propagate these embodied construction rules to their progeny, facilitating the bottom-up self-construction of the biological architectures we see in and around us through an unmatched sophistication of decentralized control, spatial computation, and material composition.

Take, for example, the development of an embryo from that initial single "seed" cell. Within its merely ten microns-wide nucleus, this initial building block of the embryo encapsulates a two meters-long DNA strand, where physically encoded are the instructions required to build a dynamic, multicellular living structure with massively complex structural, functional, and material properties.

This seemingly magical structural fabrication in nature is in stark contrast to the traditional construction methods humans have been using for millennia to build diverse architectures, from the primitive hut to the New York skyline. Beyond this ability to self-construct by replicating and orchestrating their building blocks into target morphologies, biological structures can also heal back to that target morphology in the face of damage. They can do real-time spatial computation and respond with embodied intelligence. Most importantly, they have a negative carbon footprint. None of these astounding features are found in human-made structures, despite our discipline of architecture being thousands of years old. Enchanted by this dichotomy between bottom-up vs top-down construction in nature vs culture, I began taking a closer look at how these self-construction processes unfold in nature and came to the transformative understanding that beneath nature's magic, there is in fact a tremendous amount of logic. Furthermore, we now may be able to engineer this underlying logical framework, through the tools of synthetic morphogenesis, and thereby harness nature as a rational design medium for architecture. In other words, we are now at this unprecedented, exciting point where, for the first time in history, as architects, we might be able to import the unique features of living biological structures into human-made architectures. To do this, we need to speak the language of morphogenesis and "convince" biological tissues to grow themselves into completely novel forms: ones designed by us.

This realization has forever changed my path as an architect and designer, and it is the reason why I decided to pursue my PhD in Biology. I recognized that to explore and forge this next design frontier, a rigorous, knowledge-driven, and meaningful juxtaposition of architecture and biology is critical, for only then we can truly combine

the best of both worlds: top-down goal-orientation of architectural design, and bottom-up autonomous magic of biology.

Motivated by developing self-constructing living architectures by design, I first began exploring the question of how to use the principles of human-developed top-down design to steer natural biological self-construction processes towards rationally devised ends through the deployment of genetic circuits. In my synthetic biology research prior to the PhD, my methodical focus for accomplishing synthetic morphogenesis was through encoding the instructions needed to arrive at the final architecture in traditional genetic circuits that can be booted in living cells. I refer the reader to my dual master's thesis for more details on this method of synthetic morphogenesis[1]. In my PhD research, I decided to develop a different but complementary approach: synthetic morphogenesis through leveraging anatomical tissue plasticity, without the use of any exogenous genetic circuits. This Dissertation will introduce this latter design approach.

To investigate and illustrate this novel approach to synthetic morphogenesis, I developed a novel biological architecture, a new type of programmable anatomy (i.e., biobot) that that we termed "Anthrobot" in reference to its human cellular origin. Anthrobots are the first self-constructing, living, functional, synthetic biological architectures by design. Each Anthrobot builds itself from a single human cell (in 14 days) into one of several different morphological configurations, and accordingly assumes one of several different motility patterns, facilitated by hair-like locomotive appendages on their surface. Anthrobots can be created from a patient's own cells, without having to perform genetic editing. To explore the self-organizing plasticity of

morphogenesis without genomic change and to yield ciliated motile spheroids, which was the example target functionality and morphology aimed at Anthrobots, I started out by selecting an existing biological system in which triggering of such outcome is the most likely: adult, somatic, human airway tissues. To study and steer the in vitro morphogenesis of this existing biological system into synthetic multicellular three-dimensional constructs with cilia facing outward (to obtain significant translocation), I developed a novel protocol that builds upon the existing ability of human bronchial epithelial progenitor cells to form monoclonal spheroids with cilia-lined lumina (i.e., apical-in configuration). I modified this process by manipulating the culture environment such that it now yields cilia-coated (i.e., apical-out) spheroids, which exhibit spontaneous locomotive ability. In this way, I demonstrated a proof-of-concept for how we may be able to access latent developmental abilities waiting to be unlocked in wild-type organisms. In doing so, we discovered two major surprising aspects of these synthetic constructs: first, the resulting morphology and function of Anthrobots displayed a degree of variability and exhibited discrete characters with easily recognizable primary features; and these morphological and functional characters correlated with one another. Second, Anthrobot aggregates into larger structures that can span openings in tissue tears and can help these tissues heal.

In this Dissertation, I start with elaborating on initial wetlab experiments focused on testing the specific hypothesis of whether guiding the WT chassis NHBE through the morphogenetic functions of self-construction (monoclonal expansion, proliferation, differentiation) and mechanical eversion will enable it to become a self-constructing, cilia out, motile organism, i.e., Anthrobot. Then I proceed to explain the morphological

and behavioral characterization and correlation experiments we conducted. This characterization was a key part of this dissertation. This is because upon observing the first Anthrobot in the dish, even though we had accomplished our goal of evoking an alternate developmental path to yield a target anatomy (i.e., a cilia-coated motile spheroid), it was not known whether the resulting behavior would be identical every single time, forming a uniform pool, or whether it would constitute slight changes, forming a continuous distribution, or whether it would fall into a distinct character bin, forming distinct traits. To characterize the morphological and behavioral space to understand developmental and functional features of the resulting synthetic multicellular constructs, we sampled a large population of the resulting anatomies and motility patterns and investigate whether the distribution is uniform, or it displays a continuous gaussian along certain behavioral features, or it consists of specific combinations of these features, hence forming discrete and unique characters. I then proceed to elaborating our follow-up investigations to see whether i) there is a hierarchy between different anatomical features in terms of their impact along the developmental path of these synthetic constructs; ii) there is a correlation between these anatomical traits and the behavioral traits.

Following this essential background characterization of Anthrobots' native capacities, from which future efforts to reprogram form and function will flow, I proceed to describe how we then interfaced synthetic constructs with novel environments to explore their native competencies further. Notably I explain experiments we conducted on identifying novel multicellular interactions between anthrobots and other tissue types that the original tissue Anthrobots derived from (lung epithelium) would not otherwise

interact with, such as cortical neurons. I report on a discovery in this context on how Anthrobots have been able to help gap closure on deformed neuronal tissues.

Finally, I conclude my Dissertation by elaborating on how a systemic exploration of morphogenetic plasticity through a “morphospatial landscape” has the potential to enable a profound paradigm shift in synthetic biology.

CHAPTER II

Anthrobots: Motile Living Biobots Self-Construct from Adult Human Somatic Progenitor Seed Cells

"Every building you see is the image of a [hu]man whom you do not see."

Architect Luis Sullivan, 1918

Abstract

Fundamental knowledge gaps exist with respect to the plasticity of cells from adult soma and the potential diversity of body shape and behavior in living constructs derived from such genetically wild-type cells. Here we introduce Anthrobots, a spheroid-shaped multicellular biological robot (biobot) platform with diameters ranging from 30 to 500 microns. Anthrobots have an inherent capacity for motility in aqueous environments, via cilia covering their surface. Each Anthrobot starts out as a single cell, derived from the adult human lung, and self-constructs into a multicellular motile biobot after having been cultured in extra cellular matrix for 2 weeks and transferred into a minimally viscous habitat. Anthrobots exhibit diverse behaviors with motility patterns ranging from tight loops to straight lines and speeds ranging from 5-50 microns/second. Our anatomical investigations reveal that this behavioral diversity is significantly correlated with their

morphological diversity. Anthrobots can assume morphologies from fully polarized to wholly ciliated bodies with spherical or ellipsoidal shapes, each correlating with a distinct movement type. Anthrobots were found to be capable of traversing in-vitro tissues derived from human cells in various ways. Remarkably, Anthrobots were seen to induce rapid repair of scratches in human neural cell sheets in vitro. By controlling microenvironmental cues in bulk, novel structures, with new and unexpected behavior and biomedically relevant capabilities, can be discovered in morphogenetic processes without direct genetic editing or manual sculpting.

Introduction

What is the latent space of possible functional morphologies that cells, with a wild-type genome, can be coaxed to construct? [2] This question drives at the heart of fundamental issues in evolutionary, developmental, cell, and synthetic biology, and has been taken up by a rapidly growing field focusing on building new kinds of active living structures: biobots [3-7]. This emerging multidisciplinary effort to control the behavior of cellular collectives has garnered much excitement for two main reasons. First, because it offers the possibility of using engineering to reach outcomes that are too complex to micromanage directly, and hence promises to revolutionize efforts to produce complex tissues for clinical applications in regenerative medicine and beyond. Second, increased control over the morphology and behavior of cellular collectives by leveraging morphogenetic tissue plasticity could enable the development of self-constructing living structures by design with predictable and programmable functional properties and numerous practical uses, greatly extending the current abilities of traditional fabrication

practices in diverse fields as robotics [8-25], architecture, sustainable construction, and even space exploration.

In the last decade, interest in developing biological structures *de novo* has seen a rapid surge [26,27]. Among these efforts, a subset of functional biogenic assemblies gave rise to a special class of motile synthetic structures dubbed *biobots*. Early examples of biobots are hybrids between biological cells and inert chemical substances supporting them, such as gels or 3D-printed scaffolds [28-32]. These assemblies incorporated living cells ranging from bacteria to diverse mammalian tissues such as nerve, muscle, and neuromuscular junctions (NMJs), as well as engineered cell lines with programmable features, all carefully crafted into diverse three-dimensional scaffolds designed to harness and amplify the innate functionality of biological cells [33-39].

A different approach resulted in the Xenobots, first fully-biological biobots created by sculpting or molding amphibian embryonic cells into multicellular structures that can spontaneously locomote without external pacing [40-42]. But it was not known how general these phenomena are, whether this kind of plasticity extended to mammals, or what the throughput of this technology can be. Thus, we sought to address whether the capacity of genetically unaltered cells to generate a self-propelled, multicellular living structure in this way is unique to amphibian embryonic cells, and whether such a living structure can be built without needing to be individually sculpted or molded, but instead coaxed to self-construct from an initial seed cell, resulting in a high-throughput process wherein large numbers of biobots can be grown in parallel.

Here, we introduce novel, multicellular, fully biological, self-constructing, motile living structures created out of human lung epithelium. We refer to them as Anthrobots,

in light of their human origin and potential as a biorobotics platform [3,6,7,43]. We quantified their emergent natural, baseline properties as an essential background characterization of their native capacities which will serve as targets for future efforts to reprogram form and function for useful purposes. Anthrobots self-construct in vitro, via a fully scalable method that requires no external form-giving machinery, manual sculpting, or embryonic tissues and produces swarms of biobots in parallel. They move via cilia-driven propulsion [44], living for 45-60 days. We quantitatively characterized the range of movement and morphological types, showing that their behaviors are strongly correlated with specific features of their anatomy. The ability of adult, somatic, human cells to form a novel functional anatomy, with unique behaviors, reveals that this plasticity is not restricted to amphibian or embryonic cell properties, and is a fundamental feature of wild-type cells that requires no direct genetic manipulation to unlock. Furthermore, we found that Anthrobots exhibit a highly surprising behavior given their origin as static airway epithelium: they can move across scratches in (human) neuronal monolayers and induce gap closures across these scratches. Numerous in vitro and in vivo uses of such functional living structures can be envisioned, especially because they can now be made from the patient's own cells [45].

We developed the Anthrobots by leveraging normal human bronchial epithelial cells' native tissue plasticity and unlocked a novel morphology, which is not apparent from the reliable, default developmental patterning of airway epithelium, in order to fulfil target functional and structural needs of creating a self-constructing, multi-cellular, 3-dimensional, motile living structure of human-origin. Airway organoids with apical out tissue organization, yielding ciliated spheroids anatomically similar to the Anthrobots,

have very recently been shown using different protocols [46-48], each starting from individual normal bronchial epithelial cells isolated from airway epithelium extracts. Apical out spheroids made out of intact airway epithelium extracts have also been produced [49]). Each one of these three protocols is optimized for different priorities such as ease of organoid access during its development [48], structural uniformity in final products [46], and ability to easily modulate resulting organoid size [47]. The common denominator between these parallel advances is that they are characterized as organotypic cultures exclusively, enabling scientists to investigate lung anatomy, function, and pathology. Beyond native tissue recapitulation, these constructs' abilities as functional assemblies, range of behavioral and morphological patterns, as well as functional correlations between these patterns have yet to be explored.

These three methods, plus the one detailed in this paper, constitute convergent but distinct technical approaches towards producing the novel morphology of cilia-out spheroids derived from human airway epithelium. These four protocols for creating cilia-covered NHBE-derived spheroids differ in their apical orientation from the earlier established approaches for creating traditional airway organoids where cilia develop as lining the lumen [50]. Boecking & Walentek [48] grow airway organoids as embedded in a collagen-rich matrix (as opposed to the traditional Matrigel approach) and also cultures them in ALI inserts, which have traditionally been used with NHBEs for 2D differentiation into airway epithelium, enabling ease of access to the airway organoids during their developmental course [48]. After this initial ALI culture period of 14 days, the mature airway organoids are dissolved from the collagen matrix and replated into a fresh same matrix of similar composition (to remove catabolites) for another 14 days. It is in this second 14-

day period that cilia localization on the surface is accomplished by administering RSPO2 and Noggin into the matrix. Accordingly, this Boecking & Walentek method consists of two consecutive 2-week periods of matrix-embedded growth and differentiation: first period without and the second period with RSPO2&Noggin.

The method introduced in our paper is most similar to the Boecking & Walentek method in that the initial proliferation of individual NHBEs into spheroids with cilia-lined lumen is accomplished by culturing them as embedded in a gel-based matrix. However, in our method, upon dissolution of spheroids from matrix at the end of this 14-day period, the cilia-in spheroids are not plated back into the matrix, and instead, the cilia localization into the spheroid cortex is achieved by culturing these spheroids in low-adhesive environments. Accordingly, cilia localization is observed within one week, making our method a faster (20 days between single cell to cilia-coated spheroid as opposed to 28), less laborious (single matrix dissolution, as opposed to two), and potentially higher-throughput (since each time matrix is dissolved, a certain percentage of spheroids are lost with it, as is also reported by Boecking & Walentek). The remaining two cilia-out protocols (Stroulios and Wijesekara) are in contrast not leveraging the self-construction ability of NHBEs, and instead form spheroids by means of cell aggregation in U-bottom wells without the presence of a matrix, which in turn provide them with higher regularity of spheroid size (given each spheroid self-assembles with a similar number of constituent cells).

The Stroulios et al method aggregates single cells in low-adhesive micro aggregation chambers first, then transfers them into regular wells for differentiation in matrix-free liquid environment with bronchial epithelial differentiation medium, achieving

uniformity in organoid morphology and size [46]. Similarly, the Wijesekara et al method also first aggregates individual cells into spheroids, and then either transforms them into a matrix environment for differentiation, or keeps them in the liquid environment with bronchial epithelial differentiation medium, both approaches yielding apical-out spheroids with the ability to control the resulting ciliated spheroid size by modulating the initial aggregate size [47,51]. In summary, our method facilitates differentiation as embedded in extracellular matrix, enabling spheroids to self-construct, a feature the other two methods Stroulios and Wijesekara lack; though in turn they achieve higher spheroid regularity and control over spheroid size. The major difference between our method and the Boecking & Walentek method is that upon extraction of apical-in spheroids from Matrigel, we simply culture the spheroids in a non-adhesive environment and achieve polarity reversal and motility within a few days. However, the Boecking & Walentek method replates the spheroids into the Matrigel for another two weeks, during which period they administer RSPO2&Noggin in order to facilitate polarity reversal, and at the end of this period they dissolve the Matrigel again to finally harvest the apical out spheroids. We believe our method provides a simple, rapid, scalable, and high-throughput protocol that harnesses biological cells' ability to build themselves into multicellular complex structures. Despite their differences in methods, goals, and characterization metrics, these four novel protocols taken together help explore the space of possible morphologies of NHBEs and unravel the morphogenetic potential of human airway epithelium; they are thus significant steps for mapping the morphogenetic plasticity landscape of non-embryonic wild-type cells.

Results

Human bronchial epithelial cells self-construct into multicellular motile living architectures.

To explore the self-organizing plasticity of morphogenesis without genomic change, we chose a cellular substrate in which such outcomes would be most surprising: adult, somatic, human airway tissues. To study and steer the in vitro morphogenesis of novel three dimensional tissues with motile appendages, we developed a novel protocol (Figure 1A) that builds upon the existing ability of human bronchial epithelial progenitor cells to form multicellular spheroids (Figure 1-a.1) with cilia-lined lumina [52-55] (i.e., apical-in configuration). We modified this process by manipulating the culture environment such that it now yields cilia-coated (i.e., apical-out) spheroids, which exhibit spontaneous locomotive ability.

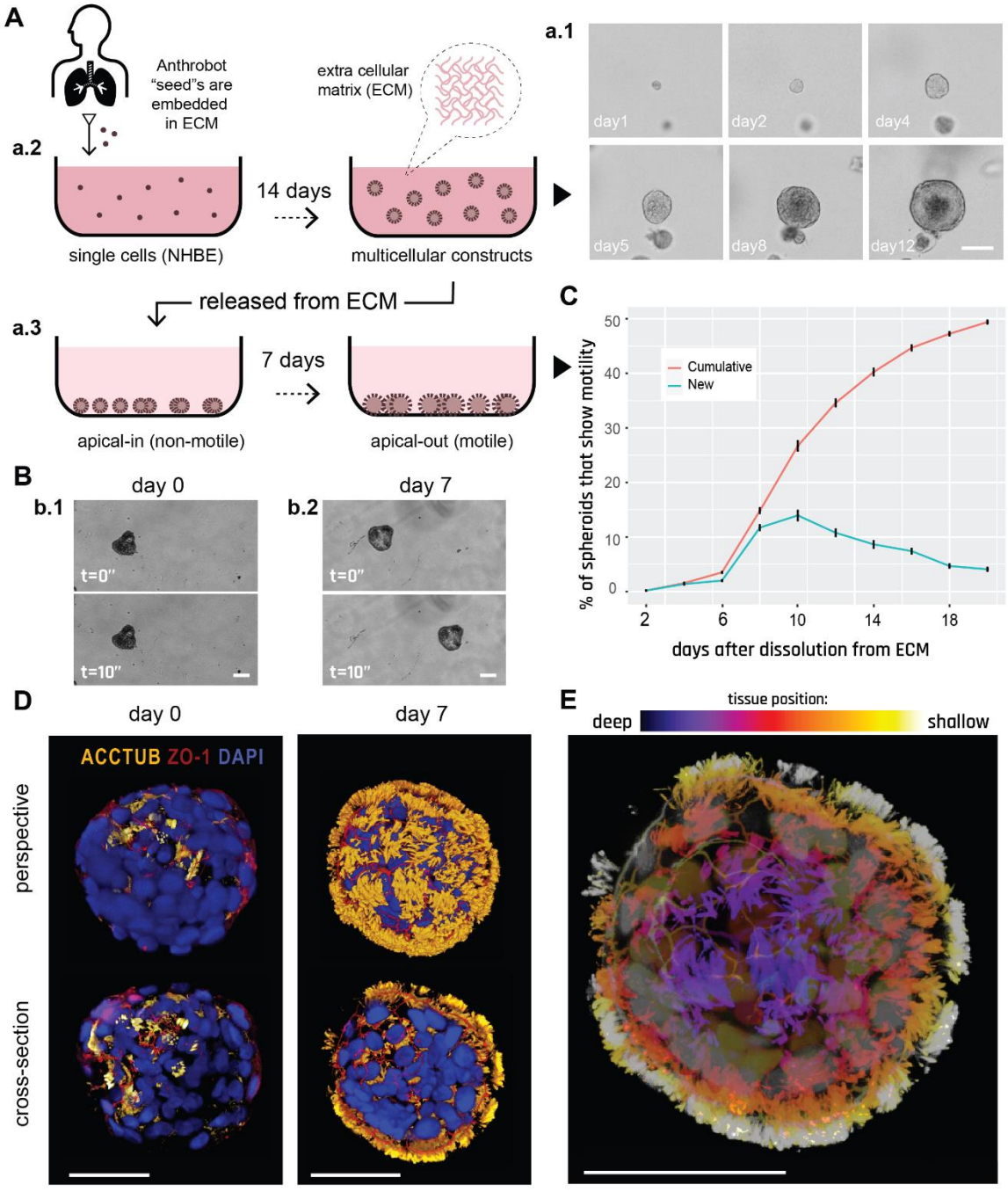

Figure 1 Human bronchial epithelial cells self-construct into multicellular motile living architectures.

(A) Workflow for producing Anthrobots. NHBE cells' apical-in to apical-out transition is facilitated by first culturing them in extra cellular matrix (ECM) under appropriate differentiation-inducing conditions), during which time apical-in spheroids self-construct from single cells (a.1), and upon the completion of this 14 day period (a-.2) by releasing mature spheroids from the ECM (a.3) and continuing to culture them in low-adhesive environment. (B) Phase contrast images of an apical-in (b.1) and apical-out (b.2)

spheroids, captured immediately after dissolution from ECM (day 0) and 7 days after dissolution (day 7), respectively. Day 0 spheroids show no motility, whereas day 7 spheroids show drastically increased motility. (C) Percentage of cumulative (total fraction of motile spheroid since day0) and newly motile spheroids (fraction of motile spheroid that reached motility since the previous time point) in the 3 weeks following dissolution. Out of the 2281 spheroids characterized total, around 50 % consistently showed no signs of motility (despite most having cilia) within this 3-week period and are referred to as non-movers. The data shown on this graph only includes the motile bots, N=1127. (D) Immunostaining of two separate spheroids from day0 and day7 with a-tubulin (cilia marker), ZO-1 (tight junction marker), and DAPI (nuclear stain). The amount of multiciliate cells on the spheroid surface show a drastic increase by day 7. (E) A day 7 Anthrobot with depth information to show full cilia coverage. Bots in panels D, E were immunoassayed with a-tubulin (cilia marker), ZO-1 (tight junction marker), and DAPI (nuclear stain). Colors represent tissue depth. All scalebars on this figure feature 50um.

A key step in their construction, in order to obtain significant translocation, is the induction of cilia to face outward. Given that cilia naturally localize into the lumen due to the basal cells' interaction with the surrounding high-viscosity matrix, we hypothesized that changing the culture environment to a lower viscosity level (e.g., water-based media instead of gel-based matrix) may trigger the basal layer cells to migrate inward and allow the apical layer to take their place on the spheroid cortex [56]. Thus, to trigger apicobasal polarity switching, we first grew airway organoids embedded in Matrigel as reported previously [50] (Figure 1-a.2), which does not yield either ciliated or motile spheroids. We have then proceeded to dissolve the surrounding matrix while keeping the spheroids intact and transferred them into a low-adhesive environment (Figure 1-a.3) and induced them with retinoic acid on a bidaily basis while performing media changes every 3 days. (Matrigel's elastic modulus is 450 Pa [57] whereas water based liquid media's elastic modulus in this low-adhesive environment is $2*10^9$ Pa). This new approach has enabled the originally apical-in spheroids (that show no motility on day 0 as shown on Figure 1-b.1) to became motile by day 7 (Figure 1-b.2), featuring highly motile ciliary appendages

on the spheroid surface. A high-resolution high-speed capture of ciliary movement in Anthrobots (supplemental video 1) show that they deploy a similar propelling strategy observed in multiciliate motile organisms [44].

We next examined two aspects of the microenvironment as possible control parameters for properties of Anthrobot self-assembly. First we tested the role of matrix viscosity, which is known in other bioengineering contexts to impact diverse cell properties, from secretory profile [58] to mechanical attributes [59]. We observed that culture environments with higher viscosity levels than the protocol baseline result in decreased motility (Figure S2) and size (Figure S3), suggesting that low-viscosity environments better facilitate the growth of functional bots as well as yield larger bots. Second, we examined cell seeding density as a factor for motility (Figure S4) and size (Figure S5). We set up three separate conditions: one with the default seeding density in Matrigel (x=30,000cells/mL), one with double this density (2x=60,000cells/mL), and one with half this default density (x/2=15,000cells/mL). After growing the bots under these three conditions for two weeks, while keeping all other protocol aspects constant, we dissolved the mature spheroids from the matrices and measured their size immediately. We then continued culturing the bots per usual maintenance protocol and measured their motility in a binary fashion (i.e., displacing mover or not) during the period where bots show peak motility (between days 9-20) on a bidaily basis. In both experiments, we observed significant differences in the resulting bot sizes and motility (on particular days) among different seeding density conditions, though the effect of introducing additional cells was not linear at any time point tested. These results show that the size and time course of maturation of motile bots could be modulated by altering the concentration of cells in the

Anthrobot differentiation culture, suggesting initial cell seeding density to be a tractable control knob for Anthrobot morphology and function.

To characterize the temporal dynamics of motility initiation, we periodically (every other day) counted the number of motile spheroids for 3 weeks following dissolution and observed a sigmoidal motility profile with peak change in motility on day 10 (Figure 1C). We next confirmed that this drastic change in motility occurred as a result of a morphological reorganization event exposing cilia on the cortex (Figure 1D). We immunoassayed the spheroids on day 0 (pre-motility) and day 7 (post-motility) with DAPI and for the apical markers a-tubulin (cilia marker) and ZO1 (tight junction marker), revealing a drastic increase in external multi-ciliated cells on day 7 compared to day 0. Figure 1E shows the tissue organization within an approximately 50-micron depth of a typical Anthrobot. Upon observing increased multi-ciliated cell presence in motile subjects, we sought to definitively attribute the emergence of motility to the presence of surface cilia. We administered the efficient blocker of cilia motion, ciliobrevin [60,61], and observed the expected drastic decrease in motility (See Figure S6), confirming that the motility of Anthrobots is cilia-driven.

Anthrobots self-organize into discrete movement types.

Despite their wild-type human genome and somatic origin, these self-motile constructs exhibited a wide range of behaviors and an anatomy that differs from the species-specific body morphology. To characterize this diverse landscape and uncover the developmental features of Anthrobots, next we sought to characterize these behavioral and morphological capabilities and investigated a potential correlation

between their form and function. One initial key task for Anthrobots, as with any new behavioral subject [62], is to determine whether its major morphological properties and activities are discrete, continuous, or uniform characters [63,64]. Thus, we quantitatively analyzed their range of behavior modes in time-lapse videos of approximately 200 randomly selected motile spheroids (Figure 2A, see supplemental videos 2-5) for 5 hours in groups of 4 or 5 Anthrobots, and extracted their movement trajectory coordinates. We then split up these 5 hour-long trajectories into 30 second periods to classify behavior with a higher degree of granularity and in an aggregate manner. To identify patterns within a potentially unlimited set of possible movements, we characterized these periods by how straight and/or circular they are as all possible trajectories can be explained together by these two properties. To this end, we used two main trajectory characterization metrics: straightness and gyration indices (see Materials and Methods for detailed description of how these indices are calculated) and plotted all viable trajectorial periods along these two indices (Figure 2B). We then ran the unsupervised clustering algorithm Ward.D2, a common hierarchical clustering method (see methods for more details), on this two-dimensional plot and observed four statistically distinct clusters to emerge (Figure 2C). Further investigation of these clusters reveals that each represents a distinct movement type: circular, linear, curvilinear and “eclectic” (Figure 2D). Further analysis of each cluster in terms of its homogeneity (measured by “average dissimilarity” index), which is a measure of the intra-cluster variation, and its size (measured by “% of observations”) was performed (Figure 2E), as well as a quantitative comparison between different clusters along the two major movement indices (Figure 2F).

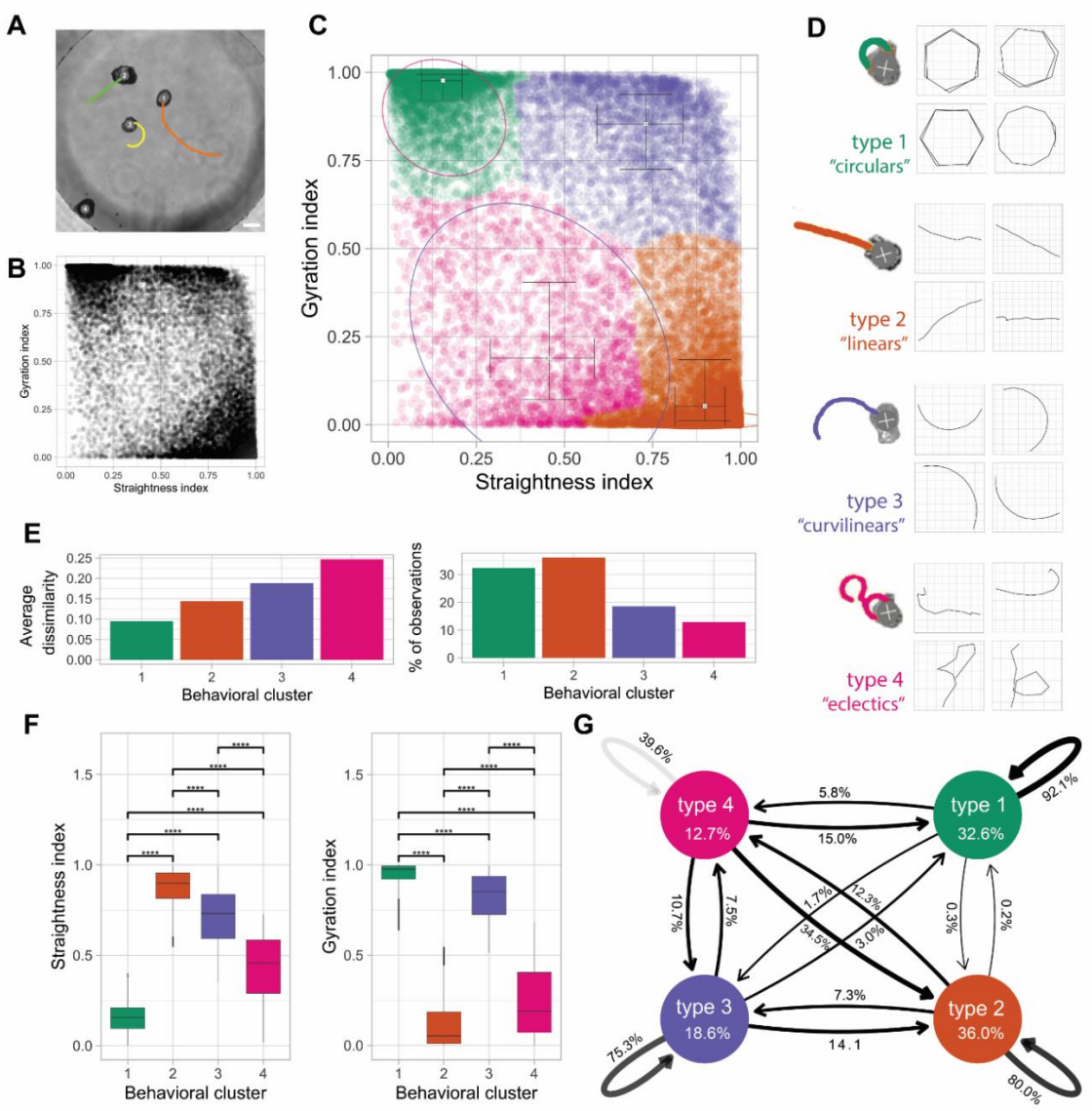

Figure 2 Anthrobots self-organize into discrete movement types.

(A) Anthrobots display different movement types. Scalebar 100uM. (B) Distribution of all 30-second periods in the analysis plotted by their straightness and gyration indices, showing signs of clustering near three of the 4 corners of the plot. (C) Clustered scatter plot of all 30-second periods with centers of cluster marked and colored. (D) Prototypical examples from each cluster with 30-second sample trajectories. (E) Quantitative comparison of key characteristics of the four clusters in terms of intra-cluster homogeneity "average dissimilarity") and occurrence frequency ("% of observations") which show that the largest clusters 1 and 2 have relatively low dissimilarity indicating these are the most consistent behavioral patterns. (F) Comparison of gyration and straightness indices for each cluster with significance levels indicated, showing that each cluster occupies a unique, quantifiable position in the sample space. P-value range after pairwise 2-sample

t-test of 0 to 0.0001 corresponded to ****, 0.0001 to 0.001 corresponded to ***, 0.001 to 0.01 corresponded to **, 0.01 to 0.05 corresponded to * and 0.05 to 1 corresponded to ns. Cluster one had 6004 30-second periods, cluster two had 6700, cluster three had 3436 and cluster 4 had 2384. (G) Markov chain showing state transitions between different clusters (same as in figure 2F) and the degree of commitment to a given behavior (persistence), with the circular bots (type 1) as the most committed category with 92.1% chance of the next period being a circular if the current period is a circular. It is followed by linears and curvilinears, which are also relatively consistent at 80.0% and 75.3% respectively. Cluster 4, or the eclectics, as expected, are very unstable, with a consistency of only 39.6%. Cluster 4 seems to act as a sort of intermediate, since there is a substantial chance of the eclectics converting to linear (34.5%) or to a lesser degree circular (15.0%) or curvilinear (10.7%). The transition probability between circulars and linears and vice versa is the lowest and almost nonexistent, at 0.3% and 0.2% respectively. Linears, curvilinears, and circulars rarely convert into eclectics with a probability of 12.3%, 7.5%, 5.8% respectively (and when they do, it is most likely due to collisions or using eclectics as an intermediary).

As a result of these behavioral characterization analyses, we observed that the circular bots (type 1, Figure 2D) score the highest on gyration and lowest on straightness indices (Figure 2F). They also have highly similar trajectories and are very common among the behaviors of Anthrobots given this cluster has the smallest homogeneity and a representation of over 30% of all the recorded periods (Figure 2E). We also observed that the linear bots (type2, Figure 2D) score the highest on straightness and lowest on gyration indices (Figure 2F). They have less homogeneity than circular bots but also have the greatest representation out of all clusters (Figure 2E). Accordingly, circular and linear bots together make up more than half of the population, and each have highly homogeneous populations. Finally, the third most common (Figure 2E) type of bot is the curvilinear bot (type 3, Figure 2D), which scores high on both the gyration and straightness indices (Figure 2F) and has the second most heterogeneous trajectories (Figure 2E). Bots with most disorganized trajectories and smallest representation in the overall population (Figure 2E) are the eclectic bots (type 4, Figure 2D), which score the lowest on both the

gyration and straightness indices (Figure 2F) due to exhibiting eccentric trajectories that are often a combination of the other three types.

After having characterized each major movement type observed in Anthrobots, we next investigated the transition probabilities between each pair of behavior types. In order to estimate the stability of each trajectory and state transitions between different movement types, we used a Markov chain model shown on Figure 2G, which revealed the degree of commitment to a given behavior (persistence) and provided an ethogram of Anthrobot behavior. We observed that the most stable movement pattern for an Anthrobot is circular motion, followed by linear/curvilinear motion. The eclectics act more like an intermediate and over time, at least probabilistically, resolve into one of the 3 other categories. Therefore, we conclude that the vast majority of Anthrobot movements can be broken down into simpler, highly consistent patterns like linear, circular, curvilinear, with eclectics acting as a transient intermediary. The fact that Anthrobots exhibit movement types with high “consistency” and low rates of inter-type conversion (e.g., between circulars and linears) suggests that Anthrobots self-organize into discrete and stable movement types, each bot having a distinct motility fingerprint.

Anthrobots self-organize into distinct morphological types.

Having observed several distinct movement types, we next asked whether the range of Anthrobot morphologies was continuous or again composed of discrete categories [65-68]. This question is important for both understanding the macro-scale rules of self-assembly, and for future efforts to control their functional properties. We hypothesized the primary parameters of this possible underlying morphological

framework to be a function of the Anthrobots' 3D shape and overall cilia distribution pattern, since Anthrobot motility is generated by cilia. Accordingly, we collected 3-dimensional structural data (Figure 3-a.1) from ~350 Anthrobots through ICC/IF and confocal microscopy, focusing on shape and cilia distribution pattern properties, and binarized these morphological features (Figure 3-a.2) to extract quantitative information on cilia and body boundaries. We then plotted this information for ~350 Anthrobots along eight different morphological characterization indices we developed, each quantifying a different aspect of the Anthrobot shape and cilia pattern. (Figure 3B, also see Figure S7A). The shape-related indices among these eight formal morphological characterization indices included the ratio between the longest and shortest distance within a spheroid (i.e., "aspect"), longest distance within a spheroid (i.e., "max radius"), how invaginating or protruding the spheroid surface is (i.e., "shape smoothness"); the cilia-related indices included the total area covered by cilia signal on a spheroid surface ("cilia points"), cilia signal per unit area on a spheroid surface ("cilia points/area"), proximity of current cilia point distribution to a complete random uniform distribution ("cilia distribution homogeneity"), how clustered the cilia are on a spheroid surface ("polarity"), and how many free-floating cilia points there are that are not a part of a cluster ("noise points"). See Materials and Methods section for more details on how these morphological indices were calculated.

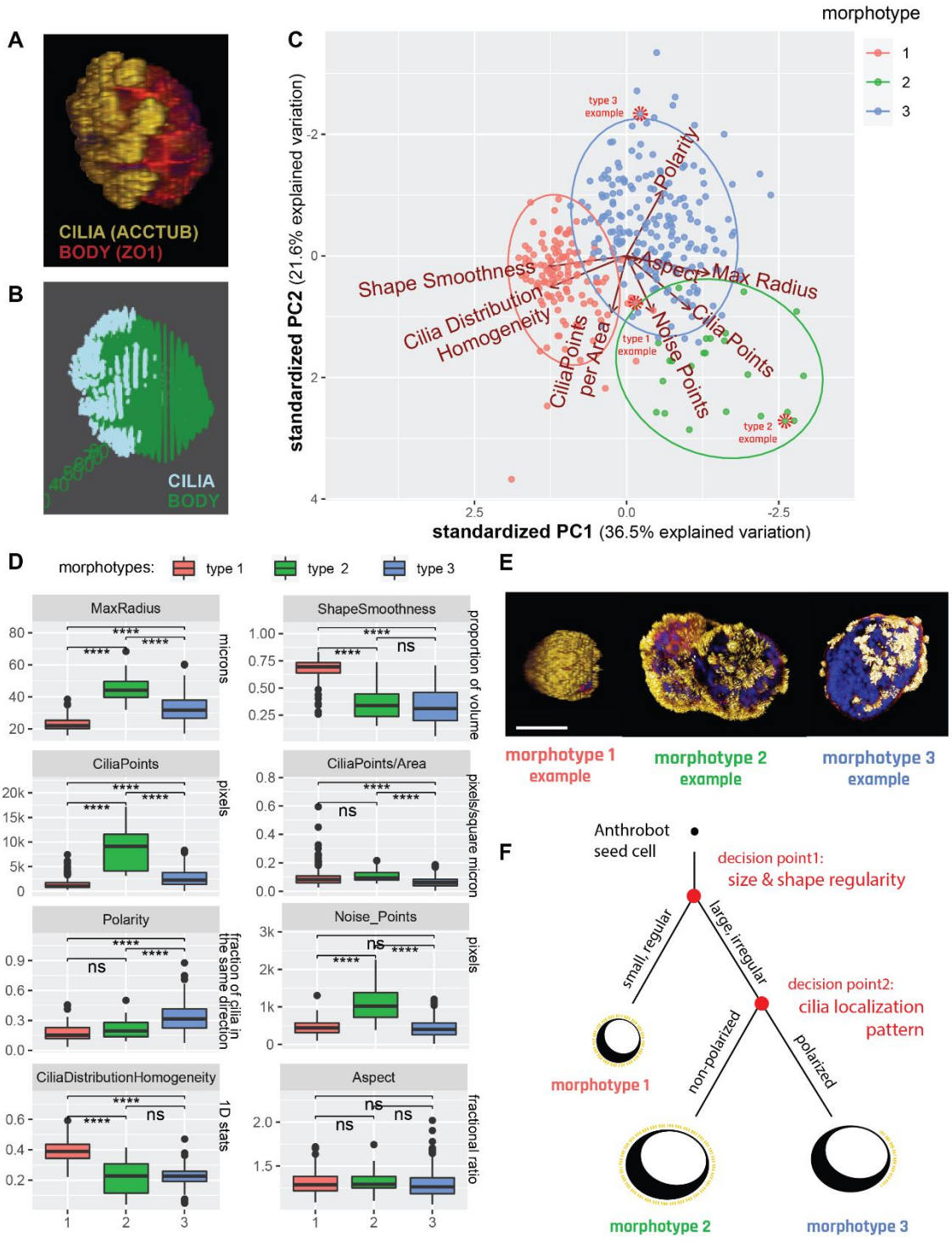

Figure 3 Anthrobots self-organize into distinct morphological types.

(A) Anthrobot immunocytochemistry enables morphological classification pipeline. Sample immunological stain for cilia (acctub, i.e., acetylated a-tubulin) and apical layer marked by the tight junction marker (ZO1) acquired as a complete 3-dimensional Z-stack showing the Anthrobot body boundaries and cilia localization on the body. (B)

Binarized version of the sample immunological data, used as input to the morphological characterization pipeline. (C) Binarized body and cilia information from 350 Anthrobots plotted along 8 morphological indices on an 8-dimensional cloud and clustered with the unsupervised Ward.D2 method, which identify global clusters based on the proximity of the centroids of locally emerging clusters and merging them together when applicable. PCA shows the three morphotypical clusters on the highest variation plane, marked by PC1 and PC2. Red dashed circles point to specific examples featured in panel E, selected from the cluster edges for distinct representation. (D) Distinct morphotypes translate with significance to differences in real-life morphological metrics, characterized by 8 variables from which the PCA was computed. The P-value range of 0 to 0.0001 corresponded to ****, 0.0001 to 0.001 corresponded to ***, 0.001 to 0.01 corresponded to **, 0.01 to 0.05 corresponded to * and 0.05 to 1 corresponded to ns. Clusters 1,2 and 3 in the analysis corresponded to the clusters in the PCA, with n = 125, 24 and 201 respectively. We ran a two-sided, two-sample t-test on all pairs of clusters, for all 8 variables, which are then plotted here. (E) Sample morphotype examples for Type 1, 2 and 3 chosen for their ability to best represent the cluster. Type 1 Anthrobots are small, regularly shaped, tightly and uniformly covered by cilia. Type 2 and 3 bots are larger, more irregularly shaped and have less tightly knit cilia patterns, with type 3 bots featuring significantly more polarized cilia coverage. Scalebar 50uM. (F) Decision tree of Anthrobot morphogenesis with two major checkpoints as revealed by the PCA hierarchy: first decision point is size/shape (has equal impact), second decision point is cilia localization pattern.

Next, we performed a PCA followed by an unsupervised clustering algorithm on this 8-dimensional data cloud and observed the emergence of three statistically distinct clusters (Figure 3C), each representing a distinct morphological type (morphotype). Figure 3D shows a quantitative characterization of each cluster along 8 different morphological indices. This analysis revealed the following two characteristics to be the most important distinguishing factors (to an equal degree, both ranking the top place in PC1 contributions) between different morphotypes: the size of the Anthrobot (measured by “max radius”), and the uniformity of its shape (measured by “shape smoothness”). These two most distinguishing characteristics formally describe type 1 bots to be significantly smaller in size and smoother (spherical) in its volume, while type 2 bots to be the largest and least uniformly shaped, and type 3 to be somewhere in between the two both. (See

Materials and Methods section for PC1 and PC2 contribution rankings of different indices used to uncover this hierarchy.)

At the second level of importance in distinguishing between these three morphotypes is a set of four indices (all ranking equally top place in PC2 contributions), pertaining to cilia characterization. While the first two of these indices characterize cilia count, i.e., the density of cilia per Anthrobot (measured by “cilia points”), and the density of cilia per unit area of Anthrobot (measured by “cilia points/area”); the remaining two indices characterize the pattern in which these cilia are distributed: how tightly grouped the cilia are (measured by “polarity,”), and the number of “free-floating” ciliary patches that are not within a group (measured by “noise points”). These four indices together describe type 2 bots as being significantly more ciliated than type 1 and type 3 bots, and type 3 bots as having a significantly more polarized cilia distribution pattern (with the least amount of extra-cluster noise) in comparison to type 1 and type 2 bots (Figure 3D).

The third most important (scoring a second level rank in both PC1 and PC2) characteristic in distinguishing between the different morphotypes is a function of both the size/shape of the Anthrobot and the localization pattern of its cilia: the homogeneity of cilia distribution on the surface of the Anthrobot (measured by “cilia distribution homogeneity”). This local index is related to, but not directly anti-correlated with, the polarity index, because while cilia distribution homogeneity characterizes local neighborhood patterns, polarity (along with its supporting index “noise points”) characterizes the global (entire Anthrobot-level) cilia distribution. (See Materials and Methods for more information). In this way, we obtain both a local and a global view of the cilia distribution patterns at once and identify type 1 bots as both globally and locally

homogeneous, type 2 bots as globally homogeneous but locally heterogeneous, and type 3 bots as both globally and locally heterogeneous with high degree of global polarization.

In summary, our morphological characterization pipeline suggest that Anthrobots self-organize into 3 major morphotypes (Figure 3E) and this relationship can be represented by a developmental decision tree shown on Figure 3F wherein the first "decision point" determines the Anthrobot size and shape. Accordingly, bots that are small and regularly shaped (morphotype 1) form one branch, whereas bots that are larger and more irregularly shaped (morphotypes 2 and 3) form the alternating branch. On this alternating branch a second decision point forms further downstream and determines Anthrobot cilia pattern. Anthrobots with a non-polarized cilia pattern form one branch (morphotype 2), and Anthrobots with a polarized cilia pattern form the other (morphotype 3).

Finally, one characteristic that does not seem to be changing in any significant way between these three morphotypes is the ratio between the longest and shortest distance within a spheroid (measured by "aspect"). Although the 3 morphotypes differ significantly in terms of the volumetric regularities (measured by the shape smoothness index) as explained above, their aspect ratios are statistically very similar.

Distinct movement types and morphotypes are highly correlated.

Having observed the emergence of several discrete types of movement (Figure 2) and morphology (Figure 3), we next decided to investigate whether there is a mapping between Anthrobots' different movement types and morphotypes. To do this, we incorporated an additional level of movement-type information into the PCA analysis used

for identifying the morphotypes as introduced in Figure 3. During the initial sample collection process for this analysis, we were able to definitively distinguish between non-motile Anthrobots (non-movers) and motile Anthrobots (movers) as described in Figure 1C. To further represent the movement types observed within the mover population, we randomly sampled from the set of motile subjects, targeting 30 Anthrobots that translocated (*i.e., displacing movers)* to assign a movement type. Selected displacing movers were randomly collected from the two most orthogonal movement types, circulars and linears, in approximately equal proportions.

Next, we identified these non-mover and displacing mover Anthrobots within the PCA cloud presented in Figure 3C and assigned them this additional layer of information, i.e., movement type (Figure 4A) without changing anything else in our sample pool or analysis workflow. In result, 62% of non-movers were identified within morphotype 1 cluster (with the remaining 38% falling into the morphotype 2 cluster). A 100% of displacing bots were identified in morphotype clusters 2 and 3, with ~85% of linear bots being in cluster 2, and 88% of circular bots being in cluster 3. We have further computed the statistical significance of these overlaps (using the Fisher test, see Materials and Methods) and conclude that the non-movers, linears, and circulars significantly correspond with the morphotypes 1, 2 and 3, respectively.

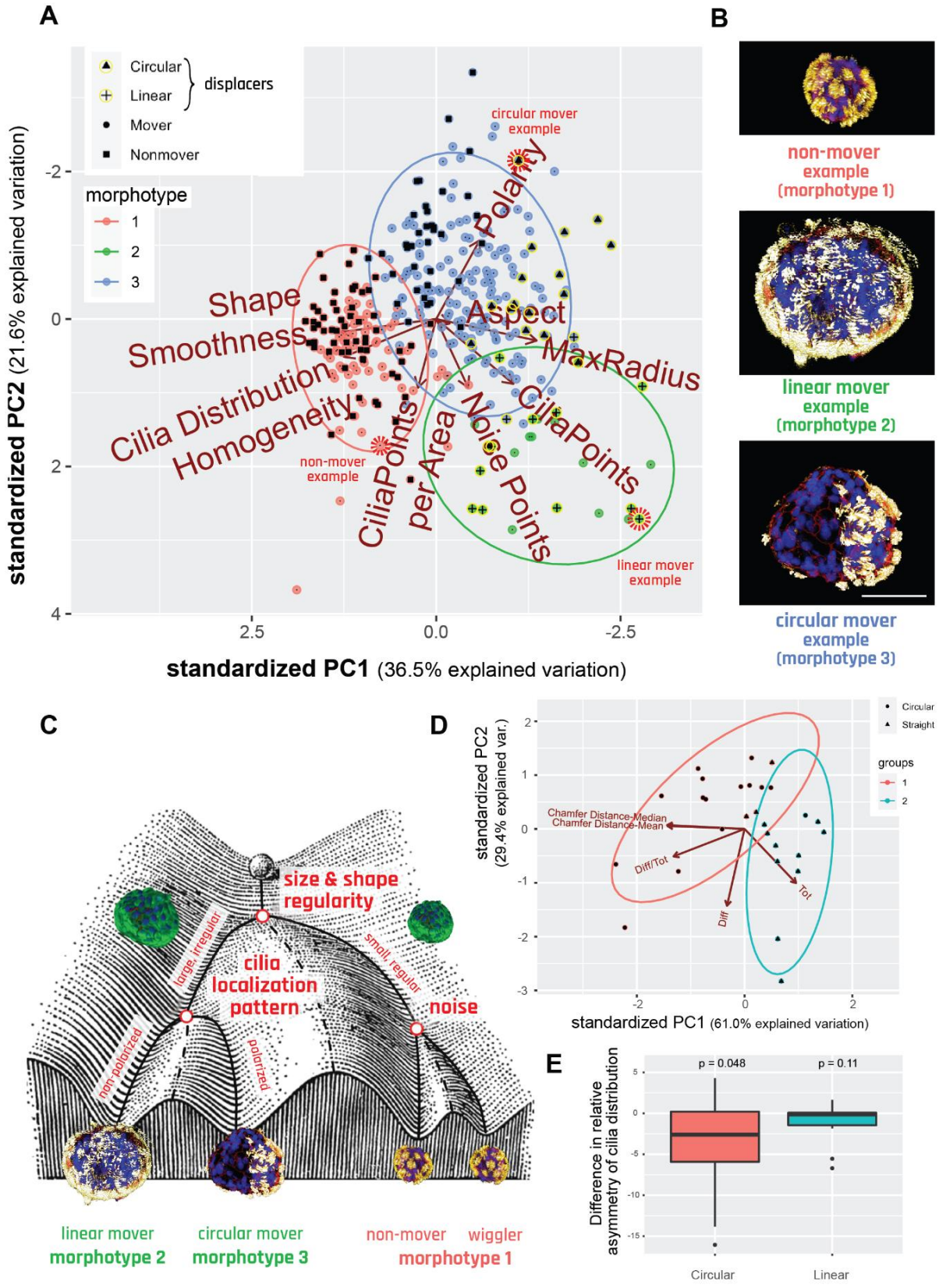
A
B
C
D
E
Circular
Linear
displacers
Mover
Nonmover
morphotype
1
2
3
circular mover example
non-mover example
linear mover example
Polarity
Shape Smoothness
Aspect
MaxRadius
Cilia Distribution Homogeneity
CiliaPoints per Area
Noise Points
CiliaPoints
standardized PC2 (21.6% explained variation)
standardized PC1 (36.5% explained variation)
non-mover example (morphotype 1)
linear mover example (morphotype 2)
circular mover example (morphotype 3)
size & shape regularity
cilia localization pattern
noise
large, irregular
small, regular
non-polarized
polarized
linear mover morphotype 2
circular mover morphotype 3
non-mover wiggler morphotype 1
Circular
Straight
groups
Chamfer Distance-Median
Chamfer Distance-Mean
Diff/Tot
Diff
Tot
standardized PC2 (29.4% explained var.)
standardized PC1 (61.0% explained variation)
p = 0.048
p = 0.11
Difference in relative asymmetry of cilia distribution
Circular
Linear

Figure 4 Distinct movement types and morphotypes are highly correlated.

(A) PCA of 350 bots forming 3 morphotypical clusters, showing that there is significant overlap between these clusters and the separately marked non-movers, linears and circulars. Red dashed circles mark specific examples featured in panel B, selected from the cluster edges for distinct representation. (B) Sample morphotype examples from each cluster, corresponding to Cluster 1, 2 and 3 and Nonmover, Linear, and Circular, respectively chosen for their ability to best represent the morphotype vs movement type mapping. Scalebar 50uM and applies to all three bots. (C) Waddington landscape illustrating the logic of determination of bot behavior and their relation to morphotypical indices with end behavioral products, as well as the potential states possible at each level of bifurcation of the bots' development. (Waddington Landscape image modified from J. Ferrell, 2012.) (D) PCA and unsupervised clustering showing the polarization among linear and circular bots in respect to bilateral symmetry metrics. (E) Difference in asymmetry of cilia distribution between the movement axis and its 90-degree offset axis. Here, n = 15 and 13 for Circulars and Linear respectively, with p = 0.0482 and 0.1116 done by one-sample t-test for each with alternative hypothesis.

The fact that none of the displacing bots were identified within the morphotype 1 cluster suggests that the movers identified within this cluster (i.e., those morphotype cluster 1 data points which are not labeled as "non-movers") are statistically likely to be *non-displacing movers*, displaying a stationary wiggling motion. Accordingly, we conclude that morphotype 1 bots are likely to assume either non-mover behavior or wiggler behavior. This may be attributable to their spherical shape with homogeneously distributed cilia where the propulsion forces generated by the ciliary motion are more prone to canceling each other out due to the radially symmetric spherical shape, resulting in little or no movement. Accordingly, inherent noise in the system (such as small imbalances in the cilia distribution on the spheroid surface or how the bot happened to be oriented in the plate) may be sufficient to have these bots generate small amounts of movement, causing them to wiggle, but not enough movement to become a displacing bot.

As a result of these analyses, we conclude that there is a statistically significant relationship between the Anthrobots' developmental morphology and their behavior, and we show visual examples of this relationship with categorical examples on Figure 4B. We further represent this relationship by a decision tree in the form of a Waddington Landscape – a formalism often used to characterize cell- and body-level properties by mapping out the sequential logic of decision-points in transcriptional space or morphospace [69-72]. Figure 4C shows the Waddington Landscape for the Anthrobot. The single cell at the top of the diagram represents the single cell that will develop into the multicellular Anthrobot. During this process of self-construction, the Anthrobot moves through the developmental landscape, negotiating certain points of morphological possibility to reach its final architecture. We conclude that the unique and spontaneous 3-D multicellular morphogenesis of adult airway cells into Anthrobots is consistent; the final form of the Anthrobot displays a degree of variability and exhibits discrete characters with easily recognizable primary features that also map on to phenotypic behavior.

Anthrobots show bilateral asymmetry along movement axis.

The above metrics all focused on the global structure of the bot. Next, we studied the local characteristics that connect the movement of bots to their morphology, by looking for a difference in bilateral symmetry, or lack thereof, between the two major types of displacing bots (linears and circulars) through symmetricity measurements across plane coincident with their direction of movement. One hypothesis is that Anthrobots have bilateral symmetry that underlies their ability to move in straight lines (as observed in many existing species [73,74] and even synthetic forms [75]); this hypothesis predicts that

Anthrobots with circular motion should have more asymmetry across their movement axis compared to other planes. This hypothesis was tested by running a PCA and unsupervised clustering algorithm on a point cloud quantifying Anthrobot cilia distribution patterns through four major bilateral symmetry-related measurements: total cilia points on a given bot (measured by “tot”), difference in number of cilia points between the two hemispheres (halves of the bot that are separated by the movement axis) of a given bot (measured by “diff”), this difference normalized by total cilia points (measured by “difftot”), and finally the bilateral symmetry index along the movement axis (measured by “Chamfer distance,” see methods for more details). Results of this analysis (Figure 4D) yielded two major clusters that in a statistically significant manner, each corresponding to one of the two major types of displacing bots (linears and circulars), with the group consisting predominantly of linears scoring significantly higher on the bilateral symmetry measurement (via Chamfer Distance axes, which inversely correlate with bilateral symmetry measurement). This result provides preliminary evidence in support of the hypothesis that Anthrobots with linear movement trajectories may have higher degrees of bilateral symmetry.

In order to further test this hypothesis, while also controlling for the globally homogeneous cilia distribution in linear bots posing a potential confounding factor for bilateral symmetry measurements, we compared the bilateral symmetricity of linear and circular bots against arbitrary axes other than the axis of movement. The initial hypothesis that linear Anthrobots may have higher degrees of bilateral symmetry compared to circular bots automatically suggests that for linear bots, we would expect there to be no other axis than the axis of movement along which the bilateral symmetry is higher; and

for circular bots, we would expect there to be other axes than the axis of movement in respect to which the bilateral symmetry is higher. We tested this postulation by measuring linear and circular Anthrobots bilateral symmetry indices separately along each bot's axis of movement vs its farthest rotated (i.e., 90-degree rotated) counterpart (as the control axis). As a result (Figure 4E), we indeed observed that while for the linear bots there exists no other axis in respect to which the bilateral symmetry is higher than that of the axis of movement, for the circular bots, there exists other axes than the axis of movement in respect to which the degree of bilateral symmetry is higher ($p = 0.048$). (See Figure S8 for comparison with other control axes that have rotational angle smaller than the farthest possible 90-degrees.) Taken together, these findings support our hypothesis that Anthrobots with distinct movement types have distinct local bilateral symmetry profiles, with linear bots showing higher bilateral symmetry. This suggests that these synthetic forms recapitulate a fundamental morphological property observed in many wild-type species.

Anthrobots can move across scratches on live monolayers in vitro.

One possible use of these living biobots is to manipulate other tissues, in vitro or in vivo, in future biomedical or bioengineering applications. How will biobots react to environments different from those that their component cells face in their native configuration in vivo? Thus, Anthrobot behaviors need to be characterized outside of a bare culture dish context, and especially in environments that airway epithelia do not normally encounter. Having characterized their baseline movement and morphology, we wanted to assay this novel motile form for potentially useful behaviors and ways in which

it may interact with other somatic tissues, especially sites of damage. Because we are interested in surprising examples of behaviors in such novel constructs, we sought to confront them with a scenario which would not be natural for these airway cells, either in vivo or in their evolutionary history. We decided to study the ability of Anthrobots to move across live tissues that have been damaged, taking advantage of a common model system: the monolayer scratch assay in vitro [76,77]. We produced 2-D confluent layers of human neurons derived from hiNSCs based on a previously established method [78], and introduced a scratch of 400-1000 microns by mechanically scratching away the neuron layer in a long swath. We chose hiNSC-derived scratches, instead of for example smooth and regular PDMS channels, because complex borders of such in-vitro live tissue scratches featuring live cells constitute more biologically realistic in-vitro proxies. We are interested in developing aspirational models for more complex scratched multi-layered live tissues which are more prone to reveal novel and interesting interactions compared to gels or other artificially smooth surfaces.

Anthrobots were placed within these neuronal scratch environments in order to characterize their dynamics in this novel biological environment. Bots were allowed to freely move on their own and timelapse videos were recorded (Figure 5A, see supplemental videos 6, 7). These videos were then tracked, and specific indices were calculated from the tracked files (Figure 5B). Among these indices, we characterized the degree to which bots interact with the native tissue surrounding the scratch (measured by “proportion of bot on tissue”), bots’ tendency to assume a circular motility profile (measured by “bot’s rotational tendency”), and bots’ displacement speed in traversing the scratch (measured by “instantaneous velocity”). More specifically, we investigated the

relationship between bots' efficiency in traversing the scratch as a function of the circularity of their movement pattern (Figure 5C). We observed a significant positive relationship (slope=1.5, p=0.01), confirming our baseline assumption that although circling bots are less efficient in forward motion, they are better at covering the most unique coordinates in the scratch. We have further observed that the instantaneous velocity also had a significant positive relationship with bots' efficiency in moving across the scratch (slope=0.0082, p=0.031 (Figure 5D), presumably due to increased collisions with the tissue. Taken together, these data reveal that Anthrobots are capable of efficiently moving across damaged tissues, and that bots that have a higher rotational tendency and or higher speed have higher degrees of unique coordinate coverage by moving across a higher percentage of the scratch interface.

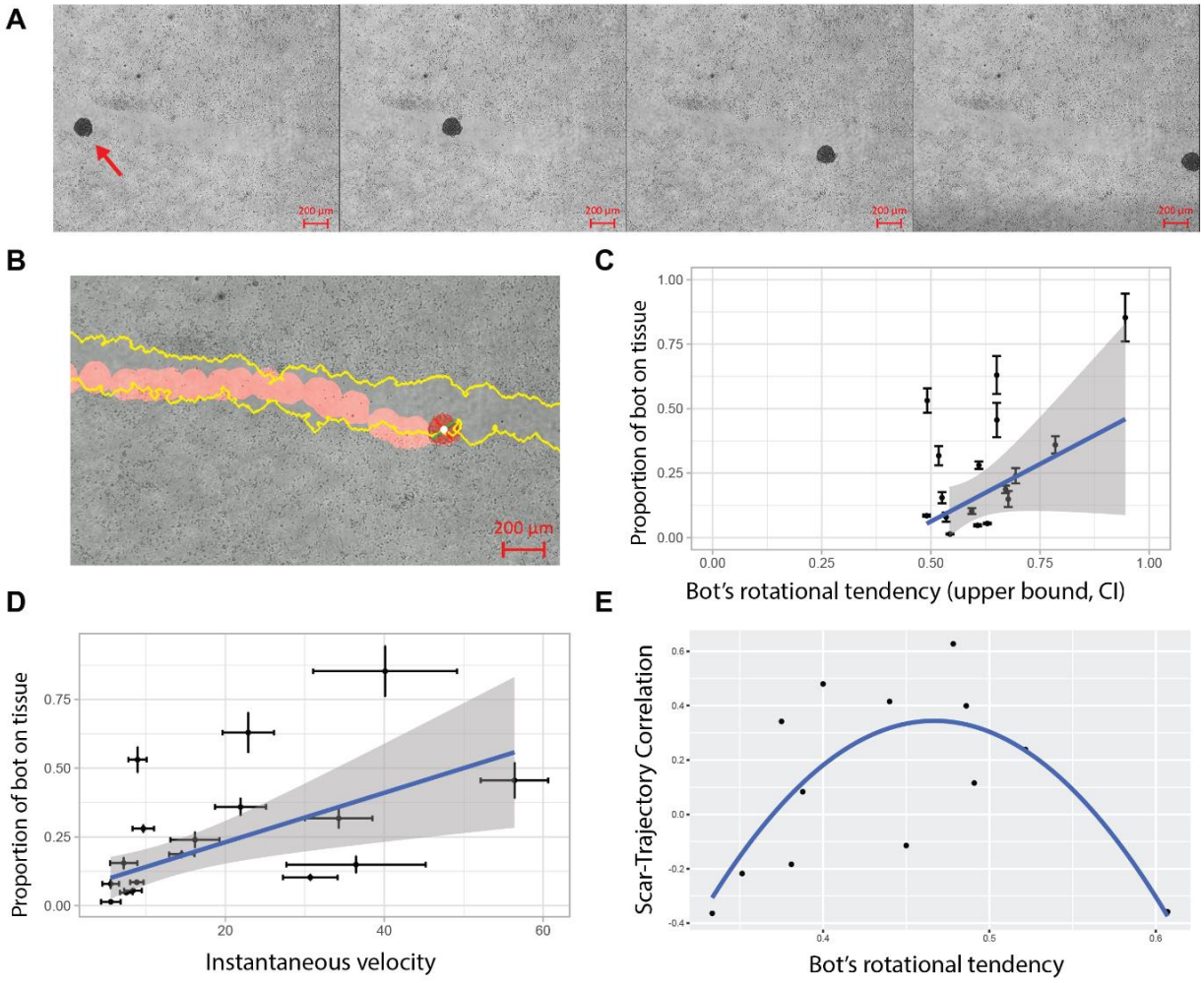

Figure 5 Anthrobots can move across living monolayers in vitro.

(A) A representative timelapse video of an Anthrobot as it moves along a neural scratch in vitro. (B) Sample tracking video output with scratch edge highlighted in yellow and bot path in red. The rotation of the bot is measured through the change in the orientation of the green and red bars attached to the center of the bot in white. (C) The significant (p=0.017, slope 1.15, n=17, t-test for slope) positive relationship between bot gyration index and proportion of bot's body in contact with scratch suggest that circular bots cover the edges of the scratch more as they move along the scratch. (D) The significant (p=0.031, slope 0.0082, n=17, t-test for slope) positive relationship between bot speed and proportion of bot's body in contact with scratch further suggest that faster bots also cover the edges of the scratch more as they move along the scratch. (E) For a subset of bots (dataset constrained to non-stalling bots with rotational tendencies between 0.33 and 0.7 and viable tracking videos), the quadratic (alternative curves were insignificant) relationship (p=0.006, n=13, t-test) between bot gyration index and scratch-trajectory similarity metric suggests that there is a goldilocks zone for the bot rotational tendency for maximum scratch area exploration. This quadratic relationship was revealed when we initially tested for a linear relationship between these two metrics by plotting the residuals

against the fitted values for the model and observed a clear quadratic trend among the residuals (see Figure S9), which strongly suggested the fitting of a quadratic model instead, which is shown here. Consistent with these statistical analyses, in the experimental space we observed that bots with very low rotational tendencies interacted minimally with the scar edges while bots with very high rotational tendencies skidded in place or was prone to veering off the scratch edge. There appears to be an optimal amount of rotation for a bot to move across the scratch while faithfully following the scratch edge.

Having observed the behavior of these bots in scratches, we focused on the interactions between various scratch edge patterns and bots' ability to track along them. In order to do so, we first constrained the dataset to trajectories that could be used to further understand this relationship. We specifically focused on bots that were not extreme in their rotational tendencies, had ample contact with the scratch and had viable tracking videos (see Materials and Methods). This enabled us to isolate the tendency of the bot to turn consistently in the same direction (measured again by "bot's rotational tendency") and the correlation between the trajectory and scratch edge (measured by "scratch-trajectory correlation"). With our constrained dataset, we saw that gyration had a quadratic effect on scratch-trajectory similarity (Figure 5E) with $p=0.006$, suggesting that there is a specific range for gyration where the scratch-trajectory correlation can be maximized: Anthrobots can be chosen to specifically maximize coverage efficiency based on their rotational tendency.

Anthrobots can promote gap closures on scratched live neuronal monolayer tissues.

One of the most important aspects of exploring synthetic morphogenesis is the opportunity to observe novel behaviors that are obscured by standard, default phenotypes. Having seen that these airway cell-derived constructs can move along and

settle in neural scratches, we decided to check for the effects of their presence on the surrounding cells. A characterization of their wild-type capabilities is important not only for understanding biological plasticity but also for establishing a baseline for future efforts in which biobots are augmented with additional synthetic circuits for pro-regenerative applications.

Inspired by collective behavior and swarm intelligence, and more generally, how in nature collectives can accomplish tasks that individuals cannot, we decided to create “superbot” assemblies by facilitating random self-aggregation of distinct Anthrobots that fuse to form larger structures. We accomplished this without using molds or any other external shape-giving equipment, but by simply constraining multiple Anthrobots in a relatively smaller dish, while keeping everything else constant. Akin to how ants cross openings that are too wide for a single ant to cross by forming a bridge through aggregation of their bodies [79], we placed these superbots into arbitrary sites along the tissue scratch such that they span the entire width of the scratch, enabling them to “bridge” two sides of the damaged tissue in order to see if we can induce any kind of repair of the scratched monolayer by bridging the two sides, akin to a mechanical stitch. Figure 6A shows a superbot on a scratch upon its placement on day 0, as well as the resulting bridge configuration on subsequent days of day 1 and day 2.

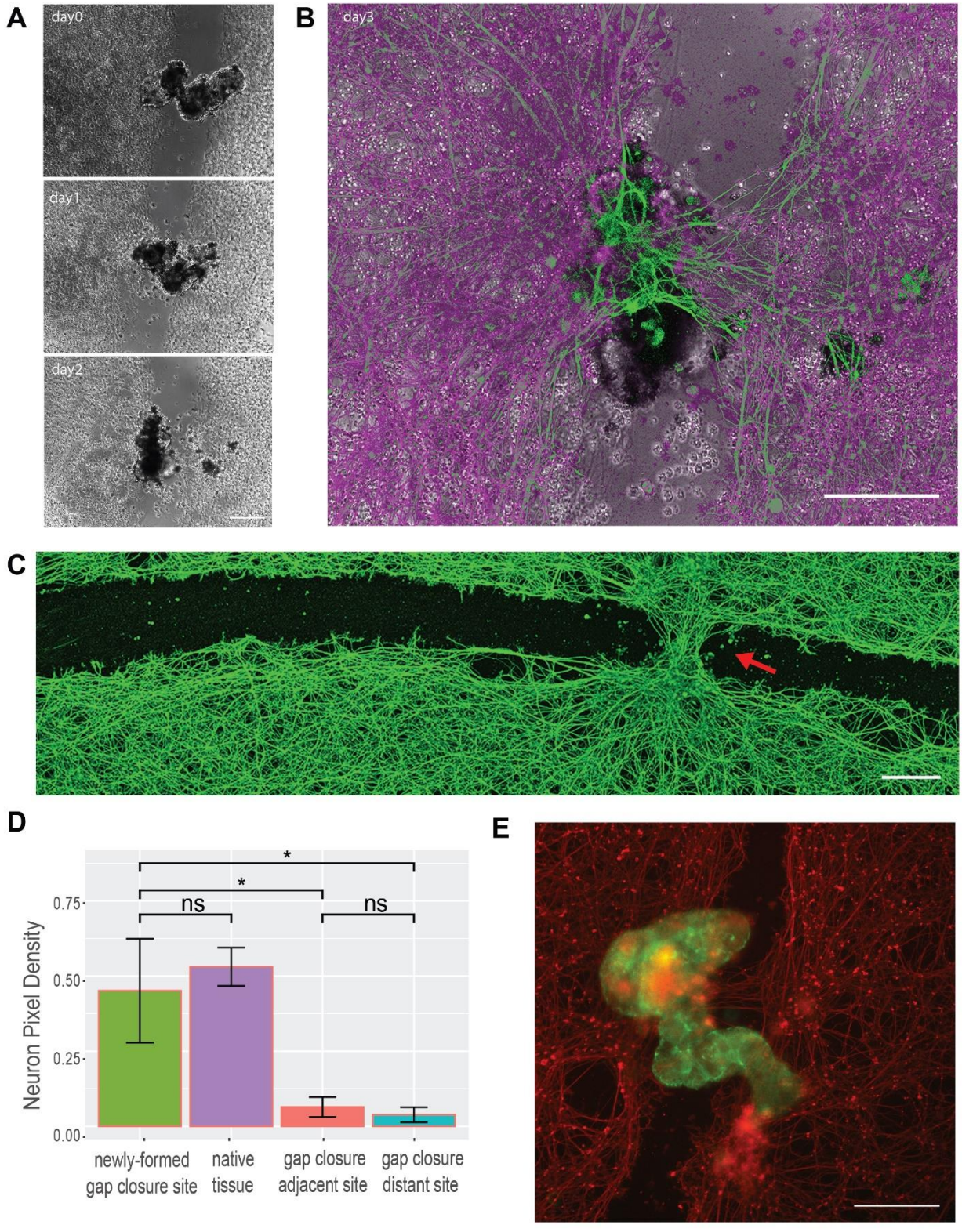
A
day0
day1
day2
B
day3
C
D
Neuron Pixel Density
0.00
0.25
0.50
0.75
ns
ns
*
*
newly-formed gap closure site
native tissue
gap closure adjacent site
gap closure distant site
E

Figure 6 Anthrobots can promote gap closures on scratched live neuronal monolayers.

(A) sample micrograph of a bridge across a neural scratch over time from bridge inoculation day (day0) to days 1 and 2. (B) An overlay of a bridge bot and the induced "stitch" (i.e., gap closure site) at the end of the observation on day 3.(C) Immunological staining of neurons with Beta III Tubulin (Tuj1) upon fixation on day3 after the bots were introduced to the system, showing an induced neural gap closure at the site of bot settlement. (D) Among N=10 experimental replicates, 50% of the Anthrobot bridges have maintained connectivity to both sides of the scratch area across all three days of the experiment (i.e., fully connected bridges), and among these bridges, 100% has yielded gap closure underneath at the neuronal scratch site. Shown here is a quantification of the resulting tissue on day 3 of all fully connected bridges measured by average proportion of neuronal coverage by pixel counts for each positional category: gap closure site, unscratched native tissue (calculated by the average of the two neuron-heavy area pixel coverage), adjacent and distant sites to the gap closure. Difference between gap closure site and native tissue is insignificant ($p = 0.37$), while the difference between the gap closure site and both adjacent and distal scratch sites are significant (w/ $p = 0.006$ and $p = 0.005$, respectively); that suggests the tissue at the gap closure site is as dense as the native tissue, and the gap closure effect follows a crisp profile as opposed to a gradient profile. The P-value range of 0 to 0.0001 corresponded to ****, 0.0001 to 0.001 corresponded to ***, 0.001 to 0.01 corresponded to **, 0.01 to 0.05 corresponded to * and 0.05 to 1 corresponded to ns. See methods section for example frame of a sampling region. Scratch lengths varied between 150-500um (E) Immunological staining of another sample bridge superbot (green) and the neuronal tissue (red). All scalebars on this figure feature 200 microns.

Strikingly, within the next 72 hours upon inoculation of the superbot into the tissue scratch on day 0, we observed a substantial regrowth of the native tissue taking place (i.e., gap closure), resulting in the formation of a stitch right underneath the "superbot bridge," connecting the two sides of the scratch (Figure 6B). This gap closure was observed solely at the site of superbot inoculation, and at no other place along the long scratch (Figure 6C). A quantitative analysis (Figure 6D) of these gap closure sites shows that while the neuron pixel coverage density of the gap closure site is as high as the native tissue outside the scratch (see Figure S10), the rest of the scratch space, whether adjacent or far, had significantly less density of coverage. Thus, the density of the induced

gap closure area that formed as a result of the presence of the superbot represented full (statistically indistinguishable from 100%) recovery of the original tissue and was uniquely different from the surrounding scratch area. Further quantification of superbot bridge-assisted neuronal gap closure formation showed an average aspect ratio of 0.7 on average. Finally, in order to test whether simple (passive) mechanical contact or presence of other biological substance was sufficient to induce the same effect, we incubated neuronal scratches for 4 days with a piece of agarose (see Figure S11) and a multicellular spheroid made up of HEK cells (see Figure S12) on top of the neuronal scratch to provide purely mechanical as well as other biological tissue loading and; neither induced any gap closure behavior.

Discussion

Biorobotics and bioengineering have at least two main areas of impact. One is the production of useful living machines [3,5,80]. The other is the use of unconventional configurations for living materials at all scales, to probe the macro-scale rules of self-assembly of form and function [16,81-83]. Specifically, by confronting evolved systems with novel contexts, we can learn about the degree of plasticity that cells and control pathways can exhibit toward new anatomical and functional endpoints, as well as develop protocols to alter default outcomes. Here, we used human patient cells to begin the journey toward immunologically acceptable, active, living biomedical constructs, and to begin to probe the morphological and functional capabilities of mammalian, adult cells.

Self-motile, fully-organic biobots have been demonstrated with frog cells [40-42]; however, it was unknown whether the surprising properties of Xenobots depend strongly

on their amphibian genome and evolutionary history, as well as their embryonic state. Specifically, the plasticity of amphibian tissues, and the propensity of embryonic cells to self-assemble into structures were thought to be unique features that may not be available to engineers working with adult patient-derived cells. We show that despite spending their entire life in a flat, tracheal architecture (a cycle of over 4-8 decades for our donors), these human cells, with a wild-type genome and no introduction of scaffolds or nanomaterials, are able to implement a novel set of morphogenetic classes and motile behaviors. Another surprising finding, given the usually tight mapping between genomes and species-specific form and function, the Anthrobots adopt some of the morphological and functional properties similar to Xenobots despite their highly divergent genomes.

Anthrobots' overall shape and behavior are similar to that of Xenobots, but not identical. Anthrobots are around 20 to 300+ micrometers in size, whereas Xenobots range from an average of 487±39 μm for the smallest cut explants to 602±30 μm for the largest[30]. Xenobots likewise offer discrete motion types, and their behavior transition profile is similar. The interconversion between linear and circular is very small for Xenobots (0.5% and 1.6%) and Anthrobots (0.2% and 0.3%), while their consistency of Circular behavior is extremely high for Xenobots (95%) just like for Anthrobots (92%). However, Xenobots' linear behavior consistency was not as high (67%) when compared to Anthrobots (80%). Despite their highly divergent genome, age, and tissue origin, the two platforms assemble into very similar types of creatures, illustrating the importance of generic laws of morphogenesis [84-89] in addition to species-specific genomic information.

Another difference from existing biorobotics is that the Xenobots' construction depended on a rate-limiting process of extracting source cells from frog embryos. Here

we show a protocol for enabling the self-construction of Anthrobots: living structures made from epithelial cells that traverse aqueous environments. The process is highly scalable, and produces Anthrobots in the course of 3 weeks, with minimal manual input beyond weekly media changes. At the end of their 4-6 weeks life span, they safely degrade by becoming unviable debris.

Anthrobots exhibit several distinct movement and morphological classes, which are significantly correlated. This is especially important because the structure and function of this novel construct is not that of a familiar organism (despite a wild-type genome), and it was not yet known whether its morphospace possessed specific attractors, how reliable the cells' navigation of that morphospace was, or how the movement patterns would relate to its specific morphology. Anthrobots showed clear and consistent active movement types, quantified over 30 second periods: circulars, linears, curvilinears, and eclectics, with the last category including the non-displacing bots, i.e., wigglers, as well as distinct morphotypes that are best distinguished by Anthrobot size, shape, and cilia localization patterns. While more work needs to be done to establish a causal relationship between these morphotypes and the movement types, our analyses showed significant correlation between the non-displacing (wiggler or non-mover) movement type and morphotype 1, linear movement type and morphotype 2, and finally circular movement type and morphotype 3. Such correlation has implications for future control of higher-order behaviors (such as movement types) by way of controlling Anthrobot morphology through synthetic morphogenesis, as well as real-time physiological signaling. In the future, machine learning classifiers may help predictively identify different movement types from phase contrast images of live bots, without

needing to perform immunostaining on them. Furthermore, such classifiers will use AI tools to correlate initial physiological parameters with final outcomes, as part of the effort for using Anthrobots as a platform for cracking the morphogenetic code.

Analysis of movement and morphology has further revealed the ability of the Anthrobots to establish bilateral symmetry, which is an interesting aspect of self-assembly in a symmetrical environment and will enable future studies of the still poorly understood question of how multicellular amniote embryos bisect themselves to establish a single midplane for their body plan.

We found that Anthrobots can traverse neural tissues and defects therein. This popular but highly simplified injury model [76] is just the beginning for understanding how Anthrobots will deal with traversing complex multifaceted three-dimensional tissues. Most remarkably, we found that Anthrobots induce efficient healing of defects in live human neural monolayers in vitro, causing neurites to grow into the gap and join the opposite sides of the injury. Passive materials did not recapitulate this effect, but it is not yet known which of the many possible biochemical and biophysical aspects of Anthrobot presence are required for this. Although the complex in-vivo dynamics (e.g., immune components, migratory cells, inflammatory signaling and so on) that may otherwise be observed in actual wounded tissues are not present in this simplified in-vitro neuronal injury model, so are the endogenous repair cues (e.g., chemical gradients that normally guide such repair processes), yet the Anthrobots were still able to facilitate the repair of a scratched neuronal monolayer. Future work will examine the functionality of Anthrobots in complex injury sites in vivo and identify which of their properties and active processes are mediating the effects.

Furthermore, the size of the Anthrobot to facilitate this repair can be adjusted. The tendency of the bots to fuse together and thus form different sized collectives (i.e., superbots) for different scratches can be controlled by modulating the number of Anthrobots cultured together in the same well for fusion, which happens only on days immediately following dissolution while the Anthrobot basal layers are still exposed and thus can mediate the bot-to-bot fusion. The finding is unexpected given these tissues' normal roles in the human body – the fact that wild-type cells from trachea will move over and heal neural tissues could not be predicted from any current molecular or tissue-level models. Thus, it is likely that screens for engineered interactions between body tissues in the context of motile bio-robotics and other preparations should be performed to uncover novel capabilities of cells and multicellular constructs. Likewise, future molecular biophysics and machine learning efforts could identify the specific signaling modality that is used by Anthrobots to induce neural repair in their vicinity, and thus harness this effect for therapeutic purposes.

Anthrobots are derived from adult human tissue, and in the future could be personalized for each patient, enabling safe in-vivo deployment of these robots in the human body without triggering an immune response. Once inoculated in the body via minimally invasive methods such as injection, various applications can be imagined, including but not limited to clearing plaque buildup in the arteries of atherosclerosis patients, bulldozing the excess mucus from the airways of cystic fibrosis patients, and locally delivering drugs of interest in target tissues. The possible applications will represent those arising from exploiting surprising novel behaviors of cells and engineering new ones via future synthetic biology payloads, such as novel enzymes, antibodies, and

other ways to manipulate the cells they traverse and interact with. They could also be used as avatars for personalized drug screening [90], having the advantage of behavior over simple organoids, which could be used to screen for a wider range of active, dynamic phenotypes.

Conclusion

We quantified in detail the morphogenetic and behavioral capacities that self-organized, clonally derived biobots can develop in culture from adult, genetically wild-type, human cells. We found correlations between their specific form and several modes of autonomous (self-driven) motile function and characterized the space of discrete characters of form and function that are not currently inferable from the standard target morphology associated with the human genome. We also found a surprising non-cell-autonomous functionality of Anthrobots - a repair property that likewise could not have been guessed in advance from existing frameworks describing the uses of organoids and other bioengineered structures.

Anthrobots may be able to be generated from other ciliated cells in the human body (e.g., oviductal epithelia or brain ependymal cells), and other cell types can be used for bots when autonomous motility is not needed (they can still perform various functions such as the healing we report here, or sensing/reporting, etc.). It may also be possible to induce a ciliation program in other body cell types. These data establish a research program with many unanswered questions for subsequent work. What other cells can Anthrobots be made of? What other behaviors might they exhibit, and in what environments? What other tissue types can they repair or affect in other ways? Can

transcriptional or physiological signatures be read out in living bots, that reflect their past and immediate interactions with surrounding cellular or molecular landscapes? Do they have preferences or primitive learning capacities [91], with respect to their traversal of richer environments? More fundamentally, these data reveal additional morphogenetic competencies of cells which could have implications for evolutionary developmental biology, as evolution of anatomical and functional features could be affected by the ability of the same genome to produce very diverse forms in different environments. Finally, this kind of new model system is a contribution to two key future efforts. The study of synthetic biological systems [10,16,92,93] is an essential complement to the standard set of phenotypic defaults available in the natural phylogenetic tree of Earth, revealing the adjacent possible in morphological and behavioral spaces [94,95]. Moreover, these systems offer a safe, highly tractable sandbox in which to learn to predict and control the surprising and multi-faceted system-level properties of multiscale complex systems.

Materials and Methods

Production of Anthrobots via NHBE culture

Normal human bronchial epithelial cells (NHBE) were sourced from Lonza Walkersville, MD (CC2540S). The cells were first thawed and seeded on a T150 flask containing bronchial epithelial growth medium (BEGM Lonza CC-3170) for 2D cell culture growth. Once the NHBEs were ~80% confluent, they were passaged into a 24-well-plate of Matrigel (Corning #354230) beds for 3D cell culture. The NHBEs were not passaged

past the 3rd passage. Each Anthrobot bed contained 500µL of 25% Matrigel, 0.1% 0.5nM retinoic acid (Sigma-Aldrich R2625) and in bronchial epithelial differentiation medium (BEDM, which is 50% BEGM without T3 and 50% high glucose DMEM without Sodium Pyruvate from Sigma #11-965-092) that was centrifuged for 5 seconds at 100 x g and prepared at least 4 hours before passaging the cells. We usually made 6 beds, but this number can be adjusted at discretion. The cells were re-suspended in 5% Matrigel, 95% BEDM and 0.1% 0.5nM RA and seeded directly onto the Anthrobot beds with 500µL per well at a 30,000 cells/mL concentration. Once seeded, the NHBEs were centrifuged for 5 seconds at 50 x g. On days 2 and 8, the NHBEs received a top feed containing 750µL 5% Matrigel, 95% BEDM, and 0.1% RA. On day 14, 500µL of the wells' contents was aspirated and 500µL of dispase (#D469) at concentration 2 mg/mL was added to each well. A mini cell scraper was used to break up the Anthrobot clumps and then followed by a 0.05% Triton coated pipette tip to mix up the Anthrobot with the dispase. The dispase was then incubated at 37°C for 1 hour with the pipetting process repeated every 15 minutes. During incubation, Pluristrainer Mini's with a 40 µm pore size (Fisher Scientific #431004050) were placed in wells of a fresh 24-well-plate that contained 2.5 mL of 0.05% Triton. After the incubation period, 250 µL of 1% 5mM EDTA in D-PBS was added into each well. The media in each well was then drawn up, using the Triton-coated tip, and added to the Triton-coated strainers. The NHBE spheroids in the strainer were rinsed with 1 mL of D-PBS then expelled onto a low adhesive dish by inverting the strainer over the dish and expelling 5 times 1 mL of BEDM through the bottom of the strainer. After all spheroids were in one dish, they were divided evenly amongst multiple 60mm dishes by using a Triton-coated pipette tip and a microscope to manually draw up and divide them.

0.5µL of 0.5nM retinoic acid was added into each dish once divided. For the next 14 days as the spheroids started moving, they required 0.5µL of 0.5nM retinoic acid every other day and a media change every 4 days. The media change was performed by swirling the Anthrobots to the center of the dish then collecting 2 mL of old media and adding 3 mL of fresh BEDM. This was done under a microscope to ensure no Anthrobots got aspirated. Finally, we created “superbot” assemblies by facilitating random self-aggregation of distinct Anthrobots that fuse to form larger structures. We accomplished this by transferring one well’s equivalent of Anthrobots into a 60mm dish, while keeping everything else constant.

Tracking timelapse videos

Timelapse videos of the Anthrobots were collected at 2.5 second intervals for a duration of 5 hours. The videos were contrast-enhanced using the video editing software ImageJ for optimal tracking and data that are within one bot length (~100um) from the edge of the vessel were omitted to prevent edge effect as a confounding factor. They were then processed to extract the trajectories of the Anthrobots utilizing the trackR function in the trackR package (version 0.5.1) for R developed by the Swarm Lab of NJIT. The software parameters were chosen manually in order to increase the accuracy of the tracking, following the instructions in the trackR package’s help section. Tracking errors such as the swapping, deletion or insertion of tracks were subsequently manually corrected using the trackFixer function from the same package.

Movement type analysis

From the extracted trajectories, the following metrics were computed: (i) the linear distance between the current position and the immediately preceding one; (ii) the linear speed at each position, approximated as the distance moved between the current position and the immediately preceding one during the time interval between these two positions; (iii) the heading of the bot at each position, approximated as the angle between the vector formed by the current position and the immediately preceding one and that formed by the Anthrobot position and the immediately following one; (iv) the angular speed of the bot at each position, approximated as the difference between the heading at the immediately preceding position and that at the current one during the time interval between the corresponding three positions required to calculate these two headings; (v) the time difference between each position.

Behavioral classification was then performed on non-overlapping 30-second blocks of trajectory. To determine how predictable a position change was, the linear speed, heading, and angular speed were estimated at each position to predict the coordinates of the following position. The error (Euclidean distance) between the predicted coordinates and the actual coordinates was then computed. For each complete 30-second block of trajectory (i.e., a block with no missing timestamp), total error over the entire block was calculated and normalized by the total distance traveled during that block to account for the artificial error amplification caused by predicting over longer distances. To separate active from inactive blocks, an automated classification method was used on the distribution of total normalized errors. A gamma mixture model with two components was fit to the data using the expectation maximization algorithm in the REBMIX function

from the rebmix package (version 2.12.0) for R [96]. The 30-second periods in the resulting cluster with the highest total normalized error were considered as inactive and excluded from further classification.

We then derived two metrics to describe each trajectory: (i) a “straightness” index computed as 1 minus the circular variance of the headings during the block (a value of 1 indicates a perfectly straight line) and (ii) a “gyration” index computed as 1 minus the circular variance of the angular speed during the block divided by the circular variance of the same angular speeds and their additive inverse, which helps in taking into account the magnitude of the angular speeds themselves (a value of 1 indicates a trajectory following a perfect circle).

The need for two indices arises from the fact that a straightness index alone cannot fully tease apart all different movement types due to its aggregate view of a trajectory. In other words, a low straightness index does not automatically translate into a perfectly circular bot, as we can see in Figure S6-a.1 and 6-a.2 with the arc trajectory. This is because the straightness index does not account for the time-dependent dynamics and thus ignores individual variations across frames. This is where the second movement metric, the gyration index, comes into play. To account for temporal information, we calculate the angular speed, which is the difference between successive headings divided by time between frames and thus has units of radians/ second. Figure S6B shows a bent trajectory and Figure S6C shows an arc trajectory, both of which have similar straightness indices. However, when we start looking at their temporal relationships using angular speeds, the behavior is entirely different. For the arc (Figure S6C), the variance of the

angular speed is very small since the change in heading of the trajectory each time is relatively consistent (the distribution shown in the histograms).

For the bent trajectory (Figure S6B), the variance of angular speed is much larger than the arc since for most of the trajectory the angular speed is close to 0 (it goes straight), but the bent portion has a very high angular speed, i.e., the angle changes very quickly. In general, the greater the absolute value of the angular speed the sharper the turn in the trajectory (zero is straight) and the greater the variance of the angular speeds, the less the consistency of the turns in the trajectory. A circle or arc usually has absolute values of the angular speed much greater than zero and low variation of angular speed. However, the gyration index alone cannot differentiate between all behaviors either. Let's look at a circular trajectory (Figure S6D). Even though the absolute values of the angular speeds between arcs and circles are different, the circle also ends up having a gyration index close to 1 since all the turns in a circle are highly consistent like in an arc and thus the variance of the angular speed for both is very small. This fact means the gyration index cannot segregate between arcs and circles, among other things, by itself. Interestingly, the straightness index is exceptional at separating arcs and circles. This shows that though either index alone cannot distinguish all movement types well, together they can accomplish much more.

To separate the trajectory blocks into categories of similar behavior after calculating the movement metrics, a cross-entropy clustering algorithm was used [97], and implemented in the cec function of the CEC package (version 0.10.2) for R [98]. This yielded us six categories, of which trajectories from categories numbered 3 and 4 were merged into categories numbered 1 and 2 respectively due to the difference being phenotypically

minimal. In the “behavioral space” as defined by the straightness and gyration indices, cluster 3 had the same straightness index range as cluster 1 and a lower gyration range between roughly 0.65 and 0.95, which represented trajectories that were highly circular but fell short of cluster 1 which represented “prototypical circulars”. Similarly, Cluster 4 had a slightly smaller straightness index range than cluster 2 (0.7 to 1 instead of 0.6 to 1) and higher gyration range between 0.1 and 0.55 which represented trajectories that were mostly linear but didn’t have a high enough gyration to be curvilinear or low enough gyration to be Cluster 2, a “prototypical linear”. The merge of the two clusters increased the average dissimilarity of the cluster, but it is a testament to how similar clusters 1 and 3, and 2 and 4 were already that their dissimilarity remains very low at ~0.09 and ~0.14 respectively. Last, to understand how the bots’ behaviors are distributed relative to each other, transition probabilities between each behavioral category were estimated by calculating the proportion of times a block of a given category is followed by a block of the same or another category. This was then presented in the form of a Markov Chain.

Immunocytochemistry / Immunofluorescence

Anthrobots were collected in Pluristrainer Mini’s with a 40-micron pore size (Fisher Scientific #431004050) and fixed with 4% paraformaldehyde at room temperature for 30 minutes. Following PBS washes, blocking and permeabilization were performed for 1 hour at room temperature on a rocker in a blocking buffer consisting of phosphate-buffered saline with 10% normal goat serum, 1% bovine serum albumin, and .15% triton x-100. Anthrobots were then incubated with mouse anti-acetylated tubulin (Sigma-Aldrich #T7451) primary antibodies at 1:250 dilution factor in blocking buffer for 24 hours at 4oC

on a rocker. The primary antibodies were labeled with Alexa Fluor 647 donkey anti-mouse (Thermo Fisher Scientific #A31571) secondary antibodies, at 1:500 dilutions in blocking buffer, for 1 hour at room temperature on a rocker. Lastly, Anthrobots were incubated with Alexa Fluor 594-conjugated mouse anti-ZO-1 (Thermo Fisher Scientific #339194) at a 1:100 dilution in blocking buffer for 24 hours at 4oC on a rocker. Anthrobots were mounted on glass-bottom 96-well plates in ProLong Glass Antifade Mountant with NucBlue (Thermo Fisher Scientific #P36981). Neuronal tissues were fixed, blocked and stained using the same protocol, except by using Beta III Tubulin (Tuj1) (Abcam #ab18207) as the primary antibody for staining the hiNSCs. Images were collected using a Lecia SP8 FLIM with a 25x water immersion objective. Z-stack step size=3 micron unless otherwise specified.

Morphotype analysis

To find whether there were any unique morphological types like was the case with movement types, each spheroid was processed through a custom-made analysis pipeline (code attached). First, a 3D model of the bot was created in R where the points corresponding to the body and the cilia were clearly indicated. For this, first the cilia channel was isolated from the LIF images of the bots; these cilia-only images were then ran through CiliaQ [99] using the RenyiEntropy algorithm for detection. These binarized cilia were then imported into our code, along with the points that comprised the body. These “body points” were extracted using the “body channel” of the LIF images by first running the pixels through a logistic transform then thresholding the pixels based on the signal to

noise ratio, calculated by using a median filter and comparing the points before (“signal + noise”) to after (“only signal”).

Due to the large volume of body points, to reduce the points to a manageable amount, we first found the outlines of each slice of the spheroid by using a concave hull using the Concaveman package (version 1.1.0) [100]. The cilia points were then projected on the nearest body points by simply choosing the nearest one by distance to get the shadow of the cilia on the body.

The structural index variable Cilia Points was calculated by counting the number of unique projected points on the body. Then, the dbscan package (version 1.1-10) [101] function in R was used to find the clusters of cilia. The number of points that fell outside of clusters with this definition were defined as Noise Points.

Following this step, we computed the spanning ellipsoid of the body points by using the ‘ellipsoidhull’ function from the cluster package (version 2.1.3) [102]. The Max Radius variable was calculated directly by the function, and Aspect was defined as the ratio of the largest radius to the shortest radius, all quantities computed by the function. Finally, we used the ‘ashape3D’ function from the alphashape3d package (version 1.3.1) [103] to generate a 3D alpha hull of the body points, and used the mesh to get the surface area of each spheroid.

Cilia Points/Area was defined as the Cilia Points variable divided by the calculated surface area. Similarly, the Shape Smoothness was defined as the ratio of the volume of the 3D alpha hull to the volume of the spanning ellipsoid. Finally, we found the center of the bot by finding the sum of the centroids of each triangle that makes up the alpha hull weighted by area of the triangle. Polarity was defined as the norm of the vectors from the

center to each cilia point divided by the sum of the norm of each vector. The Cilia Distribution Homogeneity was defined as 1 - D statistic of the two sample Kolmogorov-Smirnov test, where sample A is the 1st nearest neighbor (1NN) distances for the cilia, and sample B the 1NN distances if the same number of cilia points were distributed close to uniformly but randomly across the surface of the bot. After these analyses were carried out, we ran the dataset through a Principal Components Analysis with centering and scaling. Afterwards, a hierarchical clustering was carried out on the resultant dataset with the Ward.D2 method and the resulting classification was plotted as above. In total, 350 bots were put through the pipeline and into the following PCA and included Movers, Nonmovers, Linears and Circulars. Further details can be seen in the code.

To get a confidence interval for the absolute value of the loadings, we bootstrapped the loading value by sampling 250 bots from the 350 that we have, 10 times. We then took the loadings value for the 1st and the 2nd primary component for all 8 variables and calculated the mean and 95% Confidence Interval for the loadings for the PC in question. If there was overlap between the CI of the loadings, they were assigned the same rank, otherwise they were assigned different ranks. Ranks were relative to the “highest” contributor of the rank; i.e, for PC1, Shape Smoothness had overlap with Max Radius, but it also had overlap with Cilia Distribution Homogeneity. However, Cilia Distribution Homogeneity did not overlap with Max Radius. Max Radius had the highest upper limit of the CI among the 3 variables in question, and thus Shape Smoothness was co-ranked #1 along with Max Diameter, but Cilia Distribution Homogeneity was not.

Morphotype & movement type overlap

After finding trends among behavioral and morphological data, we decided to see if there was any potential overlap between the two. To eke out any possible correlation, we first chose to use categories of spheroids behaviorally orthogonal to movers, the non-movers. The goal was to observe whether there is any overlap between the morphology of movers and non-movers. Similarly, we had four potential behavioral types that could overlap with our morphological clusters. Eclectics could not be included in the analysis since they are an aggregate of multiple inconsistent patterns and highly uncommitted to their behavior (Figure 2G), and thus cannot be used in a bot-level analysis (instead of period). Circulars and Linears on the other hand were highly committed behavioral types that were orthogonal to each other (had little to no interconversion on the Markov plot) and prototypes of two extreme movement types with high variability between them. Consequently, the Curvilinear behavioral subtype was also not included since it lacked orthogonality with both Circulars and Linears due to shared traits between them. The morphological indices for each spheroid were calculated as outlined in the methods for the previous sections, and then clustered with Circulars, Linears, Nonmovers and Movers together. To measure the significance of the overlap, if any, between clusters, we decided to use a Fisher test to compute whether the proportion of a certain behavior per cluster type was different from the others. We ran the test twice, once to see if there were any significant differences in number of nonmovers per cluster, and once to compute the difference in the ratio between circulars and linears per cluster. It showed that the proportion of nonmovers in Cluster 1 vs. Clusters 2 and 3 were significantly different with an average p=2.6*10e-6 and 3.5*10e-8 respectively Cluster 2 and 3 also had a

statistically significant difference in number of nonmovers (p=0.01) which is understandable, since Cluster 2 had no non-movers. For Circular/Straight, Cluster 2 vs. 3 were significantly different with p=0.00011, and Cluster 1 had no Circulars nor Straights.

Motility orientation alignment & movement axis analysis for bilateral symmetry

The generated tracks were analyzed alongside Z-stacks of designated Anthrobot from a confocal microscope to see if their morphology was connected to their movement. ImageJ was used to compile the slices of the Anthrobot so that a 3D model could be generated and rotated to render a transformation that visually matches a random frame of the Anthrobot from the timelapse. This random selection could be done as the Anthrobot, despite moving around, did not tend to roll and therefore generally maintained the same orientation throughout a timelapse. Additionally, they often moved with a specific side that always faced forward that was designated as a heading. To see if biases in cilia patterns to one side or lack thereof on an Anthrobot affected its movement this heading would serve as the axis along which a plane of symmetry would be extended to bisect the bot. This plane would be defined by 3 points on the bot along this axis, one placed at the centermost point of the axis within the bot, one on the part of the bot that most visually served as the heading in the video and one on the opposite point of the bot from the heading.

Bilateral Symmetry Along Movement and Other Axes

After realizing that polarity could play a key role in determining movement type, we decided to see whether the symmetry across the movement axis had any trends compared to the other axes. To calculate this, we followed the procedure used in both Fig 3 and Fig 4 to get representations of Cilia on the body of the bot, then project these representations onto the plane of symmetry defined by the points obtained in the Motility orientation alignment section. The side of the plane (movement axis) each cilia point belonged to was noted using the sign of the dot product of the normal of the plane and the vector to the cilia point. Finally, to better distinguish whether the cilia distribution played a role in movement type (linear vs. circular) we created the Bilateral Symmetry index. This index was modified from the Chamfer distance, and was calculated as the sum of the median/ mean of the distances between all points in set A and the closest point in set B and the median/ mean of the distances between all points in set B and the closest point in set A. To calculate the index, the cilia points were projected onto the plane defined by the three points in the section below. Set A and Set B then became the points projected from one or the other side, respectively, after which the modified Chamfer index was calculated for the two sets using the createTree() function of the SearchTrees package. The statistics used to calculate the asymmetricality between both sides were the difference in points between the two hemispheres, the difference in points/ total cilia points, the median and the mean modified Chamfer distance. In the end, they were visualized and clustered using a PCA to see trends (see code).

In the case of figure 4E, instead of calculating the asymmetry statistics after getting the equation of the plane, we then used the Rodrigues' rotation formula to rotate the

normal (and thus the plane) with the fixed intersection being the center of the bot. Rotations of 45, 90 and 135 degrees were used yielding 4 axes (in the form of plane equations) including the movement axis. To eliminate the z-axis we used a PCA to get the rotation matrix to convert the projected cilia points from 3D to 2D and calculated the Chamfer distance using the formula described at https://github.com/UM-ARM-Lab/Chamfer-Distance-API, expect that we didn't square point distances. This statistic was calculated along for the cilia of all linears and circulars and put into a paired Wilcoxon rank-sum test with an alternative hypothesis of "greater" and "less" for circulars and linears respectively to see if the movement axis was "more asymmetrical" or "less asymmetrical" respectively. For the body we did the same procedure, with the exception that our statistics now involved finding the distance of the body points from the centre of the bot (once again segregated into two hemispheres with the dot product). Then, we used the KS test to calculate a D-statistic which had greater values the more dissimilar the two distance distributions for both hemispheres were. Just like the cilia we then used a paired Wilcoxon rank-sum test with an alternative hypothesis of "greater" and "less" for circulars and linears respectively to see if the movement axis was "more asymmetrical" or "less asymmetrical" respectively.

Neuronal culture

We followed a previously established protocol for creating the neuronal cultures [78] which is summarized as follows. A 150 cm dish was first coated with 0.1% gelatin for 20 minutes and then aspirated off before seeding mouse embryonic fibroblasts (ATCC #SCRC-1008) in MEF growth media (89% DMEM GlutaMAX, 10% Fetal Bovine Serum,

and 1% Anti-anti). Once the MEFs were confluent, they were inactivated by adding 20 mL of MEF growth media containing 500 µL of 10µg/mL mitomycin C (Sigma #M4287) and incubating for 2-3 hours at 37°C. After incubation, the MEF growth media + mitomycin C media was replaced with hiNSCs at a density of 1/10 of a confluent target vessel in 25 mL of hiNSC growth media (77.6% Knockout DMEM, 20.20% KOSR, 1% GlutaMAX, 1% Anti-anti, 0.18% 2-mercaptoethanol with 0.1 % of 20 ng/mL bFGF). The day after seeding the hiNSCs required a media change where all the old media was aspirated off, and 25 mL of fresh hiNSCs growth media was added. Media changes were performed every other day until the hiNSCs were 80-85% confluent. 3 hours before performing the differentiation, the destination vessels were first coated with .1mg/mL poly-d-lysine (enough to coat the bottom of the wells) for one hour at room temp, and then the PDL was aspirated before adding in 10ug/mL laminin in DPBS (enough to coat the bottom) for 2 hours at 37°C. In the differentiation, the hiNSCs first went through one D-PBS wash before adding TrypLE Select for 3-5 min to detach the cells from the plate. The cells were then collected and spun down for 3 minutes at 500g then resuspended in neurobasal differentiation media (96% Neurobasal Media, 2% B-27 supplement, 1% GlutaMAX, 1% Anti-anti). The hiNSCs were seeded at a concentration of 100,000 cells/cm^2. Once the hiNSCs were in differentiation, there was a media change the day preceding their differentiation and then every other day from there.

Traversal video tracking and analysis

To better explain the relationship between bot trajectory and movement in certain environments, we tried to relate the scratch edge to the actual movement of the bot. The

steps taken before analysis involved (i) creating a background image prototype from the .czi recording, (ii) verifying the quality of the background image and saving as .png file, (iii) tracking the bot, (iv) extracting the coordinates of the scratch, and (v) checking whether tracking was correctly carried out by generating a video with a beacon on the bot.

This procedure was carried out on 30+ files and yielded 20 usable datasets, which were whittled down to 17 after a manual check of tracking quality and excluding videos where bots never touched the scratch wall. Using the coordinates of the scratch walls and the tracking of the bot, we used the Rbioformats (version 0.0.74) [104] and Rvision (version 0.6.2) [105] package tools to test (1) whether bots are more in contact with the scratch when they have a higher rotational tendency and (2) when moving on tissue, whether faster bots tend to cover more area i.e., explore better. The lm() function was used to model the data after calculation of proportion of bot on tissue, instantaneous angular velocity and linear speed as variables. Before each model was approved, diagnostics were run on the model using the DHARMa package which included analysis of the residuals.

Afterwards, in order to take a better look at the nuances of interactions between bots and scratches, we decided to limit the data and remove any videos that had bots with very low rotational tendency (<0.33) since they were not stable enough in their rotational behavior. Bots with very high rotational tendency (>0.7) were removed since they were prone to skidding instead of interacting with the scratch walls. Finally, bots whose tracking videos were not optimal i.e they frequently went backward or circularly in the scratch were removed since they did not have consistent forward movement that could be correlated with the scratch wall. After all these removals, our dataset ended up

with 13 examples of scratch-bot interactions which could be effectively analyzed. The Gyration was simply the Rotational Tendency values renamed. Our Scratch-Trajectory Similarity metric was calculated as the larger absolute value of the correlation between the heading angle of the trajectory and the heading angles of the scratch from the surface perpendicular to the bot. These correlation values were then modelled using the lm() function with an expectation of a quadratic relationship for Gyration. The specifics can be seen in the attached code.

Traversal Video Processing

Traversal videos of bots moving along a scratch within a neuron plate were processed via Adobe Illustrator to see if the bot faithfully followed the edge of the scratch. The first method of processing aligned the center of the scratch at a horizontal line parallel to the bottom of the screen and placed a point on the center of the bot at each frame of the video as well as straight above and below this point on the edges of the scratch. Lines were made to connect each respective type of point for both of the edges of the scratch and the position of the bot. The output of this for further analysis was a set of coordinates of the end of each line derived from rendering these series of lines as a vector file and exported as text.

Neuronal tissue density analysis

To investigate whether these “bridges” were actually akin to neurons, we decided to analyze the pixel densities of various areas on and surrounding the bridge. In order to prevent confusions regarding this process with regard to intensity of color, we binarized

the image on ImageJ. If the automatic thresholding did not visually appear similar to the raw image, we adjusted the threshold manually. We ended up with six areas of interest: the neurons above the bridge, below the bridge, to the left but adjacent to the left but far, and to the right, both adjacent and far. These areas were defined relative to a FIJI ROI box on the neuronal bridge which tried to encompass the width of the bridge and the height close to the narrowest point of the scratch channel that we would interact with. A line of one bridge length or lower if the image size required smaller lines to fit the boxes was used in the vertical and horizontal directions (called hereafter as “bridge length”). The above and below bridge measurements were taken by placing the bounding box one vertical bridge length from the box on the neuronal ridge. The adjacent areas on both sides were defined as 1 horizontal bridge length away from the bridge in the scratch. The far areas were 1 bridge length beyond the adjacent areas. The far and adjacent boxes were (vertically) adjusted so they overlaid the scratch as much as possible (Figure S9). Finally, we used Analyze>Histogram in FIJI to get the size of the box (which was constant) and the number of pixels of scratch tissue (in black) and calculated the proportion. We then used an unpaired two sample T-test with unequal standard deviation to calculate the significance of the difference, if any.

Statistical Analysis

For all analyses in the paper, the p-value to symbol correspondence was that a range of 0 to 0.0001 corresponded to ****, 0.0001 to 0.001 corresponded to ***, 0.001 to 0.01 corresponded to **, 0.01 to 0.05 corresponded to * and 0.05 to 1 corresponded to ns. Additionally, all significance tests were evaluated at an alpha value of 0.05. Unless

otherwise specified, the alternative hypothesis was always two-sided for t-tests. For all statistical analyses listed below we used the Rstudio computational/ statistical software.

For Figure 2, we analyzed tracks from 197 bots for 5 hours, collected across 47 timelapse videos (each video featuring 4-5 bots). In the pre-processing step, we omitted data that is within one bot length (~100um) from the edge of the vessel to prevent edge effect as a confounding factor, which yielded a final of 42235 individual 30-second periods. After cross-entropy clustering these periods, we used a t-test to analyze cluster-specific differences in active periods (with cluster 1 having 6004 periods, cluster 2 with 6700, cluster 3 with 3436 and cluster 4 with 2384), which were further analyzed as shown on the figure. There were 23711 inactive periods that were excluded from this downstream analysis.

For Figure 3, the pre-processing step involved binarizing cilia vs body masses of 350 bots (each represented in 3D via confocal Z-stack images) through CiliaQ [38] as described in the methods above. The data obtained from these 350 bots were further clustered into 3 groups with sizes of 125, 24 and 201 for clusters 1,2 and 3 respectively. To check which of the 8 variables that were used to compute the PCA were significant for each cluster, we ran a two-sided, two-sample t-test on all pairs of clusters, for all 8 variables.

For Figure 4, we used the same full set of data for 350 bots as figure 3, which were still clustered into 3 groups with sizes of 125, 24 and 201 for clusters 1,2 and 3 respectively. Of these 350, we had specific information on type of movement for 28 bots (“displacers” - circulars and linears). Thus, of these 350, we then focused on 28 bots, 15 circular and 13 straight. These were analyzed for various metrics of asymmetry

(difference between the two hemispheres in number of cilia, or chamfer distance of the hemispheres of cilia etc.) along the movement axis and the axis that was 90 degrees offset from the movement axis as described in methods above. We then measured the change in the chamfer distance asymmetry statistic from the 90-degree offset to the movement axis (asymmetry difference = asymmetry around 90 degree offset – asymmetry around the movement axis) for circulars (n = 15) and linears (n =13) with a two-sided one sample t-test for each with a significant result for circulars (p = 0.0482) but not linears (p = 0.1116).

For Figure 5 during preprocessing, we excluded videos where the bot never touched the scratch wall as described in the methods above. A t-test for the slope was run on the relationship between bots' rotational tendency and proportion of bot on tissue which yielded a significant (p=0.017, slope 1.15, n = 17) result. Similarly, when we compared the relationship between bot linear speed and the proportion of bot on tissue using a t-test again, we received a significant result (p=0.031, slope 0.0082, n =17). For a subset of these 17 bots (dataset constrained to non-stalling bots with rotational tendencies between 0.33 and 0.7 and viable tracking videos as described in methods above), we initially tried to fit a linear model of the relationship between bot rotational tendency and scratch-trajectory similarity metric. The residuals of this analysis were not centered around a mean of 0 but rather followed a visibly quadratic trend (Figure S9). This suggested a quadratic model would be a better fit for the relationship between the two. We ran the t-test for the significance of this quadratic relationship which was significant (p=0.006, n=13).

For Figure 6, we ran a two-sample t-test pairwise with each category to characterize the pixel density of these various areas (gap closure site, native tissue, sites adjacent and distal to the gap closure sites) for all bridges where the connectivity to both sides of the scratch was maintained throughout the 3-day experiment, which was 50% of the total N=10. Difference between gap closure site and native[106] tissue is insignificant ($p = 0.37$), while the difference between the gap closure site and both adjacent and distal scratch sites are significant (w/ $p = 0.006$ and $p = 0.005$, respectively).

Supplemental Figures

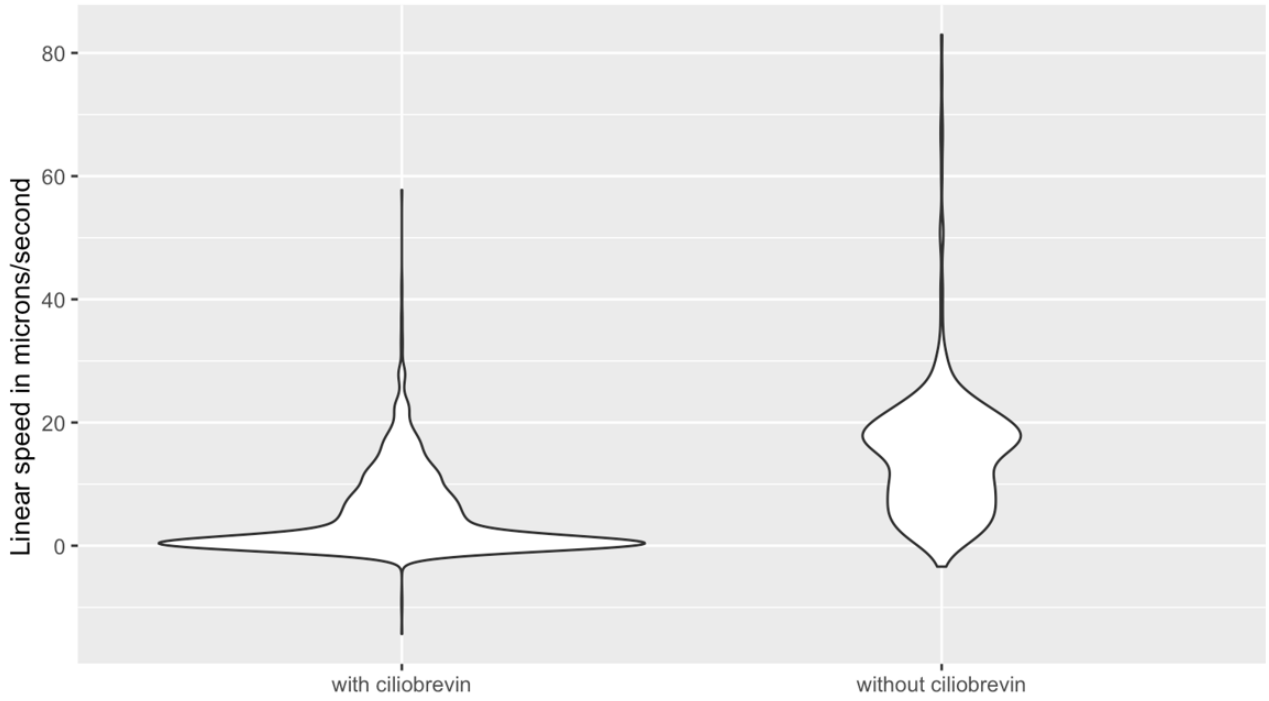

Figure 7 i.e., S1 Characterization of motility in terms of linear speed right after and prior to administration of ciliobrevin, a cilia-blocking agent.

Significant drop in speed ($p<0.0001$, using T-test) is observed.

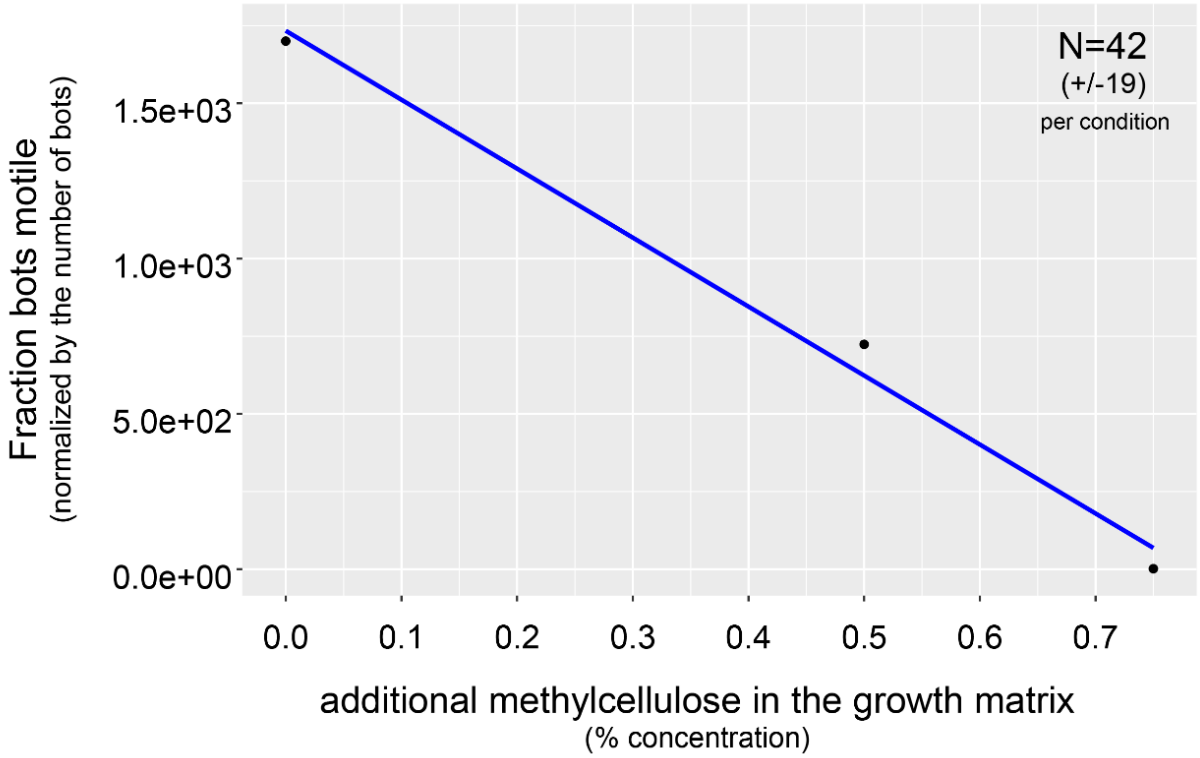

Figure 8 i.e., S2 Fraction of bots that show motility decreases as the matrix viscosity increases.

Viscosity modulation is mediated by addition of methyl cellulose into the Matrigel. Resultant linear regression of matrix viscosity (0 vs 0.5 vs. 0.75%) as compared to the # of motile bots (weighed by the total number of bots) revealed a linear decreasing trend with a significant negative slope ($p = 0.044$).

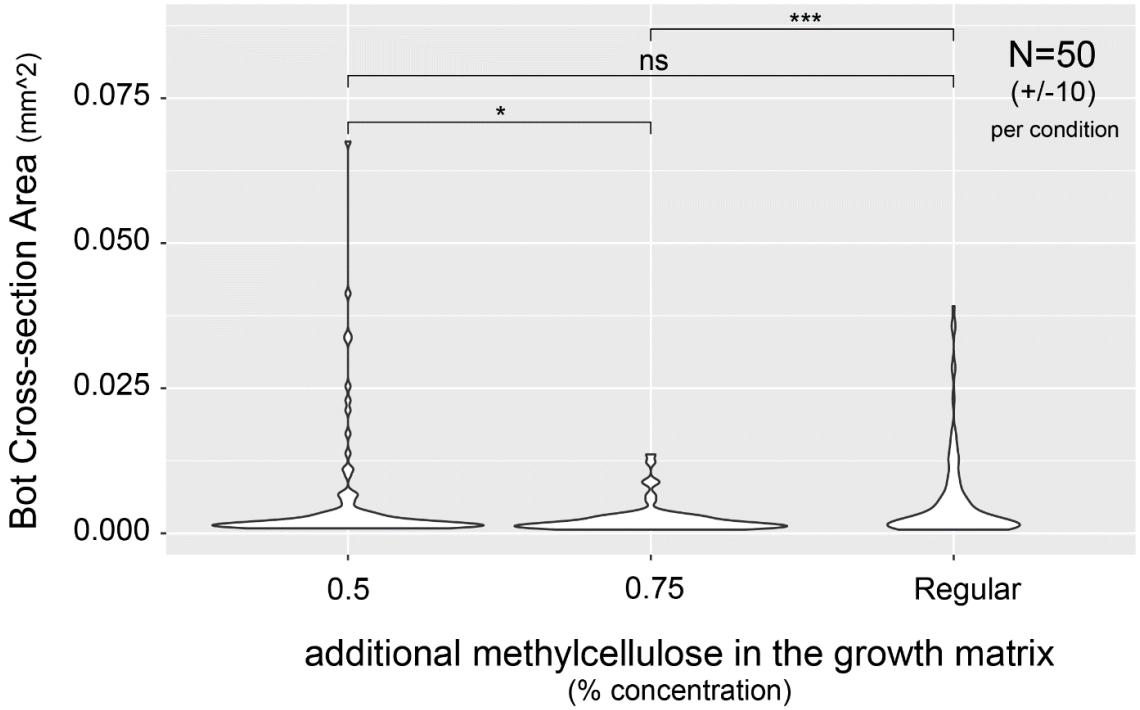

Figure 9 i.e., S3 Matrix viscosity influences the size of Anthrobots.

Viscosity modulation is mediated by addition of methyl cellulose into the Matrigel. While reducing the medium density by a factor of two did not significantly affect the area of the bots produced ($p = 0.84$), the density of 75% of baseline medium resulted in significantly smaller bot sizes when compared with bots from both 0.5 and baseline densities ($p = 0.016$ and $p = 0.0003$ respectively).

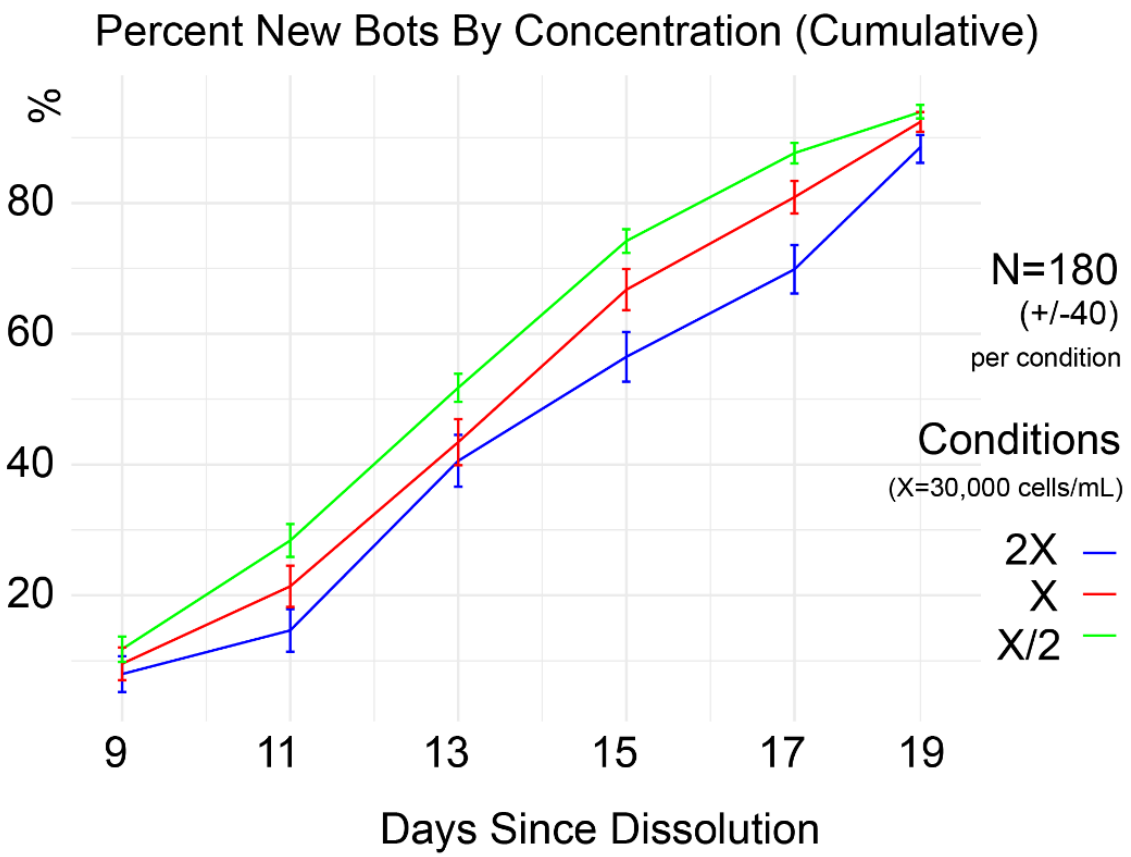

Figure 10 i.e., S4 Initial seeding density of individual cells is a key variable that influences the fraction of spheroids reaching motility at a given timepoint.

We allowed bots to form as in the described protocol at a baseline concentration of 30,000cells/mL (X), as well as varied this number to half (X/2) and double (2X) and counted the number of spheroids becoming motile each day. We saw that the 0.5x concentration formed significantly more bots than the 2x concentration on Day 11-Day 20 with p values ranging from <0.0001 to 0.0206 for individual time points measured (Day 11,13,15,17,20 respectively). On Days 15 and 17, the Regular concentration formed significantly more bots than 2x concentration with p = 0.0434 and p = 0.0184 respectively. The 0.5x concentration formed significantly more bots than the baseline concentration on Day 17 with p = 0.0323.

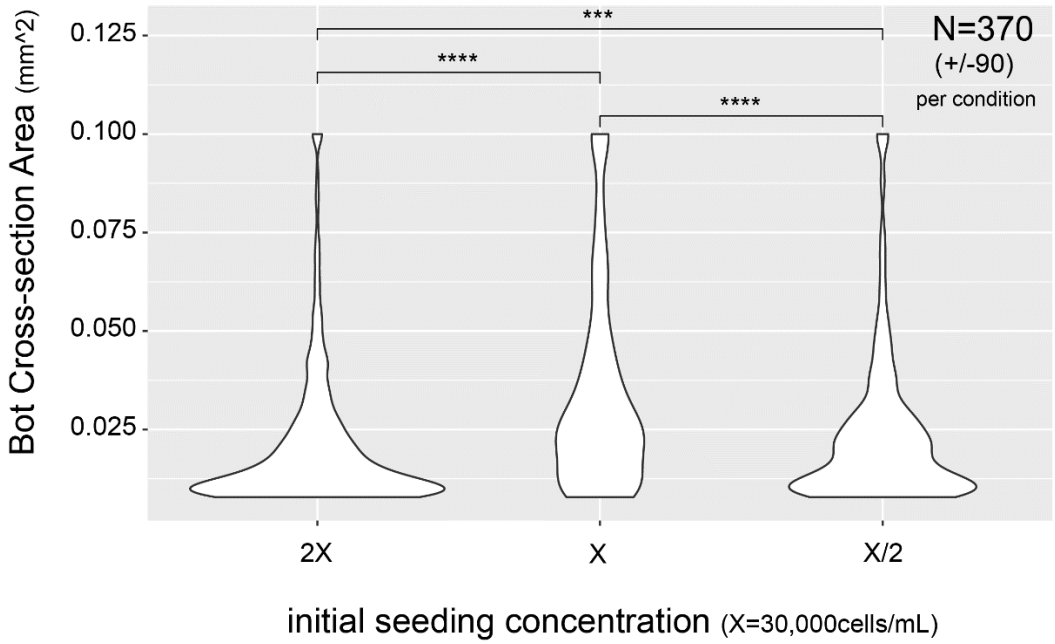

Figure 11 i.e., S5 Initial seeding density of individual cells is a key variable that may influence the size of Anthrobots.

We allowed bots to form as in the described protocol at a concentration of 30,000cells/mL (X), as well as varied this number to half (X/2) and double (2X) and measured the average size immediately upon dissolution from matrix. The size of the formed bots was drastically different, with the average areas being 2.04*10^-4, 3.35*10^-4 and 2.37*10^-4 cm^2 for 2x, Regular and 0.5x concentrations respectively. These averages were all statistically distinct from each other, with $p < 2.2e-16$ for 2x vs. Regular, $p = 0.0002469$ for 2x vs. 0.5x and $p = 4.494*10^{-13}$ for Regular vs. 0.5x. These results suggest that our experimental concentration does affect size, and extreme concentrations lead to smaller bots in general.

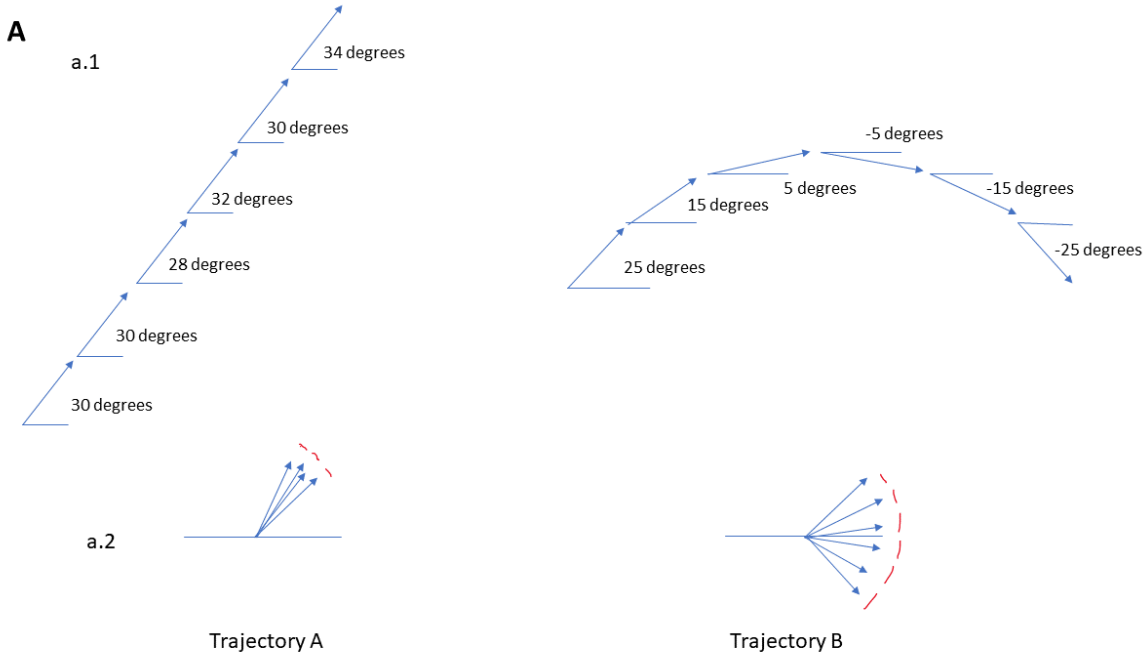
A
a.1
34 degrees
30 degrees
32 degrees
28 degrees
30 degrees
30 degrees
-5 degrees
5 degrees
15 degrees
-15 degrees
25 degrees
-25 degrees
a.2
Trajectory A
Trajectory B

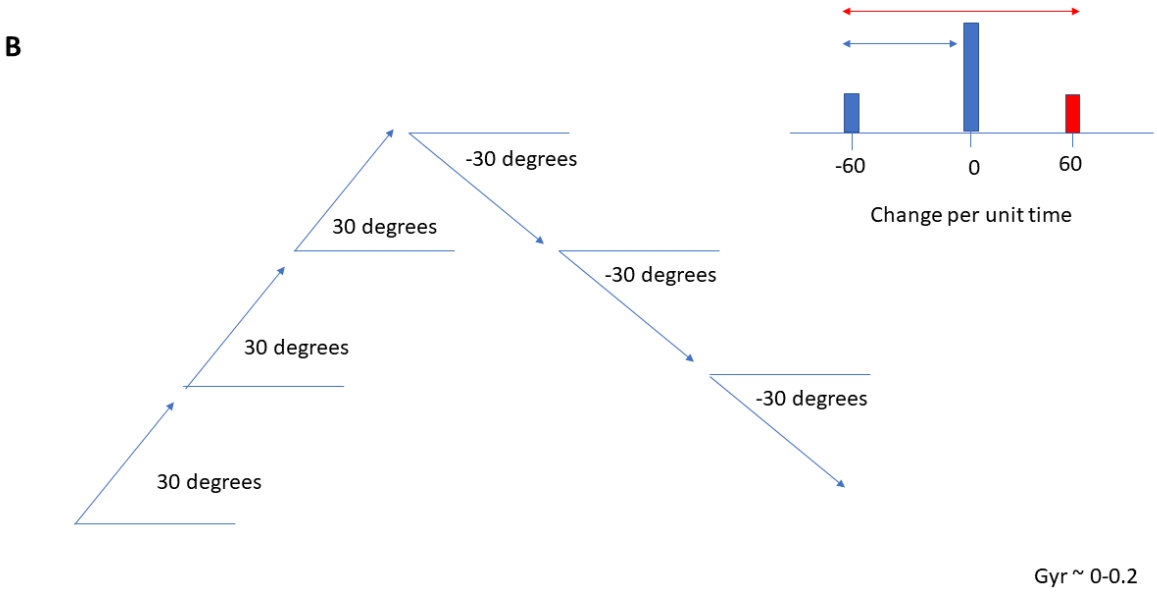
B
-30 degrees
30 degrees
-30 degrees
30 degrees
-30 degrees
30 degrees
-60
0
60
Change per unit time

Gyr ~ 0-0.2

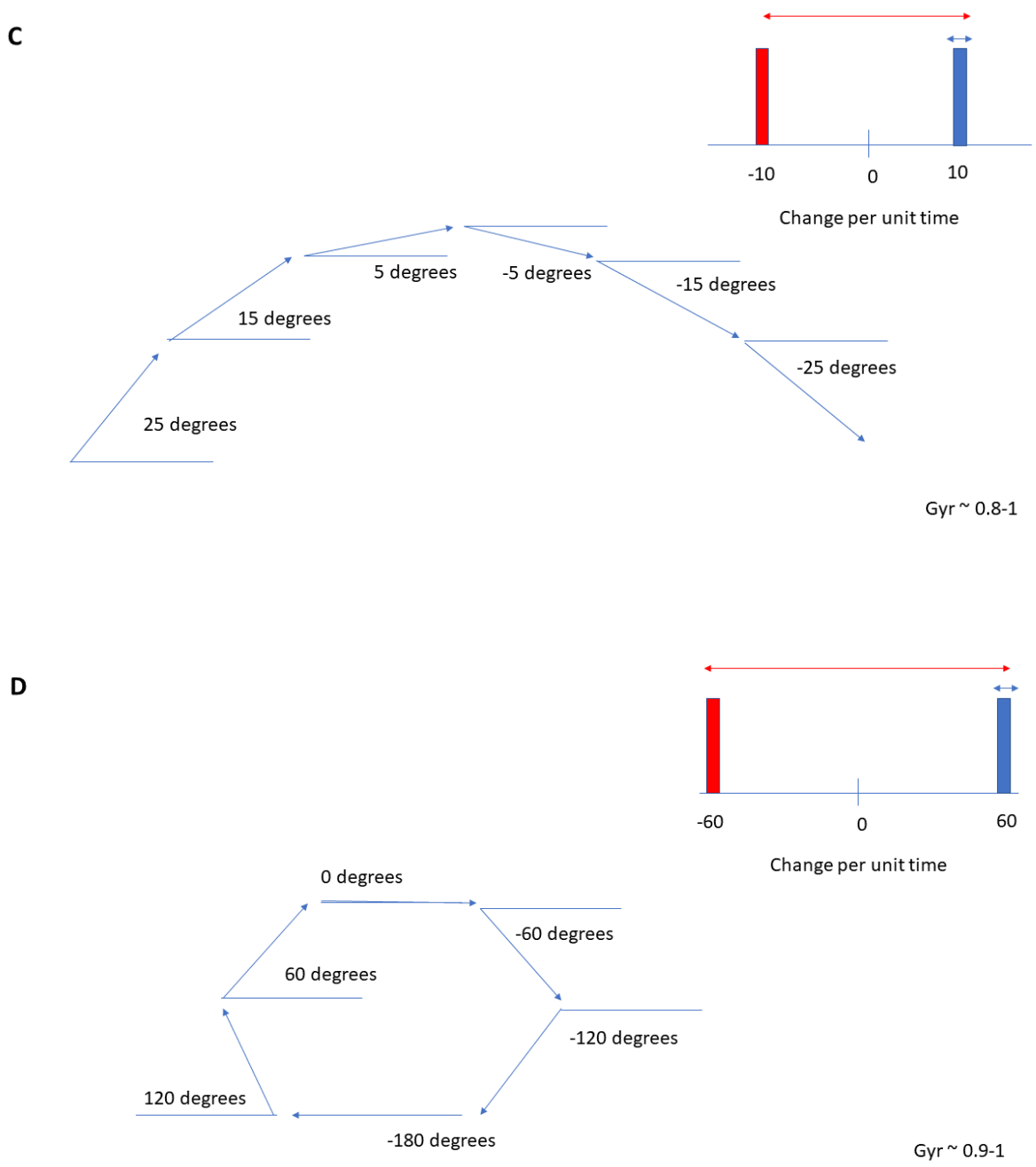

Figure 12 i.e., S6 Sample trajectories that reference a relative x-axis to find heading angle.

(A) Visual representation of straightness index, which calculates spread of headings as a whole without taking into account temporal dynamics. (B, C, D) Visual representation of gyration index, which includes the temporal aspect and calculates spread of change in headings relative to their magnitude. Graphically, it is represented as the ratio of the blue

length (original circular variance) to the red length (circular variance of the original angular speeds and their additive inverse) on the histograms.

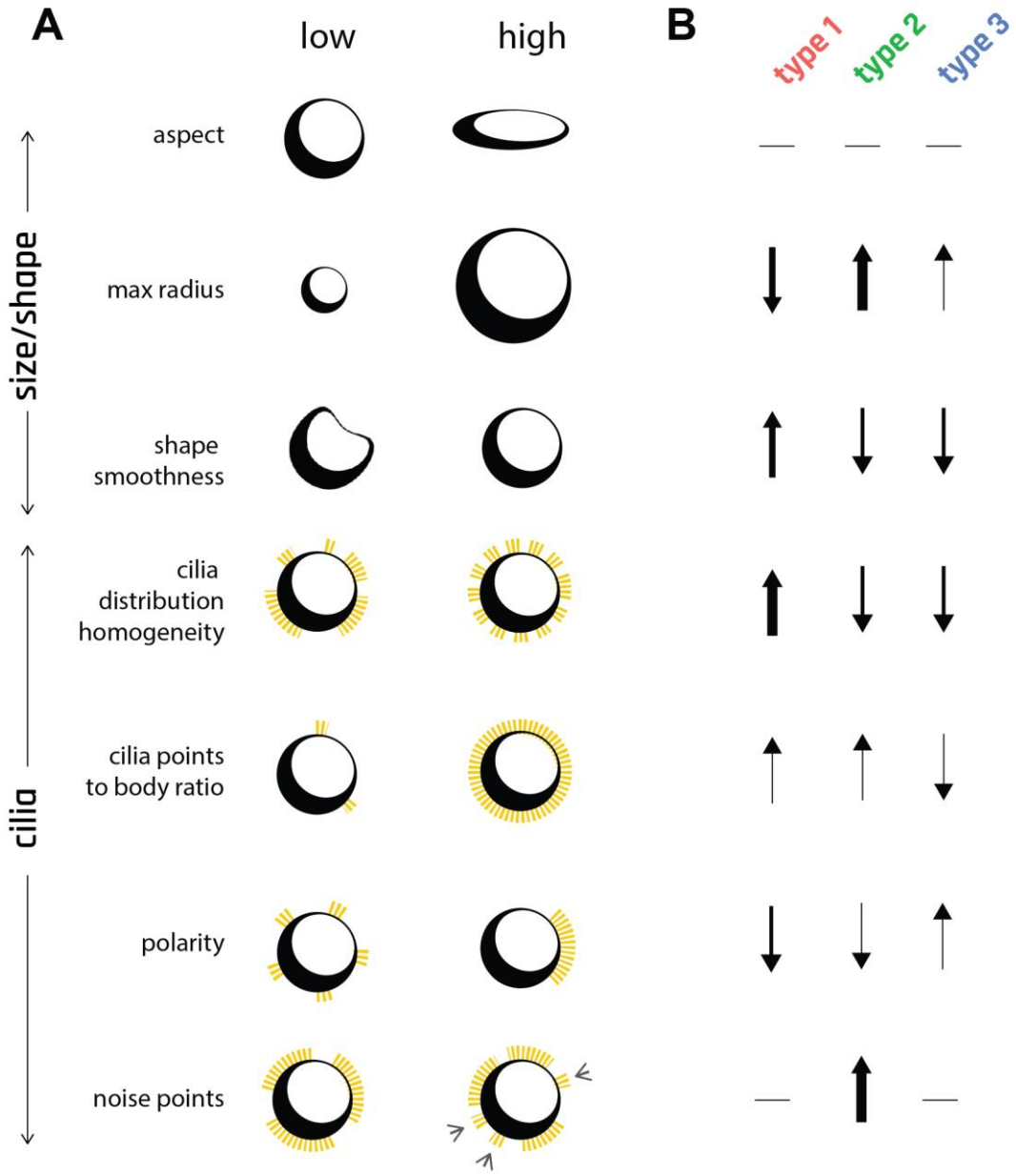

Figure 13 i.e., S7 Eight morphological indices were used to characterize Anthrobot morphotypes.

(A) Visual summary of morphological indices at their extreme points (low, high). (B) Graphic summary of boxplots on Figure 3D, describing 3 different morphotypes. Arrow thicknesses are correlated with the # of standard deviations between a given morphotype's mean vs the overall population mean for a particular morphological index.

45 Degrees

	Circular	Linear
Cilia	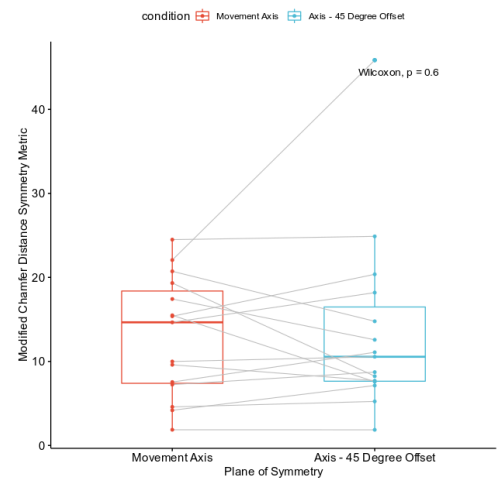	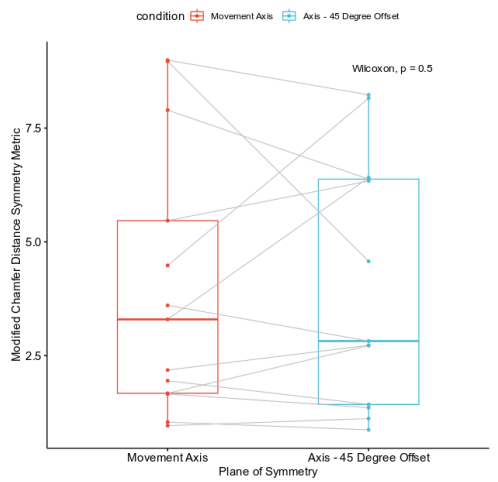
Body	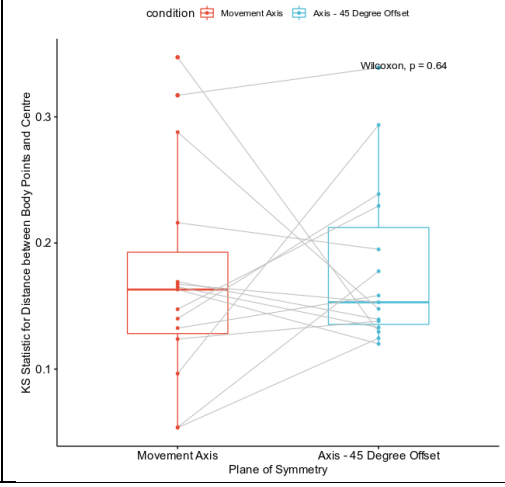	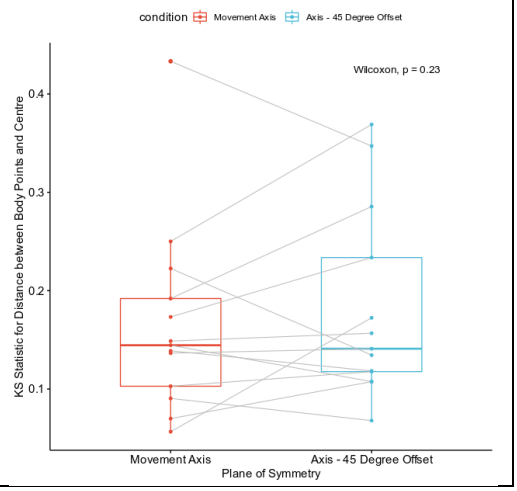

90 Degrees

	Circular	Linear
Cilia	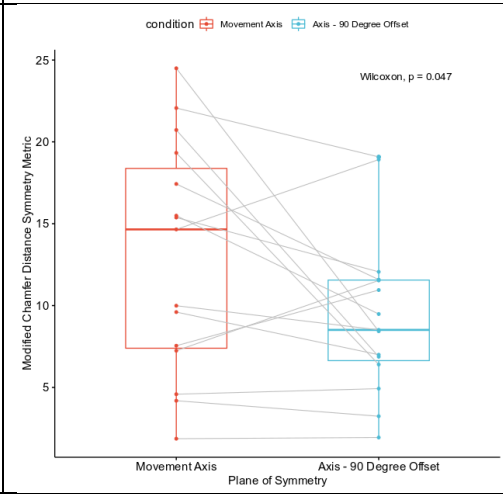	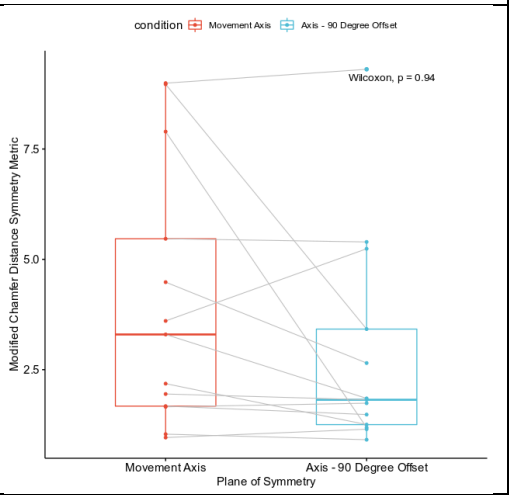
Body	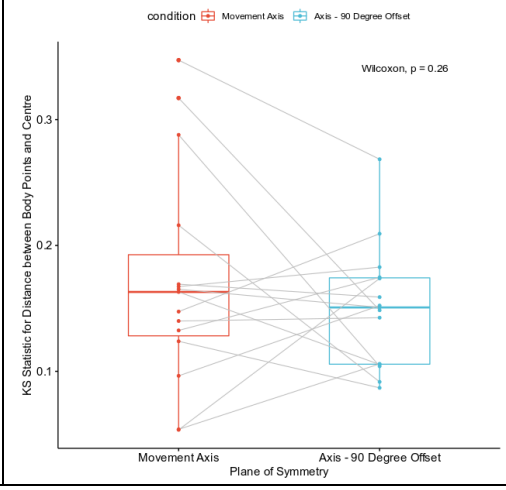	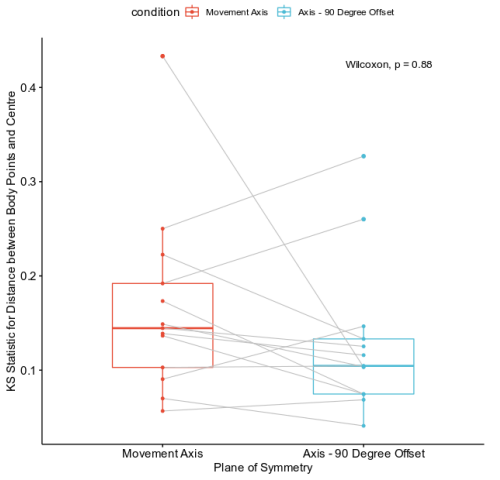

135 Degrees

	Circular	Linear
Cilia	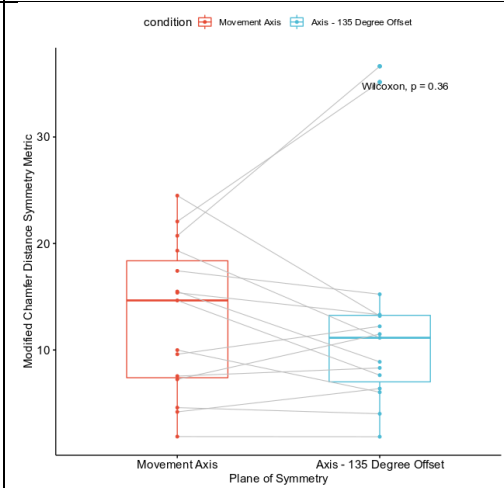	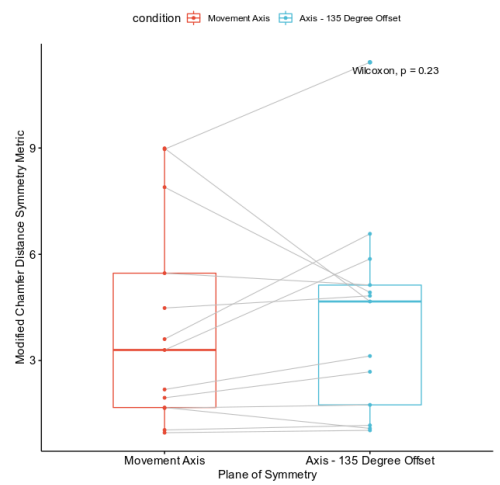
Body	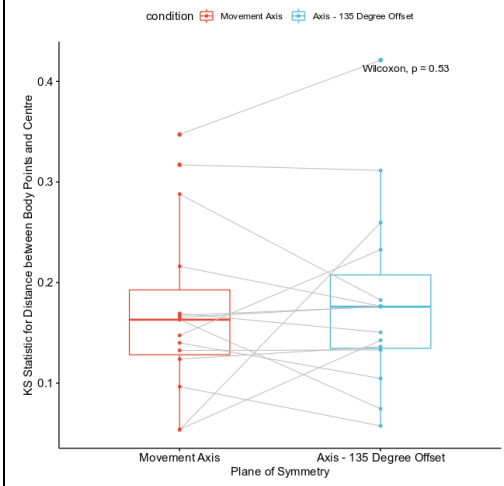	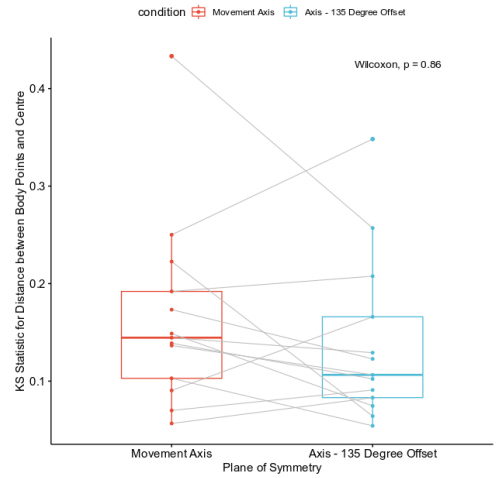

Figure 14 i.e., S8 Difference in asymmetry of cilia distribution and body shape between linear and circular bots.

Three separate analyses in respect to the movement axis and its 45, 90, and 135-degree offset axes.

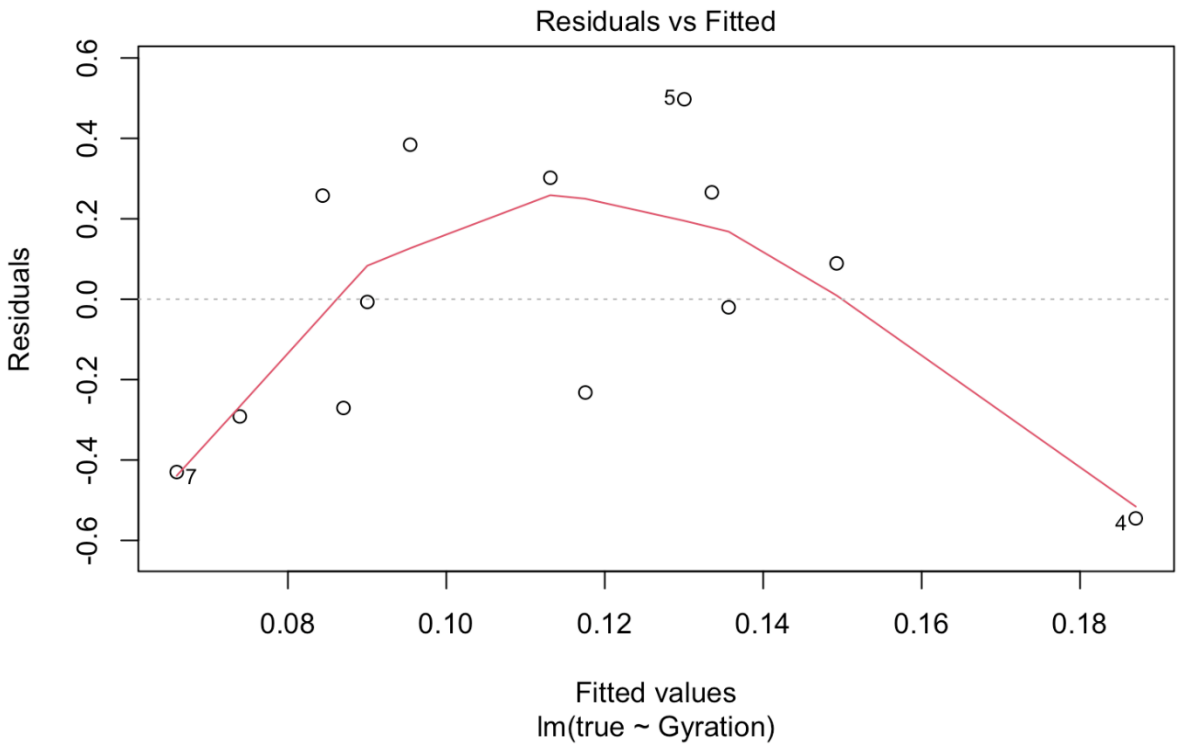

Figure 15 i.e., S9 Residual vs. fitted values.

To verify the relationship between the scar-trajectory similarity metric and the rotational tendency, we first used a linear model to measure the relationship between the two. The resulting residual vs. fitted values plot, a common diagnostic to check whether our model assumption (i.e., that the residuals have no trends and are centered around 0) are true, is shown here. The fitted values are the y values generated by evaluating our linear regression equation at the given x values (in our case, x is rotational tendency). The residuals are the actual y values (the actual scar-trajectory similarity metric) minus the predicted scar-trajectory similarity metric using the regression. When we plotted the residuals versus the fitted values for this model in this way, we observed a clear quadratic trend. Thus, this strongly suggested that a quadratic model is the most fitting to represent the relationship and that relationship was significant as shown on Figure 5 panel E of the manuscript. Furthermore, the fitness of the model, as measured by R^2, increased to 0.55 from 0.01 when we switched to quadratic from linear model, further suggesting quadratic model being an appropriate fit.

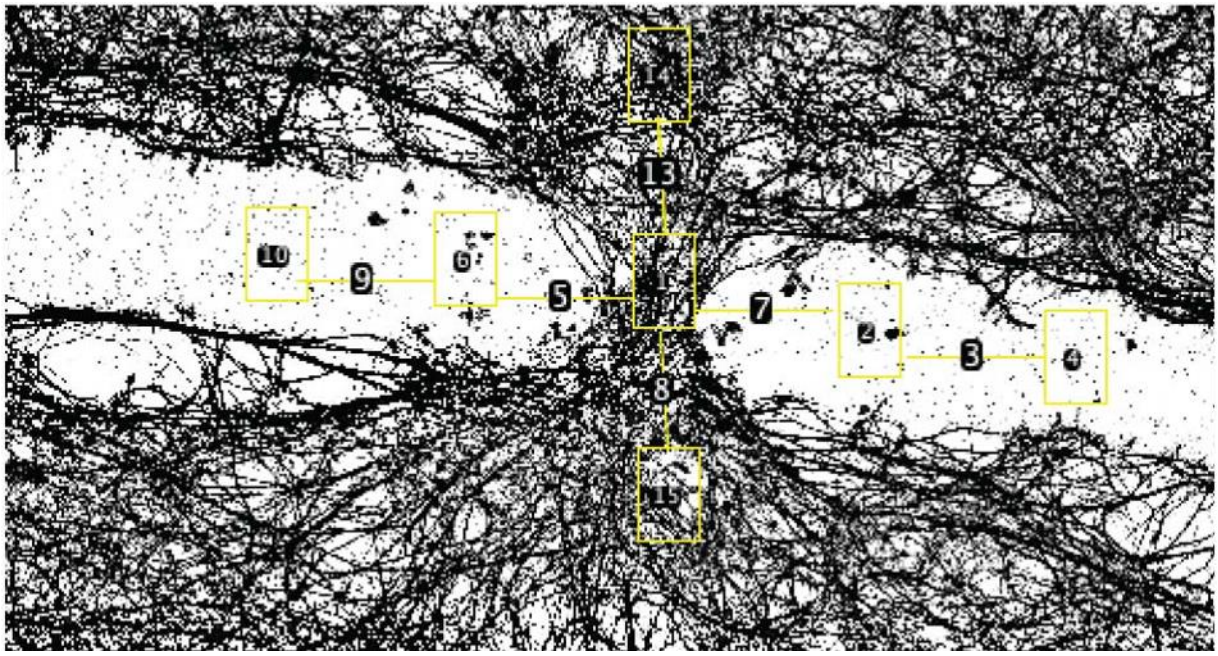

Figure 16 i.e., S10 Sample neuronal density sampling region.

Each rectangle represents an area sampled and the lines are consistently the same length, the “bridge length.”

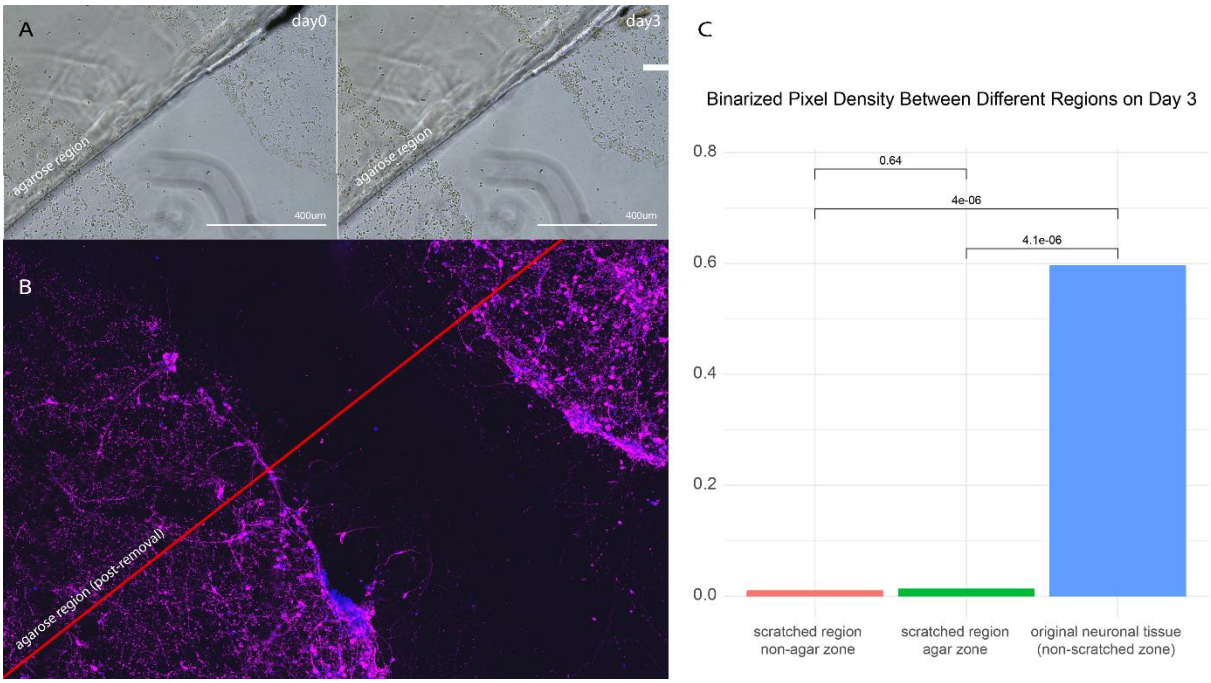

Figure 17 i.e., S11 Neuronal healing control for mechanical loading.

(A) Day 0 and 3 (i.e., day 4 upon scratching and agarose slab placement) images of a neuronal scratch with a piece of agarose slab (indicated with labels “agarose region”) placed to test for the influence of passive mechanical loading (as opposed to Anthrobots) on gap closure, which induced no difference in neuronal density between the agarose loaded and non-loaded regions as identified by (B) TuJ1 neuronal staining upon fixation on day 3 as well as (C) image analysis on agarose loaded and non-loaded zones with N=10 replicates.

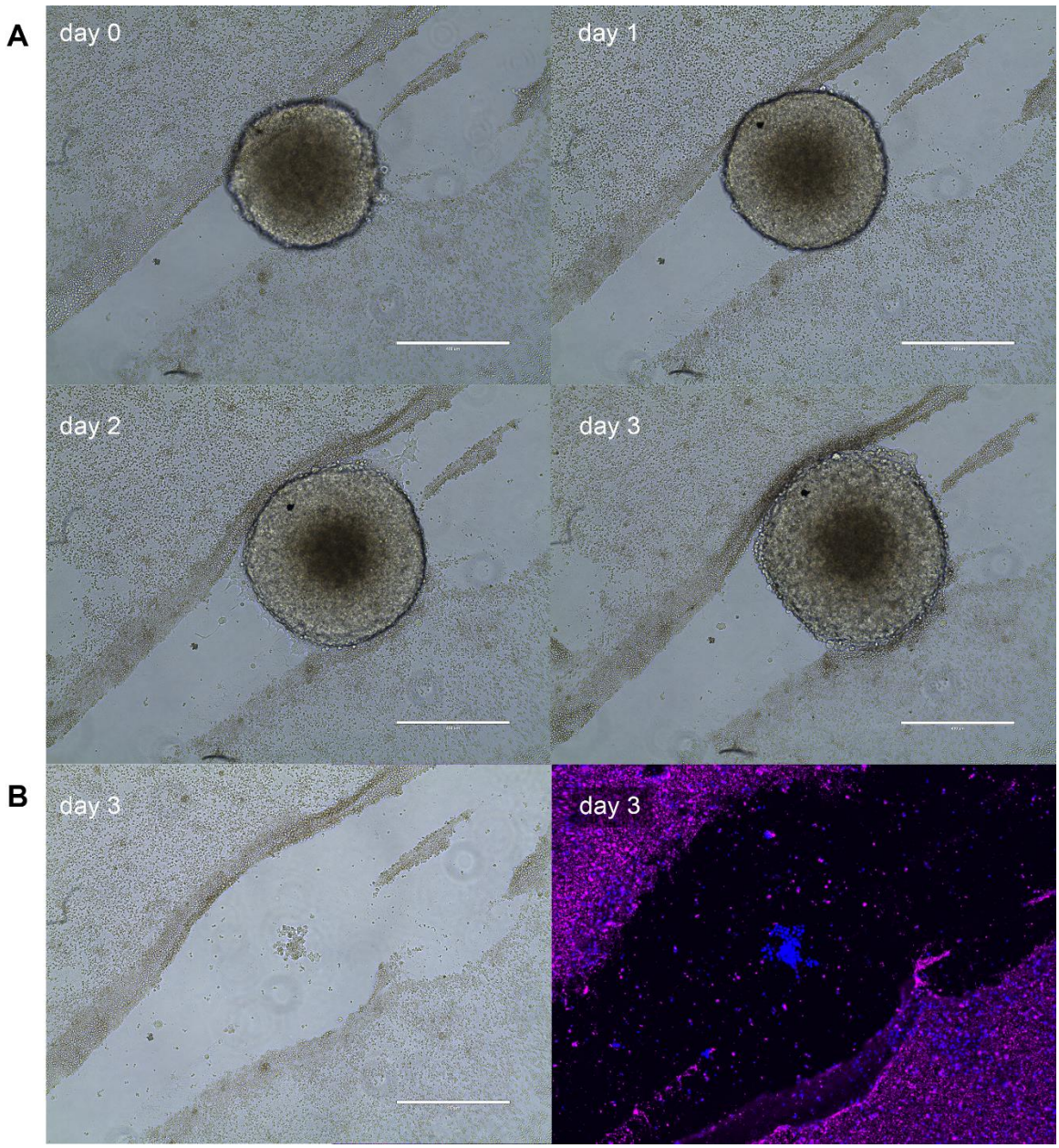

Figure 18 i.e., S12 Neuronal healing control for non-Anthrobot spheroids (e.g., made from HEK cells)

(A) Day 0 - 3 images of a neuronal scratch with a spheroid made up of HEK cells placed on top in order to test for the influence of another biological multicellular aggregate structure (as opposed to Anthrobots) on neuronal gap closure. This induced no difference in neuronal density between the HEK spheroid loaded and non-loaded regions as seen on (B) the phase contrast image of the loading site, taken upon removal of the HEK spheroid on day 3. The remaining cell cluster on the site are residual HEK cells without any neuronal make up as evidenced by the shown immunological staining performed on the tissue with Tuj1 (neuronal marker, pink) and DAPI (nuclei marker, blue) stains.

CHAPTER III

Towards a New Architecture: Exploring native anatomical tissue plasticity as an alternative approach for synthetic morphogenesis.

"The house is a machine for living in."

— Architect Le Corbusier
Towards a New Architecture, 1927

Abstract

The question of how to steer a biological system towards a target anatomy of interest lies at the very heart of the ambition of building with biology and of creating synthetic biological structures by design, which will be immensely impactful for diverse disciplines from regenerative medicine to sustainable construction. However currently there are no reliable methods for facilitating large-scale anatomical change towards a target morphology while maintaining the biological system's ability to self-construct. Therefore, the primary goal of this paper is to propose a novel methodical approach for a biological system to build itself into a prespecified synthetic target morphology. In this method the radical anatomical changes are accomplished by supplying the wild-type chassis with a set of a priori designed non-default developmental inputs to steer an

existing wild-type biological system towards the target design. As this approach relies on harnessing the emergent dynamics of biological systems, a follow-on goal of the study presented here is to additionally investigate the morphological and functional variability, and the discrete or continuous nature therein, of the resulting synthetic constructs. Finally, a discussion on the hierarchy and correlation between these anatomical and behavioral properties as they relate to the developmental choreography of the large-scale morphological reconfiguration observed in these synthetic multicellular constructs is also included. We further illustrate this novel approach to synthetic morphogenesis through the case study of Anthrobots, self-constructing, autonomously motile, synthetic multicellular structures made of human cells, with novel functions, unleashed through exploitation of functional plasticity of adult tissues without the use of genetic circuits.

Synthetic morphogenesis aims to harness hallmarks of biological construction towards generating novel anatomies by design.

Synthetic morphogenesis is an exciting sub-field of synthetic biology, focusing on developing living biological structures with novel anatomical features that are designed and programmed by humans, instead of purely driven by evolution [107-111]. However, the goal of synthetic morphogenesis is not only to create these final structures by design; but more importantly, in doing so, to harness hallmarks of biological growth, notably the process of self-construction and autonomous generation of form and function. In this way, by bringing together the goal-orientation of design and unique features of biological construction, synthetic morphogenesis could help human engineers

accomplish something that has never been possible before: building with living building blocks that can self-replicate and arrange themselves into specific target configurations with distinct material and behavioral properties.

As humans, for the last few millennia, we have gotten really good at inventing different ways to do top-down construction: from cleverly articulated steel constructions to casting cement into ingenious forms of concrete, to the good old masonry of baking bricks and stacking them on top of each other---in all instances we are the ones manually configuring the matter in a top-down manner into pre-conceived forms towards a final design. In contrast, biological structures build themselves in a bottom-up manner by replicating their constituent building blocks exponentially, perform real-time embodied computation, and heal in the face of damage. We are now at this unprecedented, exciting point in time where, for the first time in history, as engineers and designers, we might be able to import these extraordinary features of biology into the human-made structures. To do this, we need to find ways to steer biological structures towards designed ends while maintaining their unique bottom-up morphogenetic power. This way, one day we might be able to get those bricks to self-replicate and arrange themselves into a target design prescribed by the human engineer[1,106].

This requires directing a “seed” cell to build itself into a three-dimensional multicellular structure that consistently reaches (and perhaps even repairs to) an a priori designed shape and functionality (i.e., “target morphology”), either by carefully designed genetic circuits [112,113] , which has been the predominant approach so far, or an orchestration of environmental signals supplied in bulk[114]. Here we elaborate on the

latter approach through the case study of Anthrobots, a self-constructing, autonomously motile, synthetic multicellular structure made of human cells, with novel functions, as a case study in the exploitation of functional plasticity of adult tissues without the use of genetic circuits. Furthermore, as a novel aspect of the synthetic morphogenesis literature, we also discuss the behavioral dimension of these synthetic constructs.

This synthetic morphogenesis approach is in contrast (and complement) to the mainstream tissue engineering efforts for creating synthetic biological constructs, which is often garnered around shaping biological tissues in a manual, top-down manner through surgical manipulations, molding and casting, or 3D printing in order to retain an increased degree of control over the target morphology and functionality[115,116]. This approach often yields synthetic biological constructs that are hybrids between biological cells and inert chemical substances supporting them, such as gels or scaffolds or fillers (in the case of molding); but some of them can also be fully animate and not require mechanical support from inert substances as they are formed by sculpting and molding of cellular material into self-supporting structures with specific shapes[31-36,38,39,117-123]. Because this top-down form-giving approach grants engineers with greater direct control over the structures, most of these top-down shaped constructs even have functional properties, for example they can locomote either spontaneously, or with external pacing, they can respond to external stimuli, and some of them can even do useful work. Taken together, these top-down approaches, as they individually shape the final construct provide greater control over final tissue architecture and function compared to synthetic morphogenesis efforts; however, the tradeoff is that the power of

biological structures to build themselves by executing embodied morphological rules is bypassed as the final architecture is externally prescribed.

To date, most of the bottom-up, synthetic morphogenesis approaches relied on genetic circuits to drive tissues to self-organize into pre-programmed morphological states [21,124-132]. Through insertion of carefully designed genetic circuits into the constituent cells, these approaches rely on the ability of biological cells to interact based on local rules: by inserting novel rules of interaction encoded in said genetic circuits into individual cells, the multicellular system is driven into target morphologies. This approach allows versatile and robust programmability of multicellular structures while maintaining their ability to build themselves in an autonomous manner by driving self-organization towards a designed end[4,13,43,133-145]. However, this approach comes with its own challenges and limitations. Notably, the complexity of target morphologies (and functionalities) that can be created with this approach have been limited due to technical restrictions stemming from a cap on the number of transcriptional units that may be encoded in a circuit size-limiting delivery methods, and chassis-to-chassis variability [146-151].

Here, we propose an alternative but complementary approach that, instead of inserting exogenous genetic material to implement novel forms, relies on exploring alternative, existing avenues in the wild type organism's genome that may lead us to the target morphology. In the circuit-based approach, the entire emphasis is on the circuit itself and the idea (at least the aspiration) is that the chassis selection does not matter, as the circuit is expected to work as a global piece of code, isolated from the emergent affairs of its biological housing. In our approach, contrary to that, we put the entire

emphasis on the chassis and its unexplored capacity for novel form and function of interest. In other words, we hypothesize that wild-type tissues have latent morphogenetic developmental paths that have the potential to yield novel synthetic features, which may be explored by providing the wild-type chassis with non-default developmental inputs. This new approach is informed by the hypothesis that multicellular systems have latent developmental paths that are driven by an alternative set of morphogenetic rules, which are different that those called upon during the default development of the species-default morphology. We hypothesize that these latent rules may be triggered into action by providing the system with non-default inputs, thereby systematically harnessing native tissue plasticity to steer a biological system into target morphologies. In this way, we still enable biological material to retain its autopoietic ability to self-construct, while yielding complex final morphologies without being held back by the rate limiting aspects of genetic circuit-based synthetic morphogenesis. To illustrate this point, we discuss Anthrobots as an example.

Exploiting anatomical tissue plasticity as an alternative approach for synthetic morphogenesis.

It has been known that same genome can give rise to different anatomies [152-157], as the developmental process unfolds as a series of morphogenetic functions [158], to which genes are a critical input but are far from the only one[159,160] : environment is an equally powerful determinant of the set and sequence of morphogenetic events unfolding in a developmental process, evidenced by same cells grown in different conditions giving rise to vastly different anatomies. The field of morphogenetic plasticity

thus has been concerned with mapping the possible anatomical outcomes that develop out of a specific wild type (WT) chassis, and the non-default environmental input(s) driving these outcomes. However, the inverse problem has not been investigated: how to arrive at a specific anatomy by starting from which WT chassis supplied with what non-default environmental input(s)? Thus, the primary goal of this paper is to discuss a model system in which the key question of whether the native plasticity of an existing tissue system with a wild-type genome can be steered towards a target morphology is answered. This goal relies on the hypothesis that specific morphogenetic outcomes may be achieved by systematically steering a biological system towards alternate developmental paths.

Creating the morphospatial landscape is the first step for facilitating radical morphological change towards target anatomy:

In order to identify what specific alternative developmental path to evoke, we start by constructing a “morphospatial landscape” (Figure 19), on which starting point is a default wild-type anatomy (see step1 below), from which alternative developmental paths branch out (step 2) wherein each path ultimately lead to the target synthetic morphology in different ways, all the while keeping the genome wild type. The specific aim of a morphospatial landscape is to map the hypothetical and testable avenues for steering an existing biological system (with a well-characterized stable developmental path) towards an a priori defined target morphology by only tuning its environmental variables while keeping the genome wild type (avoiding direct genetic editing). In other words, the goal of creating a morphospatial landscape is to map potential paths that

may facilitate radical morphological change towards the target anatomy that may be well within this WT biological system's unexplored morphospace[161-165].

Next, we propose a stepwise summary of how to map a morphospatial landscape to identify the path of interest, followed by details on preliminary experiments performed on the path of interest selected per the morphospatial landscape in this specific project.

<u>There are four major steps for building a morphospatial landscape and selecting the path of interest towards target anatomy:</u>

Step 1: Identify an existing, evolved "default" morphology that is closest in material and functional properties to that of the target system.

Step 2: Mark the existing deviations from this default morphology as alternative developmental paths already explored.

Step 3: Map alternative developmental paths within the chassis that may conceivably lead to the radical target morphology, and identify the morphogenetic functions, system-level inputs, and trade-offs along each path. In other words, map out the morphospatial landscape (see Figure 19 grey shaded area, labeled "morphospatial landscape"), by identifying i) different paths, ii) and for each path:

a) What morphogenetic functions need to unfold within the chassis [along each potential path] to drive its morphological state to the target morphology (e.g., cilia coated spheroid) from a known starting position (e.g., individual cells that are human airway progenitors as shown in Figure 19 point B; or an already

differentiated version of these cells in 2D or 3D, as shown in Figure 19 points D and C, respectively).

b) What external inputs are needed for identified morphogenetic function(s) to unfold within the chassis along a given path, while keeping the genome wild type (so, no direct genomic editing inputs are allowed).
c) What tradeoffs exist along each developmental path in terms of fabrication and growth conditions.

Step 4: Evaluate different paths and identify the path of interest (per what territorial tradeoffs are important for the target design, given all paths conceivably result in the same target morphology), and accordingly plan the experimental strategy to trigger the necessary morphogenetic functions [needed along that path] in the chassis.

Thus, a critical first step in coming up with a morphological hypothesis to steer a WT anatomy to a designed end as is to first map the morphospatial landscape on which reasonably conceivable (but not necessarily all possible) alternative developmental paths as well as necessary morphogenetic functions and territorial tradeoffs are laid out.

<u>Example application of the morphospatial landscape towards a target anatomical design:</u>

To investigate this approach, here we explore a specific target morphology, a novel, multicellular, fully biological, self-constructing, motile spheroids, by providing an existing biological system, human lung epithelium, non-default inputs and investigate whether this target morphology may be accessed as a latent developmental path. As a result, we expected to observe synthetic multicellular constructs with the target

morphology and function to self-construct in vitro, via a fully scalable method that requires no external form-giving machinery, manual sculpting, or embryonic tissues, and will move via cilia-driven propulsion. This will mean that by confronting evolved systems with novel contexts, we can learn about the degree of plasticity that cells and control pathways can exhibit toward new anatomical and functional endpoints, as well as develop protocols to alter default outcomes.

Therefore, in order to determine whether the native morphogenetic plasticity of biological cells can be harnessed to reach specific anatomical outcomes by design, given our design goals here, we considered different human ciliated tissues (e.g. airway epithelia, brain ventricles, oviductal epithelia), and decided on the normal human bronchial epithelial (progenitor) cells, NHBEs, as our starting WT chassis to explore the alternative developmental path towards the target anatomy of cilia-covered spheroids. In other words, because the target architecture is motile spheroids covered by cilia in the case of this project, we embark on our exploration of latent paths towards this target architecture by branching from the default developmental pathway of human airway epithelium (Figure 19, “default evolved morphology”), as this native system is known to develop heavily ciliated tissues. A biological system that is close in material properties to the target system serves as the optimum chassis for exploration as such system would have the highest likelihood of harboring the latent paths towards the target tissue architecture, providing a meaningful landscape for an efficient search for potential paths towards the target morphological and functional characteristics.

Having formed the hypothesis that human bronchial epithelial cells (NHBEs) can be used as a wild-type chassis in which the target synthetic morphology of outward

ciliated motile spheroids may be unlocked, we next identified the set of non-default morphogenetic events that need to unfold to guide this WT chassis towards the target morphology (proliferation via monoclonal self-construction, differentiation, eversion), as well as the set of non-default environmental inputs accordingly supplied to the system during its development to facilitate these morphogenetic functions.

While all paths on the morphospatial landscape start from the same default wild-type chassis (human airway epithelium in this case), each path is then forged towards the target morphology by a different set and sequence of “morphogenetic functions” (step 3a), each triggered by a specific environmental input along the path (step 3b). In this framework, each morphogenetic function has two major inputs: i) starting condition of the chassis at the beginning of the stage where the function is expected to unfold, and ii) the environmental input needed to facilitate this unfolding.

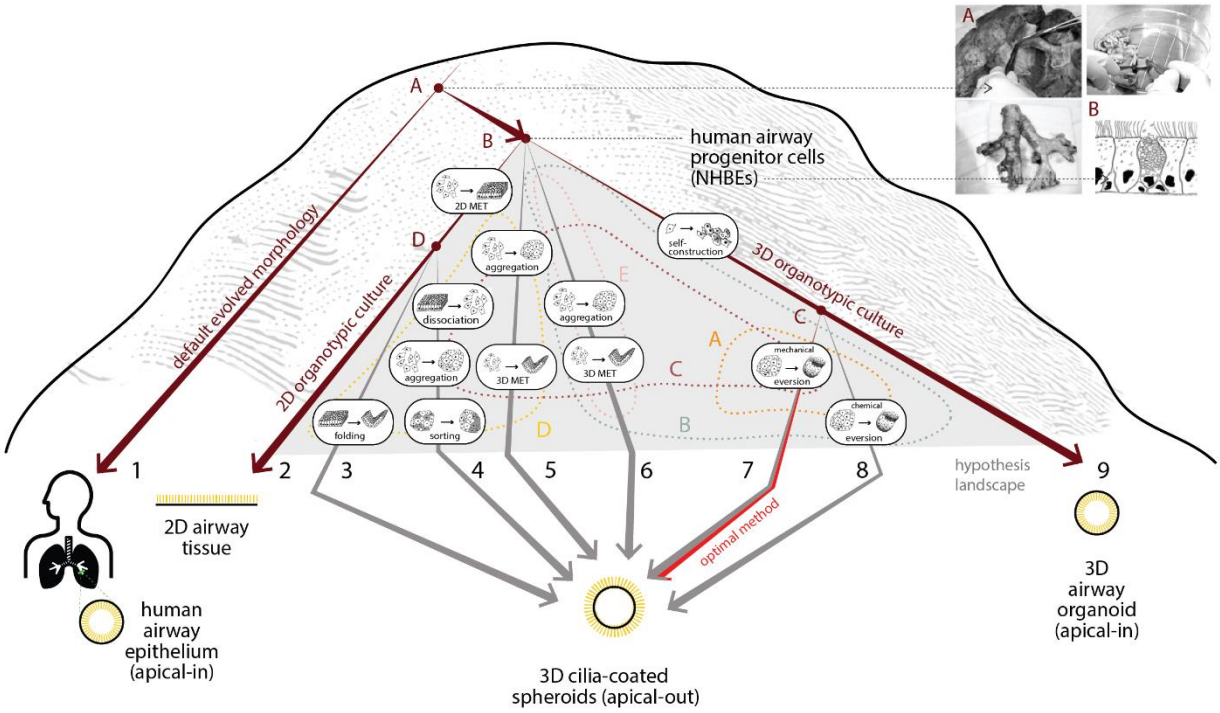

Figure 19 Morphospatial landscape for the target morphology of cilia-coated spheroids to grow from wild-type human bronchial epithelial cells.

The morphospatial landscape shows the human airway epithelium as the evolved default morphology, the wild-type tissue to conduct the exploration. Paths 2 and 9 show existing deviations from this default morphology as alternative developmental paths already explored. Paths 3 through 8 show alternative hypothetical paths that may lead the wild-type chassis (NHBEs) to the target morphology. The path explored in this proposal is #7, outlined in red. Along each path, necessary morphogenetic functions, as well as the territories each path crosses are shown.

Furthermore, even though all paths on the morphospatial landscape initially branch off from the same point and eventually result in the same target morphology, and even sometimes require similar inputs and morphogenetic functions, what is strictly unique about each path is the “territory” it passes through on the landscape (Figure 19, see dashed lines demarcating territorial boundaries). Each demarcated territory on the morphospatial landscape requires different growth and fabrication conditions (step 3c).

Based on the territory a given path cuts across, it acquires a unique set of growth and fabrication properties, invertedly trading off one property for another. For example, path 7 sacrifice uniformity of spheroid shape for the sake of retaining the ability to self-construct, while conversely paths 5 and 6 sacrifice self-construction for the sake of uniformity of spheroid shape; path 5 then further sacrifices scalability for the sake of control over spheroid size[166], and path 6 vice-versa[167].

Depending on the final purpose, the growth and fabrication properties of a given path can be as important as its ability to yield the target morphology. Thus, a comprehensive mapping of the morphospatial landscape in this way is a critical first step for identifying the optimum path to steer a WT anatomy to a designed end, as through this landscape the scientist could identify the required morphogenetic functions need to unfold in the chassis to drive it through each path, specific inputs needed to trigger these functions in the context of that particular path, as well as the territorial trade-offs along each path. At the end, with this complete set of information, a path that not only conceivably yields the target morphology and functionality, but also that satisfies the target growth and fabrication properties can be selected for further investigation and experimentation in the laboratory (step 4). For example, because the target architecture in this proposal requires self-construction, only paths 7 and 8 (i.e., ones branching off C) are suitable for the purposes of this project. It is exclusively in those two developmental paths that the formation of 3D multicellular structure is the result of a self-construction process from a single precursor cell via monoclonal expansion and proliferation. Even though other hypothetical paths (3-6) also result in the cilia-coated multicellular spheroid morphology, they require either surgical

manipulation (e.g., path 3) or molding-based cell aggregation (e.g., paths 4-6), hence they would not be appropriate to follow. And among paths 7 and 8, because mechanical eversion is known to happen faster than chemically induced eversion[168], path 7 is selected.

In terms of the exploration of this landscape, it has been proven in the laboratory that paths 3[49], 5[166], 6[167], 7[114], and 8[48] all can lead to the target anatomy. Efforts along path 4 has not yet yielded the target anatomy [see Figure 20], but since it is known that adjusting the mixing population ratios in the morphogenetic function of cell sorting can lead to vastly different morphological outcomes[169], we hypothesize that future efforts on adjusting the ciliated vs non-ciliated cells could eminently yield the target anatomy.

Specific wetlab experiments for exploring the anatomical path #7:

With the goal of studying wild-type systems in the laboratory, scientists have devised various ways to culture native biological systems in-vitro as organotypic cultures that recapitulate native tissue morphology [170]. Although the goal in these efforts is to recreate the wild-type morphology and function as closely as possible, because these in-vitro culture systems are created within the confines of the laboratory environment and optimized to be permissive to manipulation and experimentation, these tissue systems inadvertently diverge in morphology from their native counterparts. In this way, in-vitro organotypic cultures constitute the first uncovered alternative developmental paths to a given native tissue (Figure 19, branching point A) as in these cultures' cells retain their wild-type genomes yet give rise to morphologies that are

sufficiently different from their native tissue architectures that are shaped by evolution in the course of millions of years.

For example, two major protocols for culturing human bronchial epithelial cells in-vitro, the 2D Air-Liquid Interface[171] and the 3D Matrix-embedded methods[172-175], yield completely different morphologies from one another (and from the native human airways), while each sufficiently recapitulating the epithelial architecture in different ways. Although neither of these methods yield our specific target morphology (of an outward-ciliated spheroid), these developmental pathways established by these in-vitro culture methods constitute the first uncovered developmental paths alternative to the native human airways as in these in-vitro developmental pathways normal human bronchial epithelial cells retained their wild-type genomes yet gave rise to morphologies (flat ciliated epithelium in the 2D case, and a sphere with a cilia-lined lumen in the 3D case) that are sufficiently different from their native tissue architectures (cilia-lined tubular branches).

Uncovered latent paths like these (even if their goal is to recapitulate the native tissue architecture as closely as possible, as opposed to inducing a radical morphological change) provide additional launching pads to branch off from to further explore the chassis' native tissue plasticity and latent paths lay therein that may conceivably lead to the target architecture.

Accordingly, after identifying the alternate path #7 as detailed above that would satisfy not only the target requirements, but also the fabrication conditions, next we differentiated primary normal human lung epithelium cells into 3D airway organoids w/ ciliated lumen, as this constitutes a meaningful and reliable biological system to search

for the latent developmental path into the cilia-out spheroids. In order to facilitate this alternate development, providing the default developmental system with non-default environmental inputs (such as tuning substrate properties) may be necessary and sufficient. As it has been previously established in the enteroids literature that changing the high-viscosity matrix environment to a low-viscosity one causes enteroids to polarity switch from apical-in to apical-out [176], we hypothesized that as a next step, re-culturing these cilia-in airway organoids in a low-adhesive environment may enable them to similarly polarity switching, enabling the morphogenetic function of mechanical eversion to unfold and thereby pushing the biological system down an alternate developmental path towards the target morphology. This change in developmental path may enable the spheroids to become motile, fulfilling the original target morphological and functional design specifications.

In order to unlock the target morphology of outward ciliated spheroids starting from human bronchial epithelial cells (NHBEs), we first differentiated these wild-type progenitor cells isolated from the human airway epithelium as embedded in extra-cellular matrix per a previously established protocol into three-dimensional multicellular spheroids with cilia-lined lumen, featuring two morphogenetic functions: proliferation via monoclonal self-construction, and differentiation. Following these two morphogenetic functions, because the target morphology is a cilia-coated spheroid, we next facilitated a third morphogenetic function (eversion) by switching the substrate properties from extra-cellular matrix to liquid medium as it has previously been shown in the literature that ECM protein removal enables three-dimensional epithelial polarity switch. Thereby we pushed the wild-type chassis (NHBEs isolated from human airways) down a previously

unexplored latent developmental path (alternate to their original developmental path to human airway epithelium) into the novel anatomy of cilia-coated spheroids, the target morphology. This novel path is forged by the morphogenetic functions of proliferation via monoclonal self-construction, differentiation, and finally eversion, which resulted in cilia becoming exposed on the spheroid surface, hence enabling spheroids to become motile, fulfilling the original target morphological and functional design specifications, all the while keeping the genome wild type.

Synthetic constructs may exhibit emergent morphological and behavioral features beyond the target anatomy and functionality.

The goal of the selected alternate developmental path is to yield the target anatomy and behavior, a cilia-coated motile spheroid. However, considering the emergent dynamics of biological systems and the potential element of surprise, it is not known a priori whether the resulting anatomies and behaviors will be identical every single time, forming uniform pools, or whether they will constitute slight changes, forming continuous distributions, or whether they will fall into distinct character bins, forming specific anatomical and behavioral traits. Thus, to understand developmental features of the resulting synthetic multicellular constructs, it is necessary to characterize the anatomical and behavioral spaces by sampling a large population of these resulting constructs and quantifying the range of morphological and functional properties. Such investigation would not only enable the designer to identify whether the anatomical and behavioral spaces are uniform, or display a continuous gaussian along certain features, or consist of specific combinations of these features, hence forming discrete and unique

characters; but it would also help identify whether there is a hierarchy between these features in terms of their impact in guiding the synthetic developmental process towards specific sub-types. Moreover, it might even be possible to discover an emergent relationship between the range of resulting anatomies and behaviors observed in the synthetic constructs. Accordingly, in order to characterize the range of resulting morphologies and behaviors observed in Anthrobots, we collected anatomical (3-dimensional structural data via ICC/IF and confocal microscopy) and behavioral (2-dimensional motility data via timelapse microscopy and agent tracking) data from several hundred Anthrobots. Using this data, we conducted statistical analyses on body shape and cilia distribution, as well as on functional patterns of motility trajectories and mapped the morphological and behavioral character landscape of Anthrobots.

Emergent morphologies beyond the target anatomy:

First, to investigate whether the range of resulting morphologies is uniform, continuous, or composed of discrete categories, and whether there is a hierarchy between these potential morphological characters, we collected 3-dimensional structural data from several hundred of these synthetic multicellular constructs through ICC/IF and confocal microscopy, focusing on shape and cilia distribution pattern properties. We then binarized these morphological features to extract quantitative information on cilia and body boundaries. We then plotted this information along eight different morphological characterization indices that we defined, each quantifying a different aspect of these synthetic multicellular constructs' shape and cilia patterns.

The shape-related morphological characterization metrics included indices like the ratio between the longest and shortest distance within a spheroid (i.e., “aspect”), longest distance within a spheroid (i.e., “max radius”), how invaginating or protruding the spheroid surface is (i.e., "shape smoothness"); and the cilia-related metrics included indices like the total area covered by cilia signal on a spheroid surface ("cilia points"), cilia signal per unit area on a spheroid surface ("cilia points/area"), proximity of current cilia point distribution to a complete random uniform distribution ("cilia distribution homogeneity"), how clustered the cilia are on a spheroid surface ("polarity"), and how many free-floating cilia points there are that are not a part of a cluster ("noise points").

Once we quantified each Anthrobot in our pool by these morphological indices focusing on shape and cilia distribution, we performed a Principal Component Analysis (PCA) on the resulting 8-dimensional data cloud (each dimension corresponding to one of the indices explained above) to identify the maximum variability plane (defined by the two axes along which the variation on the data is maximal). Next, on this PCA-identified plane, we ran a cross-entropy clustering algorithm to identify the potential statistically distinct clusters. We indeed observed three distinct clusters and formally described each cluster by using the morphological indices, yielding a complete quantitative characterization of different “morphotypes.”

Emergence of these three statistically distinct clusters means that not only the path 7 led to the formation of the synthetic multicellular constructs with the target anatomy and behavior (i.e., multiciliate spheroids), but also that the path organically continued beyond this point, culminating in three different flavors of the target morphology, each featuring a distinct morphological type (morphotype). Had we not

observed the emergence of clusters (meaning had the data points roughly equally distributed on the PCA plane), then we would have concluded that the resulting morphology has some variation but doesn't organize around specific characters; forms a noisy continuum. Alternatively had all data points aggregated on a specific coordinate (i.e., single cluster) then we would have concluded that the resulting constructs are uniform with very little variation and thus path 7 terminates in the target morphology without further downstream branching.

Once we identified the morphotypes in this way and uncovered a downstream branching phenomenon, next we wanted to map this additional emergent landscape, which is in essence analogous to the Waddington Landscape. To this end, we analyzed the hierarchical relationship between different morphological indices in distinguishing morphotypes from one another (based on the PCA contribution rankings of each index). This hierarchical analysis enabled us to uncover the developmental decision tree (i.e., the Waddington Landscape) of these synthetic multicellular constructs, wherein hierarchical index rankings correspond to the branching points of the landscape: the highest-scoring index forms the first branching point, i.e., first "decision" point, the second highest-scoring index forms the second branching point, i.e., the next decision point, and so on. As a result of this hierarchical clustering analysis had we observed that all indices contribute equally, then we would have concluded that decision points during the developmental path is random. However, in our case we observed "size" and "shape regularity" indices as features that are the largest determinants of morphotypical clustering (i.e., highest-ranking indices), followed by cilia localization pattern (e.g., polarized vs uniformly distributed). This way, we have been able to map out the

sequential logic of decision-points in the emergent morphospace, and uncovered how Anthrobots, as synthetic multicellular constructs, move through the developmental landscape, and what check points of morphological possibility do they negotiate in reaching their final architecture.

Emergent behaviors beyond the target functionality:

After mapping the emergent morphological landscape as described above, we extended a similar analysis to the emergent behavioral landscape. Accordingly, to investigate whether the range of resulting behavioral patterns is uniform, continuous, or composed of discrete categories; and whether they correlate with the potential morphological categories established above, we collected 2-dimensional movement data, through multi-hour timelapse videos of several hundred randomly selected Anthrobots, in groups of 4 or 5, and extracted their movement trajectory coordinates. We first split up these 5 hour-long trajectories into 30 second periods to classify behavior with a higher degree of granularity and in an aggregate manner. Then, to identify patterns within a potentially unlimited set of possible movements, we evaluated these periods by how straight and/or circular the trajectories are, as all possible movement patterns can be explained together by some combination of these two properties.

To this end, we used two main trajectory characterization metrics: straightness and gyration indices and thus plotted all viable trajectorial periods along these two indices. We then ran a cross-entropy unsupervised clustering algorithm on this two-dimensional plot to identify statistically distinct clusters, if any. Similar to the analysis we

performed for the morphotype mapping, if we observed clusters in this landscape, it would mean there is emergent character trait formation on the behavioral front as well. As a result, we indeed observed four distinct clusters and formally described each cluster by using the motility indices, as well as yielding a complete quantitative characterization of the emergent behavioral types.

Furthermore, because transient behavior changes may occur -unlike morphotypes- next we investigated the transition probabilities between each pair of behavior types using a Markov chain. This analysis on state transitions between different movement types helped us estimate the stability of each trajectory and revealed the degree of commitment to a given behavior (persistence), providing an ethogram of target morphology behavior. In conclusion we identified circular, straight, and curvilinear types as movement types with high “consistency,” meaning low rates of inter-type conversion, suggesting that the synthetic constructs can self-organize into discrete and stable movement types, each having a distinct motility fingerprint.

Once we complete the behavioral characterization in this way and the morphological characterization as explained in the previous section, having identified stable attractor states in both spaces, we next investigated a potential correlation between these two sets of characters. To do this, we incorporated the movement type analysis described here into the morphological PCA analysis explained in the previous section and juxtaposed the two lenses to investigate the potential correlation. To make this analysis possible, during the initial sample collection process for the morphotype analysis, in addition to recording the binary motility data for all data points (i.e., “motile” vs “non-motile”), we had further sampled the “motile” population by collecting several

dozen data points within this category and recording the specific motility pattern. These subjects were randomly selected from the two most orthogonal movement types, in approximately equal proportions, to cover the widest range of behavioral possibilities. Upon identifying these specific data points within the morphotype PCA cloud assigning them this additional layer of information on movement type, we then computed the statistical significance of these overlaps using the Fisher test. As a result, we uncovered a significant correlation between certain morphotypes and movement types, suggesting a surprising relationship between emergent morphology and phenotypic behavior. While more work needs to be done to establish a causal relationship between these morphotypes and the movement types, our analyses showed significant correlation between the non-displacing (wiggler or non-mover) movement type and morphotype 1, linear movement type and morphotype 2, and finally circular movement type and morphotype 3.

Conclusion

The field of morphogenetic plasticity[177-179] has long been concerned with the question: what are the ways in which a wild-type genome can branch into different morphologies? The purpose of the research program detailed in this paper is to mirror that question: What are all the ways in which a wild-type genome can be steered into the same end—a designed one? These questions are not competitive, but complementary and taken together they will not only help us better understand the

relationship between genome and anatomy but will also enable generation of specific target anatomies without needing to directly interfere with the genome.

As a case study for this approach, here we review our investigations on whether the unique and spontaneous 3-D multicellular morphogenesis of adult airway cells into novel motile multicellular constructs is possible; the final morphology and function of these synthetic constructs display a degree of variability and exhibit discrete characters with easily recognizable primary features; and these morphological and functional characters correlate with one another. We hypothesized that even if the wild type tissue of origin may display anatomical uniformity, the resulting synthetic constructs may exhibit variability along major anatomical traits like body size and shape, as well as cilia amount and distribution pattern.

In order to test this hypothesis, we first collected data from several hundred synthetic multicellular constructs and measured their different anatomical features along several morphological description indices. We then use a Principal Component Analysis to identify which indices are necessary for quantitatively describing the key differentiating elements of their anatomy. We cluster-analyzed this dataset to characterize the distribution profile as discrete and uncovered the hierarchy between these different anatomical features in determining morphological outcomes, analogous to stem cell lineage decisions.

Next, similar to the morphological case, we further hypothesized that even if the wild type tissue of origin may not display the functional property (of motility), the resulting synthetic constructs may exhibit various different behaviors and motility

patterns. Furthermore, the morphological variants and behavioral variants may have a phenotypic correlation.

In order to test this hypothesis, we similarly collected movement trajectory data from several hundred synthetic multicellular constructs and characterized their motility features along two major movement indices (gyration and straightness indices). We then cluster-analyzed this dataset and discovered the behavioral distribution also consisting of discrete features. This provided us a framework to investigate whether there is a correlation between the distribution of functional properties vs the previously investigated morphological properties, and we discovered a significant correlation between these emergent morphologies and functionalities.

This morphological and behavioral analysis enabled the mapping of the anatomical decision points along this alternate developmental path we evoked, in addition to providing a better understanding of the latent morphological and functional abilities of human airway epithelium. Furthermore, such analysis will also serve as an essential background characterization of these synthetic constructs, from which future efforts to reprogram form and function will flow, and during this process, genetic circuits may still be used on an as-needed basis to enhance the established synthetic morphology. In this way, the approach that gave rise to Anthrobots is complementary to the traditional synthetic morphogenesis approach that has been focused on expanding cellular abilities primarily via genetic circuit-based engineering. Systemic exploration of morphogenetic plasticity taken together with the genetic circuits has the potential to improve the reach of synthetic morphogenesis into larger length scales.

Supplemental Figures

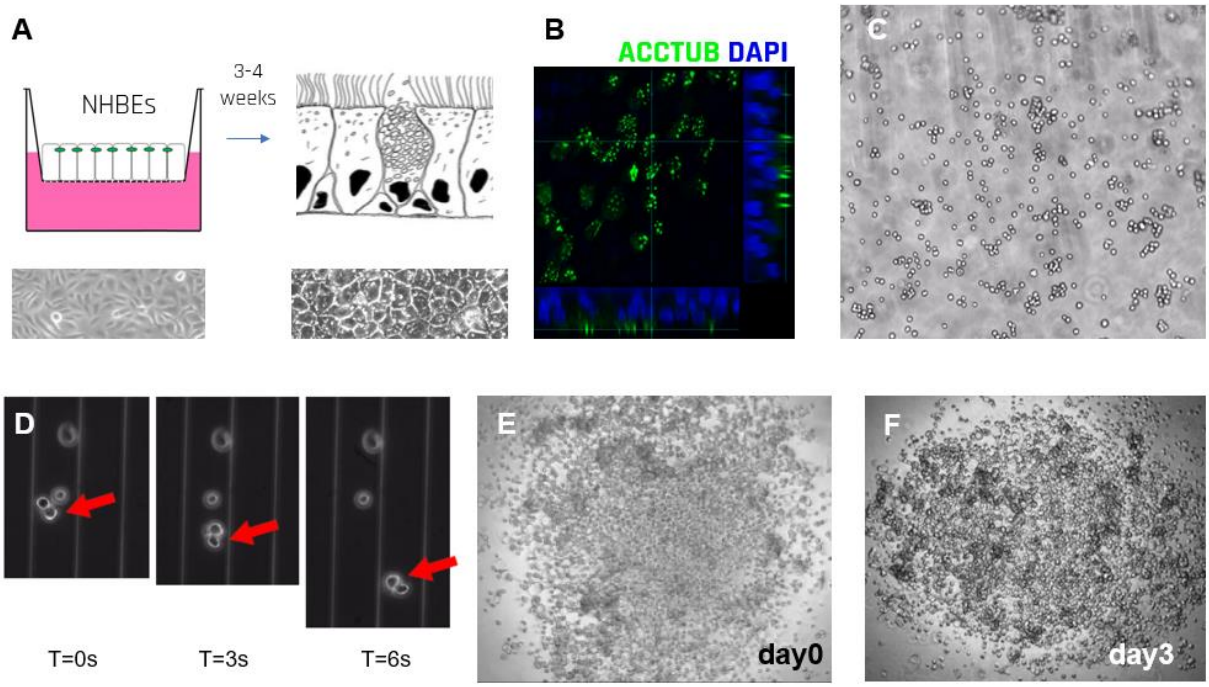

Figure 20 NHBE cells do not form cilia-coated spheroids when mixed at their native ciliated vs non-ciliated cell ratios.

Experiments showed that path 4 of the morphospatial landscape introduced in Figure 19 did not yield cilia-coated spheroids when disassociated cells were mixed together. (A) 2D differentiation of NHBE cells into ciliated epithelium was accomplished via ALI culture as evidenced by (B) an immunological assay showing the presence of cilia on the apical surface of the 2D tissue. Top view accompanied by two cross-sectional views to the bottom and to the right of the micrograph. (C) This ciliated epithelium was then dissociated into individual cells and (D) the ciliary cells motility was confirmed. (E) The dissolved cells containing ciliated and non-ciliated cells were mixed together at the native ratio and (F) formation of a self-aggregating spheroid was not observed upon a typical aggregation period in this culture method (3 days).

CHAPTER IV

Conclusion

“Study nature, love nature, stay close to nature. It will never fail you.”

— Architect Frank Lloyd Wright, 1907

How can an army of termites build “cathedrals” that are ten million times larger, when normalized to human scale, than the Notre Dame, Sagrada Familia, and Hagia Sophia stacked on top of each other? How does a sack of cells know which direction is left or right, so as to build the heart, liver, or spleen in the correct place? And how do these builders replicate and organize themselves using embodied blueprints, namely two meters-long DNA strands tucked into ten microns-wide nuclei? I remember contemplating these questions back in architecture school and finding myself in utter fascination with biological structures’ unique ability for self-construction, carbon-negative manufacturing, self-replication of building components, and ability to regenerate after damage.

As I began my biological training to understand some of these questions, I came to learn that the development, maintenance, and regeneration of form and function in living biological architectures is computed real-time by an embodied morphogenetic code. Morphogenetic code encompasses the set-in stone genetic code as well as the

additional epigenetic layers that can dynamically change based on environmental input. This corporeal computation grants biological structures the unique ability to build themselves ground up from an initial building block, a single biological cell. A prolific self-construction process unfolds as this initial build block begins to self-replicate and propagate the code to its progeny, giving rise to an exponentially growing army of builders, each able to access the same construction manual encoded within. As these biological cells collectively execute the embodied morphogenetic instructions and build themselves into large-scale tissues, this process of morphogenesis results in a final living architecture that is not only able to self-construct in this way, but it can also maintain that shape by regenerating in the face of damage. It can manufacture a wide array of biomaterials from collagen fibers able compete with steel in their tensile strength, to muscle tissues that can function as powerful biological motors. Beyond these astonishing structural and material features, biological architectures can also display a diverse set of functionalities from locomotion to sensing and actuation. Some biological structures even demonstrate complex intelligence beyond the basic impulse-response reaction. Finally, biological architectures display all these astounding functions without leaving a carbon footprint—in fact most biological architectures sequester carbon from the atmosphere.

These awe-inspiring features were far-fetched for even the state-of-the-art fabrication abilities of contemporary architectural fabrication capabilities. However, I believe this is about to change. As we get better at reading and editing the morphogenetic code, we will start being able to conceive of nature as a robust design medium. This new design frontier will enable us to develop programmable living

structures capable of autonomously assembling into predefined architectures. Now, as an architect and synthetic biologist, my central passion is to forge this new frontier further and continue developing synthetic biological structures that can predictably build themselves into target morphologies by design. This Dissertation is a step towards this vision.

Mastering top-down control of nature's bottom-up morphogenetic power in this way will be a game-changing advance because gaining control over both form and function of biological tissues remains a critical barrier to innovation in many fields including architecture, materials science, soft robotics, regenerative medicine, cancer research, and even space exploration. Efficiently programming biological cells to self-organize into target architectures will enable us to overcome the challenge of building in extreme environments, such as outer space, where transportation of traditional construction material and machinery is extremely difficult or impossible. It will also allow us to grow custom organs for transplantation or drug testing, as well as to make early cancer diagnosis possible by having cancerous somatic cells self-organize into simple shapes in-vivo (e.g., platonic solids), enabling their identification with a non-invasive imaging device. I believe that synthetic morphogenesis has the potential to give us an unparalleled opportunity to tackle some of humanity's most challenging problems from creating sustainable construction methods to novel medical approaches, and even leaps in space exploration. Thus, in my PhD, and graduate research in general, I focused on morphogenetic engineering of biological systems and developed the first example of a self-constructing living architecture by design.

References

1 Gumuskaya, G. *Form From Within: Scaling Up Self-Constructing Biological Architectures through a Novel Application of Synthetic Morphogenesis*, Massachusetts Institute of Technology, (2018).

2 Pezzulo, G. & Levin, M. Re-membering the body: applications of computational neuroscience to the top-down control of regeneration of limbs and other complex organs. *Integr Biol (Camb)* **7**, 1487-1517 (2015). https://doi.org:10.1039/c5ib00221d

3 Kamm, R. D. & Bashir, R. Creating living cellular machines. *Ann Biomed Eng* **42**, 445-459 (2014). https://doi.org:10.1007/s10439-013-0902-7

4 Kamm, R. D. *et al.* Perspective: The promise of multi-cellular engineered living systems. *APL Bioengineering* **2**, 040901 (2018). https://doi.org:10.1063/1.5038337

5 Ebrahimkhani, M. R. & Levin, M. Synthetic living machines: A new window on life. *iScience* **24**, 102505 (2021). https://doi.org:10.1016/j.isci.2021.102505

6 Doursat, R. & Sánchez, C. Growing Fine-Grained Multicellular Robots. *Soft Robot.* **1**, 110–121 (2014).

7 Doursat, R., Sayama, H. & Michel, O. A review of morphogenetic engineering. *Nat. Comput.* **12**, 517–535 (2013).

8 Andrianantoandro, E., Basu, S., Karig, D. K. & Weiss, R. Synthetic biology: new engineering rules for an emerging discipline. *Mol Syst Biol* **2**, 2006 0028 (2006). https://doi.org:10.1038/msb4100073

9 Teague, B. P., Guye, P. & Weiss, R. Synthetic Morphogenesis. *Cold Spring Harb Perspect Biol* **8**, a023929 (2016). https://doi.org:10.1101/cshperspect.a023929

10 Davies, J. A. Synthetic morphology: prospects for engineered, self-constructing anatomies. *J Anat* **212**, 707-719 (2008). https://doi.org:10.1111/j.1469-7580.2008.00896.x

11 Santorelli, M., Lam, C. & Morsut, L. Synthetic development: building mammalian multicellular structures with artificial genetic programs. *Curr. Opin. Biotechnol.* **59**, 130–140 (2019).

12 Johnson, M. B., March, A. R. & Morsut, L. Engineering multicellular systems: Using synthetic biology to control tissue self-organization. *Curr. Opin. Biomed. Eng.* **4**, 163–173 (2017).

13 Ho, C. & Morsut, L. Novel synthetic biology approaches for developmental systems. *Stem Cell Rep* **16**, 1051-1064 (2021). https://doi.org:10.1016/j.stemcr.2021.04.007

14 Hoffman, T. *et al.* Synthetic Biology and Tissue Engineering: Toward Fabrication of Complex and Smart Cellular Constructs. *Advanced Functional Materials* **30**, 1909882 (2020). https://doi.org:10.1002/adfm.201909882

15 Aydin, O. *et al.* Principles for the design of multicellular engineered living systems. *APL Bioeng* **6**, 010903 (2022). https://doi.org:10.1063/5.0076635

16 Ebrahimkhani, M. R. & Ebisuya, M. Synthetic developmental biology: build and control multicellular systems. *Curr Opin Chem Biol* **52**, 9-15 (2019). https://doi.org:10.1016/j.cbpa.2019.04.006

17 Toda, S., Frankel, N. W. & Lim, W. A. Engineering cell-cell communication networks: programming multicellular behaviors. *Curr Opin Chem Biol* **52**, 31-38 (2019). https://doi.org:10.1016/j.cbpa.2019.04.020

18 Gumuskaya, G. *Form From Within: Scaling Up Self-Constructing Biological Architectures through a Novel Application of Synthetic Morphogenesis. (Massachusetts Institute of Technology, 2018)* M.S. thesis, Massachusetts Institute of Technologuy, (2018).

19 Morsut, L. *et al.* Engineering Customized Cell Sensing and Response Behaviors Using Synthetic Notch Receptors. *Cell* **164**, 780-791 (2016). https://doi.org:10.1016/j.cell.2016.01.012

20 Toda, S., Blauch, L. R., Tang, S. K. Y., Morsut, L. & Lim, W. A. Programming self-organizing multicellular structures with synthetic cell-cell signaling. *Science* **361**, 156-162 (2018). https://doi.org:10.1126/science.aat0271
21 Toda, S. *et al.* Engineering synthetic morphogen systems that can program multicellular patterning. *Science* **370**, 327-331 (2020). https://doi.org:10.1126/science.abc0033
22 Karig, D. *et al.* Stochastic Turing patterns in a synthetic bacterial population. *Proc Natl Acad Sci U S A* **115**, 6572-6577 (2018). https://doi.org:10.1073/pnas.1720770115
23 Gumuskaya, G. Multimaterial bioprinting—minus the printer: Synthetic bacterial patterning with UV-responsive genetic circuits. *Int. J. Archit. Comput.* **19**, 121–141 (2021).
24 Basu, S., Gerchman, Y., Collins, C. H., Arnold, F. H. & Weiss, R. A synthetic multicellular system for programmed pattern formation. *Nature* **434**, 1130-1134 (2005). https://doi.org:10.1038/nature03461
25 Basu, S., Mehreja, R., Thiberge, S., Chen, M. T. & Weiss, R. Spatiotemporal control of gene expression with pulse-generating networks. *Proc Natl Acad Sci U S A* **101**, 6355-6360 (2004). https://doi.org:10.1073/pnas.0307571101
26 Ricotti, L. *et al.* Biohybrid actuators for robotics: A review of devices actuated by living cells. *Sci Robot* **2**, eaaq0495 (2017). https://doi.org:10.1126/scirobotics.aaq0495
27 Menciassi, A., Takeuchi, S. & Kamm, R. D. Biohybrid systems: Borrowing from nature to make better machines. *APL Bioeng.* **4**, 020401 (2020).
28 Sakar, M. S. *et al.* Formation and optogenetic control of engineered 3D skeletal muscle bioactuators. *Lab Chip* **12**, 4976-4985 (2012). https://doi.org:10.1039/c2lc40338b
29 Chan, V. *et al.* Development of miniaturized walking biological machines. *Sci Rep* **2**, 857 (2012). https://doi.org:10.1038/srep00857
30 Nawroth, J. C. *et al.* A tissue-engineered jellyfish with biomimetic propulsion. *Nat Biotechnol* **30**, 792-797 (2012). https://doi.org:10.1038/nbt.2269
31 Raman, R. *et al.* Optogenetic skeletal muscle-powered adaptive biological machines. *Proc Natl Acad Sci U S A* **113**, 3497-3502 (2016). https://doi.org:10.1073/pnas.1516139113
32 Park, S. J. *et al.* Phototactic guidance of a tissue-engineered soft-robotic ray. *Science* **353**, 158-162 (2016). https://doi.org:10.1126/science.aaf4292
33 Zhang, H. *et al.* Dual-responsive biohybrid neutrobots for active target delivery. *Sci Robot* **6** (2021). https://doi.org:10.1126/scirobotics.aaz9519
34 Hwang, J. & Choi, H. Neutrobots smuggle drugs across biological barriers. *Sci Robot* **6** (2021). https://doi.org:10.1126/scirobotics.abh0286
35 Aydin, O. *et al.* Neuromuscular actuation of biohybrid motile bots. *Proc Natl Acad Sci U S A* **116**, 19841-19847 (2019). https://doi.org:10.1073/pnas.1907051116
36 Williams, B. J., Anand, S. V., Rajagopalan, J. & Saif, M. T. A self-propelled biohybrid swimmer at low Reynolds number. *Nat Commun* **5**, 3081 (2014). https://doi.org:10.1038/ncomms4081
37 Feinberg, A. W. *et al.* Muscular thin films for building actuators and powering devices. *Science* **317**, 1366-1370 (2007). https://doi.org:10.1126/science.1146885
38 Xi, J., Schmidt, J. J. & Montemagno, C. D. Self-assembled microdevices driven by muscle. *Nat Mater* **4**, 180-184 (2005). https://doi.org:10.1038/nmat1308
39 Huang, G. *et al.* Cell-based intelligent micro/nanorobots for precise regulation and active biotherapy. *Matter* https://doi.org:10.1016/j.matt.2023.09.013
40 Kriegman, S., Blackiston, D., Levin, M. & Bongard, J. Kinematic self-replication in reconfigurable organisms. *Proc Natl Acad Sci U S A* **118**, e2112672118 (2021). https://doi.org:10.1073/pnas.2112672118
41 Blackiston, D. *et al.* A cellular platform for the development of synthetic living machines. *Sci Robot* **6**, eabf1571 (2021). https://doi.org:10.1126/scirobotics.abf1571

42 Kriegman, S., Blackiston, D., Levin, M. & Bongard, J. A scalable pipeline for designing reconfigurable organisms. *Proc Natl Acad Sci U S A* **117**, 1853-1859 (2020). https://doi.org:10.1073/pnas.1910837117
43 Doursat, R., Sayama, H. & Michel, O. in *Morphogenetic Engineering* (eds René Doursat, Hiroki Sayama, & Olivier Michel) 1-24 (Springer Berlin Heidelberg, 2012).
44 Boselli, F., Jullien, J., Lauga, E. & Goldstein, R. E. Fluid Mechanics of Mosaic Ciliated Tissues. *Phys Rev Lett* **127**, 198102 (2021). https://doi.org:10.1103/PhysRevLett.127.198102
45 Dye, B. R. *et al.* In vitro generation of human pluripotent stem cell derived lung organoids. *Elife* **4** (2015). https://doi.org:10.7554/eLife.05098
46 Stroulios, G. *et al.* Apical-out airway organoids as a platform for studying viral infections and screening for antiviral drugs. *Sci Rep* **12**, 7673 (2022). https://doi.org:10.1038/s41598-022-11700-z
47 Wijesekara, P. *et al.* Engineering rotating apical-out airway organoid for assessing respiratory cilia motility. *iScience* **25**, 104730 (2022). https://doi.org:10.1016/j.isci.2022.104730
48 Boecking, C. A. *et al.* A simple method to generate human airway epithelial organoids with externally orientated apical membranes. *Am J Physiol Lung Cell Mol Physiol* **322**, L420-L437 (2022). https://doi.org:10.1152/ajplung.00536.2020
49 Deslee, G. *et al.* Bronchial epithelial spheroids: an alternative culture model to investigate epithelium inflammation-mediated COPD. *Respir Res* **8**, 86 (2007). https://doi.org:10.1186/1465-9921-8-86
50 Hild, M. & Jaffe, A. B. Production of 3-D Airway Organoids From Primary Human Airway Basal Cells and Their Use in High-Throughput Screening. *Curr Protoc Stem Cell Biol* **37**, IE 9 1-IE 9 15 (2016). https://doi.org:10.1002/cpsc.1
51 Wijesekara, P., Patel, K. Z., Otto, E. L., Campbell, P. G. & Ren, X. Protocol to engineer apical-out airway organoids using suspension culture of human airway basal stem cell aggregates. *STAR Protoc* **4**, 102154 (2023). https://doi.org:10.1016/j.xpro.2023.102154
52 Sachs, N. *et al.* Long-term expanding human airway organoids for disease modeling. *EMBO J* **38** (2019). https://doi.org:10.15252/embj.2018100300
53 Wu, X., Peters-Hall, J. R., Bose, S., Pena, M. T. & Rose, M. C. Human bronchial epithelial cells differentiate to 3D glandular acini on basement membrane matrix. *Am J Respir Cell Mol Biol* **44**, 914-921 (2011). https://doi.org:10.1165/rcmb.2009-0329OC
54 Zhou, J. *et al.* Differentiated human airway organoids to assess infectivity of emerging influenza virus. *Proc Natl Acad Sci U S A* **115**, 6822-6827 (2018). https://doi.org:10.1073/pnas.1806308115
55 Barkauskas, C. E. *et al.* Lung organoids: current uses and future promise. *Development* **144**, 986-997 (2017). https://doi.org:10.1242/dev.140103
56 Co, J. Y. *et al.* Controlling Epithelial Polarity: A Human Enteroid Model for Host-Pathogen Interactions. *Cell Rep* **26**, 2509-2520 e2504 (2019). https://doi.org:10.1016/j.celrep.2019.01.108
57 Soofi, S. S., Last, J. A., Liliensiek, S. J., Nealey, P. F. & Murphy, C. J. The elastic modulus of Matrigel as determined by atomic force microscopy. *J Struct Biol* **167**, 216-219 (2009). https://doi.org:10.1016/j.jsb.2009.05.005
58 Yedgar, S. *et al.* Viscosity of Culture-Medium as a Regulator of Synthesis and Secretion of Very Low-Density Lipoproteins by Cultured-Hepatocytes. *J Biol Chem* **257**, 2188-2192 (1982). https://doi.org:10.1016/S0021-9258(18)34904-4.
59 Bennett, M. *et al.* Molecular clutch drives cell response to surface viscosity. *Proc Natl Acad Sci U S A* **115**, 1192-1197 (2018). https://doi.org:10.1073/pnas.1710653115
60 Firestone, A. J. *et al.* Small-molecule inhibitors of the AAA+ ATPase motor cytoplasmic dynein. *Nature* **484**, 125-129 (2012). https://doi.org:10.1038/nature10936

61 Reddy, G. S., Mukhopadhyay, A. G. & Dey, C. S. Characterization of ciliobrevin A mediated dynein ATPase inhibition on flagellar motility of Leishmania donovani. *Mol Biochem Parasitol* **214**, 75-81 (2017). https://doi.org:10.1016/j.molbiopara.2017.04.003
62 Abramson, C. I. & Levin, M. Behaviorist approaches to investigating memory and learning: A primer for synthetic biology and bioengineering. *Commun Integr Biol* **14**, 230-247 (2021). https://doi.org:10.1080/19420889.2021.2005863
63 Wiens, J. J. Character analysis in morphological phylogenetics: problems and solutions. *Syst Biol* **50**, 689-699 (2001). https://doi.org:10.1080/106351501753328811
64 Thiele, K. The Holy Grail of the Perfect Character: The Cladistic Treatment of Morphometric Data. *Cladistics* **9**, 275-304 (1993). https://doi.org:10.1111/j.1096-0031.1993.tb00226.x
65 Marramà, G. & Kriwet, J. Principal component and discriminant analyses as powerful tools to support taxonomic identification and their use for functional and phylogenetic signal detection of isolated fossil shark teeth. *PLoS One* **12**, e0188806 (2017). https://doi.org:10.1371/journal.pone.0188806
66 Larsen, P. A., Marchan-Rivadeneira, M. R. & Baker, R. J. Natural hybridization generates mammalian lineage with species characteristics. *Proc Natl Acad Sci U S A* **107**, 11447-11452 (2010). https://doi.org:10.1073/pnas.1000133107
67 Clemmensen, K. E. & Michelsen, A. Integrated long-term responses of an arctic–alpine willow and associated ectomycorrhizal fungi to an altered environment. *Canadian Journal of Botany* **84**, 831-843 (2006). https://doi.org:10.1139/b06-039
68 Santos, M. A. B. d. *et al.* Morphological Diversity of Springtails in Land Use Systems. *Revista Brasileira de Ciência do Solo* **42** (2018). https://doi.org:10.1590/18069657rbcs20170277
69 Masiello, M. G., Verna, R., Cucina, A. & Bizzarri, M. Physical constraints in cell fate specification. A case in point: Microgravity and phenotypes differentiation. *Prog Biophys Mol Biol* **134**, 55-67 (2018). https://doi.org:10.1016/j.pbiomolbio.2018.01.001
70 Sato, A. Chaperones, Canalization, and Evolution of Animal Forms. *Int J Mol Sci* **19**, E3029 (2018). https://doi.org:10.3390/ijms19103029
71 Townsend, G., Hughes, T., Bockmann, M., Smith, R. & Brook, A. How Studies of Twins Can Inform Our Understanding of Dental Morphology. *Comparative Dental Morphology* **13**, 136-+ (2009).
72 Fooladi, H., Moradi, P., Sharifi-Zarchi, A. & Hosein Khalaj, B. Enhanced Waddington landscape model with cell-cell communication can explain molecular mechanisms of self-organization. *Bioinformatics* **35**, 4081-4088 (2019). https://doi.org:10.1093/bioinformatics/btz201
73 Levin, M. & Palmer, A. R. Left-right patterning from the inside out: widespread evidence for intracellular control. *Bioessays* **29**, 271-287 (2007). https://doi.org:10.1002/bies.20545
74 Namigai, E. K., Kenny, N. J. & Shimeld, S. M. Right across the tree of life: the evolution of left-right asymmetry in the Bilateria. *Genesis* **52**, 458-470 (2014). https://doi.org:10.1002/dvg.22748
75 Lipson, H. & Pollack, J. B. Automatic design and manufacture of robotic lifeforms. *Nature* **406**, 974-978 (2000). https://doi.org:10.1038/35023115
76 Cory, G. Scratch-wound assay. *Methods Mol Biol* **769**, 25-30 (2011). https://doi.org:10.1007/978-1-61779-207-6_2
77 Martinotti, S. & Ranzato, E. Scratch Wound Healing Assay. *Methods Mol Biol* **2109**, 225-229 (2020). https://doi.org:10.1007/7651_2019_259
78 Cairns, D. M. *et al.* Expandable and Rapidly Differentiating Human Induced Neural Stem Cell Lines for Multiple Tissue Engineering Applications. *Stem Cell Reports* **7**, 557-570 (2016). https://doi.org:10.1016/j.stemcr.2016.07.017
79 Reid, C. R. *et al.* Army ants dynamically adjust living bridges in response to a cost-benefit trade-off. *Proc Natl Acad Sci U S A* **112**, 15113-15118 (2015). https://doi.org:10.1073/pnas.1512241112

80 Kamm, R. D. *et al.* Perspective: The promise of multi-cellular engineered living systems. *APL Bioeng* **2**, 040901 (2018). https://doi.org:10.1063/1.5038337
81 Davies, J. A. & Glykofrydis, F. Engineering pattern formation and morphogenesis. *Biochem Soc Trans* **48**, 1177-1185 (2020). https://doi.org:10.1042/BST20200013
82 Davies, J. & Levin, M. Synthetic morphology via active and agential matter. *OSF Preprints* (2022). https://doi.org:10.31219/osf.io/xrv8h
83 Velazquez, J. J., Su, E., Cahan, P. & Ebrahimkhani, M. R. Programming Morphogenesis through Systems and Synthetic Biology. *Trends Biotechnol* **36**, 415-429 (2018). https://doi.org:10.1016/j.tibtech.2017.11.003
84 Newman, S. A. 'Biogeneric' developmental processes: drivers of major transitions in animal evolution. *Philos. Trans. R. Soc. B Biol. Sci.* **371**, 20150443 (2016).
85 Beloussov, L. V. Mechanically based generative laws of morphogenesis. *Physical biology* **5**, 015009 (2008). https://doi.org:S1478-3975(08)62359-6 [pii]

10.1088/1478-3975/5/1/015009
86 Davidson, L. A. Epithelial machines that shape the embryo. *Trends Cell Biol* **22**, 82-87 (2012). https://doi.org:10.1016/j.tcb.2011.10.005
87 Miller, C. J. & Davidson, L. A. The interplay between cell signalling and mechanics in developmental processes. *Nat Rev Genet* **14**, 733-744 (2013). https://doi.org:10.1038/nrg3513
88 Newman, S. A. Inherency and homomorphy in the evolution of development. *Curr Opin Genet Dev* **57**, 1-8 (2019). https://doi.org:10.1016/j.gde.2019.05.006
89 Newman, S. A. Inherency of Form and Function in Animal Development and Evolution. *Front Physiol* **10**, 702 (2019). https://doi.org:10.3389/fphys.2019.00702
90 Ingber, D. E. Human organs-on-chips for disease modelling, drug development and personalized medicine. *Nat Rev Genet* **23**, 467-491 (2022). https://doi.org:10.1038/s41576-022-00466-9
91 Baluška, F. & Levin, M. On Having No Head: Cognition throughout Biological Systems. *Front Psychol* **7**, 902 (2016). https://doi.org:10.3389/fpsyg.2016.00902
92 Davies, J. A. & Cachat, E. Synthetic biology meets tissue engineering. *Biochem Soc Trans* **44**, 696-701 (2016). https://doi.org:10.1042/BST20150289
93 Clawson, W. P. & Levin, M. Endless forms most beautiful 2.0: teleonomy and the bioengineering of chimaeric and synthetic organisms. *Biological Journal of the Linnean Society*, blac073 (2022). https://doi.org:10.1093/biolinnean/blac073
94 Kauffman, S. A. *The Origins of Order: Self-Organization and Selection in Evolution*. (Oxford University Press, 1993).
95 Roli, A. & Kauffman, S. A. Emergence of Organisms. *Entropy (Basel)* **22**, 1163 (2020). https://doi.org:10.3390/e22101163
96 Nagode, M. & Fajdiga, M. The REBMIX Algorithm and the Univariate Finite Mixture Estimation. *Communications in Statistics - Theory and Methods* **40**, 876-892 (2011). https://doi.org:10.1080/03610920903480890
97 Tabor, J. & Spurek, P. Cross-entropy clustering. *Pattern Recognition* **47**, 3046-3059 (2014). https://doi.org:10.1016/j.patcog.2014.03.006
98 Tabor, J., Spurek, P., Kamieniecki, K., Śmieja, M. & Misztal, K. Introduction to Cross-Entropy Clustering The R Package CEC. *arXiv* (2015). https://doi.org:10.48550/arXiv.1508.04559
99 Hansen, J. N., Rassmann, S., Stuven, B., Jurisch-Yaksi, N. & Wachten, D. CiliaQ: a simple, open-source software for automated quantification of ciliary morphology and fluorescence in 2D, 3D, and 4D images. *Eur Phys J E Soft Matter* **44**, 18 (2021). https://doi.org:10.1140/epje/s10189-021-00031-y

100 Gombin, J., Vaidyanathan, R. & Agafonkin, V. *A Very Fast 2D Concave Hull Algorithm*, < https://joelgombin.github.io/concaveman/> (2017).
101 Hahsler, M., Piekenbrock, M. & Doran, D. dbscan: Fast Density-Based Clustering with R. *Journal of Statistical Software* **91**, 1-30 (2019). https://doi.org:10.18637/jss.v091.i01
102 Maechler, M., Rousseeuw, P., Struyf, A., Hubert, M. & Hornik, K. *cluster: Cluster Analysis Basics and Extensions*, <https://CRAN.R-project.org/package=cluster> (2022).
103 Lafarge, T. & Pateiro-Lopez, B. *alphashape3d: Implementation of the 3D Alpha-Shape for the Reconstruction of 3D Sets from a Point Cloud*, <https://CRAN.R-project.org/package=alphashape3d> (2020).
104 Oles, A. *RBioFormats: R interface to Bio-Formats version 0.0.75*, <https://rdrr.io/github/aoles/RBioFormats/.> (2015).
105 Garnier, S. & Muschelli, J. *Rvision - A computer vision library for R*, <https://swarm-lab.github.io/Rvision/> (2022).
106 Davies, J. A. Machines for living in: Connections and contrasts between designed architecture and the development of living forms. *Architectural Research Quarterly* **20**, 45-50 (2016). https://doi.org:10.1017/S1359135516000154
107 Davies, J. A. Synthetic morphology: prospects for engineered, self-constructing anatomies: Synthetic morphology, J. A. Davies. *Journal of Anatomy* **212**, 707-719 (2008). https://doi.org:10.1111/j.1469-7580.2008.00896.x
108 Teague, B. P., Guye, P. & Weiss, R. Synthetic Morphogenesis. *Cold Spring Harbor Perspectives in Biology* **8**, a023929 (2016). https://doi.org:10.1101/cshperspect.a023929
109 Johnson, M. B., March, A. R. & Morsut, L. Engineering multicellular systems: Using synthetic biology to control tissue self-organization. *Current Opinion in Biomedical Engineering* **4**, 163-173 (2017). https://doi.org:10.1016/j.cobme.2017.10.008
110 Toda, S., Brunger, J. M. & Lim, W. A. Synthetic development: learning to program multicellular self-organization. *Current Opinion in Systems Biology* **14**, 41-49 (2019). https://doi.org:10.1016/j.coisb.2019.02.008
111 Davies, J. Using synthetic biology to explore principles of development. *Development* **144**, 1146-1158 (2017). https://doi.org:10.1242/dev.144196
112 Toda, S., Blauch, L. R., Tang, S. K. Y., Morsut, L. & Lim, W. A. Programming self-organizing multicellular structures with synthetic cell-cell signaling. *Science*, eaat0271 (2018). https://doi.org:10.1126/science.aat0271
113 Wauford, N. *et al.* Synthetic symmetry breaking and programmable multicellular structure formation. *Cell Syst* **14**, 806-818 e805 (2023). https://doi.org:10.1016/j.cels.2023.08.001
114 Gumuskaya, G. *et al.* Motile Living Biobots Self-Construct from Adult Human Somatic Progenitor Seed Cells. *Adv Sci (Weinh)*, e2303575 (2023). https://doi.org:10.1002/advs.202303575
115 Ricotti, L. *et al.* Biohybrid actuators for robotics: A review of devices actuated by living cells. *Science Robotics* **2**, eaaq0495 (2017). https://doi.org:10.1126/scirobotics.aaq0495
116 Menciassi, A., Takeuchi, S. & Kamm, R. D. Biohybrid systems: Borrowing from nature to make better machines. *APL Bioengineering* **4**, 020401 (2020). https://doi.org:10.1063/5.0014918
117 Sakar, M. S. *et al.* Formation and optogenetic control of engineered 3D skeletal muscle bioactuators. *Lab on a Chip* **12**, 4976 (2012). https://doi.org:10.1039/c2lc40338b
118 Chan, V. *et al.* Development of Miniaturized Walking Biological Machines. *Scientific Reports* **2**, 857 (2012). https://doi.org:10.1038/srep00857
119 Nawroth, J. C. *et al.* A tissue-engineered jellyfish with biomimetic propulsion. *Nature Biotechnology* **30**, 792-797 (2012). https://doi.org:10.1038/nbt.2269
120 Feinberg, A. W. *et al.* Muscular Thin Films for Building Actuators and Powering Devices. *Science* **317**, 1366-1370 (2007). https://doi.org:10.1126/science.1146885

121 Kriegman, S., Blackiston, D., Levin, M. & Bongard, J. Kinematic self-replication in reconfigurable organisms. *Proceedings of the National Academy of Sciences* **118**, e2112672118 (2021). https://doi.org:10.1073/pnas.2112672118
122 Blackiston, D. *et al.* A cellular platform for the development of synthetic living machines. *Science Robotics* **6**, eabf1571 (2021). https://doi.org:10.1126/scirobotics.abf1571
123 Kriegman, S., Blackiston, D., Levin, M. & Bongard, J. A scalable pipeline for designing reconfigurable organisms. *Proceedings of the National Academy of Sciences* **117**, 1853-1859 (2020). https://doi.org:10.1073/pnas.1910837117
124 Basu, S., Mehreja, R., Thiberge, S., Chen, M.-T. & Weiss, R. Spatiotemporal control of gene expression with pulse-generating networks. *Proc. Natl. Acad. Sci. U. S. A.* **101**, 6355-6360 (2004). https://doi.org:10.1073/pnas.0307571101
125 Basu, S., Gerchman, Y., Collins, C. H., Arnold, F. H. & Weiss, R. A synthetic multicellular system for programmed pattern formation. *Nature* **434**, 1130–1134 (2005).
126 Matsuda, M., Koga, M., Woltjen, K., Nishida, E. & Ebisuya, M. Synthetic lateral inhibition governs cell-type bifurcation with robust ratios. *Nature Communications* **6** (2015). https://doi.org:10.1038/ncomms7195
127 Cachat, E. *et al.* 2- and 3-dimensional synthetic large-scale de novo patterning by mammalian cells through phase separation. *Scientific Reports* **6** (2016). https://doi.org:10.1038/srep20664
128 Guye, P. *et al.* Genetically engineering self-organization of human pluripotent stem cells into a liver bud-like tissue using Gata6. *Nature Communications* **7** (2016). https://doi.org:10.1038/ncomms10243
129 Morsut, L. *et al.* Engineering Customized Cell Sensing and Response Behaviors Using Synthetic Notch Receptors. *Cell* **164**, 780-791 (2016). https://doi.org:10.1016/j.cell.2016.01.012
130 Karig, D. *et al.* Stochastic Turing patterns in a synthetic bacterial population. *Proceedings of the National Academy of Sciences* **115**, 6572-6577 (2018). https://doi.org:10.1073/pnas.1720770115
131 Glock, P. *et al.* Stationary Patterns in a Two-Protein Reaction-Diffusion System. *ACS Synthetic Biology* **8**, 148-157 (2019). https://doi.org:10.1021/acssynbio.8b00415
132 Gumuskaya, G. Multimaterial bioprinting—minus the printer: Synthetic bacterial patterning with UV-responsive genetic circuits. *International Journal of Architectural Computing* **19**, 121-141 (2021). https://doi.org:10.1177/1478077120963373
133 Sia, S. K., Gillette, B. M. & Yang, G. J. Synthetic tissue biology: Tissue engineering meets synthetic biology. *Birth Defects Research Part C: Embryo Today: Reviews* **81**, 354-361 (2007). https://doi.org:10.1002/bdrc.20105
134 Elowitz, M. & Lim, W. A. Build life to understand it. *Nature* **468**, 889-890 (2010). https://doi.org:10.1038/468889a
135 Davies, J. A. & Cachat, E. Synthetic biology meets tissue engineering. *Biochemical Society Transactions* **44**, 696-701 (2016). https://doi.org:10.1042/BST20150289
136 Velazquez, J. J., Su, E., Cahan, P. & Ebrahimkhani, M. R. Programming Morphogenesis through Systems and Synthetic Biology. *Trends in Biotechnology* **36**, 415-429 (2018). https://doi.org:10.1016/j.tibtech.2017.11.003
137 Ebrahimkhani, M. R. & Ebisuya, M. Synthetic developmental biology: build and control multicellular systems. *Current Opinion in Chemical Biology* **52**, 9-15 (2019). https://doi.org:10.1016/j.cbpa.2019.04.006
138 Luo, N., Wang, S. & You, L. Synthetic Pattern Formation. *Biochemistry* **58**, 1478-1483 (2019). https://doi.org:10.1021/acs.biochem.8b01242
139 Santorelli, M., Lam, C. & Morsut, L. Synthetic development: building mammalian multicellular structures with artificial genetic programs. *Current Opinion in Biotechnology* **59**, 130-140 (2019). https://doi.org:10.1016/j.copbio.2019.03.016

140 Toda, S., Frankel, N. W. & Lim, W. A. Engineering cell–cell communication networks: programming multicellular behaviors. *Current Opinion in Chemical Biology* **52**, 31-38 (2019). https://doi.org:10.1016/j.cbpa.2019.04.020
141 Davies, J. A. & Glykofrydis, F. Engineering pattern formation and morphogenesis. *Biochemical Society Transactions* **48**, 1177-1185 (2020). https://doi.org:10.1042/BST20200013
142 Hoffman, T. *et al.* Synthetic Biology and Tissue Engineering: Toward Fabrication of Complex and Smart Cellular Constructs. *Advanced Functional Materials* **30**, 1909882 (2020). https://doi.org:10.1002/adfm.201909882
143 Aydin, O. *et al.* Principles for the design of multicellular engineered living systems. *APL Bioengineering* **6**, 010903 (2022). https://doi.org:10.1063/5.0076635
144 Zarkesh, I. *et al.* Synthetic developmental biology: Engineering approaches to guide multicellular organization. *Stem Cell Reports* **17**, 715-733 (2022). https://doi.org:10.1016/j.stemcr.2022.02.004
145 Doursat, R., Sayama, H. & Michel, O. A review of morphogenetic engineering. *Natural Computing* **12**, 517-535 (2013). https://doi.org:10.1007/s11047-013-9398-1
146 Dar, R. D. & Weiss, R. Perspective: Engineering noise in biological systems towards predictive stochastic design. *APL Bioengineering* **2**, 020901 (2018). https://doi.org:10.1063/1.5025033
147 Slusarczyk, A. L., Lin, A. & Weiss, R. Foundations for the design and implementation of synthetic genetic circuits. *Nature Reviews Genetics* **13**, 406-420 (2012). https://doi.org:10.1038/nrg3227
148 Weiss, R. & Panke, S. Synthetic biology—paths to moving forward. *Current Opinion in Biotechnology* **20**, 447-448 (2009). https://doi.org:10.1016/j.copbio.2009.09.007
149 Purnick, P. E. M. & Weiss, R. The second wave of synthetic biology: from modules to systems. *Nature Reviews Molecular Cell Biology* **10**, 410-422 (2009). https://doi.org:10.1038/nrm2698
150 Dhar, P. K. & Weiss, R. Enabling the new biology of the 21st century. *Systems and Synthetic Biology* **1**, 1-2 (2007). https://doi.org:10.1007/s11693-006-9000-6
151 Andrianantoandro, E., Basu, S., Karig, D. K. & Weiss, R. Synthetic biology: new engineering rules for an emerging discipline. *Molecular Systems Biology* **2** (2006). https://doi.org:10.1038/msb4100073
152 Sommer, R. J. Phenotypic Plasticity: From Theory and Genetics to Current and Future Challenges. *Genetics* **215**, 1-13 (2020). https://doi.org:10.1534/genetics.120.303163
153 Kelly, S. A., Panhuis, T. M. & Stoehr, A. M. Phenotypic plasticity: molecular mechanisms and adaptive significance. *Compr Physiol* **2**, 1417-1439 (2012). https://doi.org:10.1002/cphy.c110008
154 West-Eberhard, M. J. Evolution in the light of developmental and cell biology, and vice versa. *Proc Natl Acad Sci U S A* **95**, 8417-8419 (1998).
155 West-Eberhard, M. J. Developmental plasticity and the origin of species differences. *Proc Natl Acad Sci U S A* **102 Suppl 1**, 6543-6549 (2005). https://doi.org:10.1073/pnas.0501844102
156 Bedzhov, I., Graham, S. J., Leung, C. Y. & Zernicka-Goetz, M. Developmental plasticity, cell fate specification and morphogenesis in the early mouse embryo. *Philos Trans R Soc Lond B Biol Sci* **369** (2014). https://doi.org:10.1098/rstb.2013.0538
157 Martinez Arias, A., Nichols, J. & Schroter, C. A molecular basis for developmental plasticity in early mammalian embryos. *Development* **140**, 3499-3510 (2013). https://doi.org:10.1242/dev.091959
158 Davies, J. A. *Mechanisms of morphogenesis*. Second edition edn, (Elsevier/AP, 2013).
159 Pitcairn, E. & McLaughlin, K. A. Bioelectric signaling coordinates patterning decisions during embryogenesis. *Trends in Developmental Biology* **9** (2016).
160 Levin, M. Bioelectric signaling: Reprogrammable circuits underlying embryogenesis, regeneration, and cancer. *Cell* **184**, 1971-1989 (2021). https://doi.org:10.1016/j.cell.2021.02.034

161 Ollé-Vila, A., Duran-Nebreda, S., Conde-Pueyo, N., Montañez, R. & Solé, R. A morphospace for synthetic organs and organoids: the possible and the actual. *Integrative Biology* **8**, 485-503 (2016). https://doi.org:10.1039/C5IB00324E
162 McGhee, G. R. *The geometry of evolution : adaptive landscapes and theoretical morphospaces*. (Cambridge University Press, 2007).
163 Stone, J. R. The spirit of D'arcy Thompson dwells in empirical morphospace. *Math Biosci* **142**, 13-30 (1997).
164 Olle-Vila, A., Duran-Nebreda, S., Conde-Pueyo, N., Montanez, R. & Sole, R. A morphospace for synthetic organs and organoids: the possible and the actual. *Integr Biol (Camb)* **8**, 485-503 (2016). https://doi.org:10.1039/c5ib00324e
165 Raup, D. M. & Michelson, A. Theoretical Morphology of the Coiled Shell. *Science* **147**, 1294-1295 (1965). https://doi.org:10.1126/science.147.3663.1294
166 Wijesekara, P. *et al.* Engineering Rotating Apical-Out Airway Organoid for Assessing Respiratory Cilia Motility. (2022). https://doi.org:10.1101/2022.01.15.476455
167 Stroulios, G. *et al.* Apical-out airway organoids as a platform for studying viral infections and screening for antiviral drugs. *Scientific Reports* **12**, 7673 (2022). https://doi.org:10.1038/s41598-022-11700-z
168 Boecking, C. A. *et al.* A simple method to generate human airway epithelial organoids with externally orientated apical membranes. *American Journal of Physiology-Lung Cellular and Molecular Physiology* **322**, L420-L437 (2022). https://doi.org:10.1152/ajplung.00536.2020
169 Tordoff, J. *et al.* Incomplete Cell Sorting Creates Engineerable Structures with Long-Term Stability. *Cell Reports Physical Science* **2** (2021). https://doi.org:10.1016/j.xcrp.2020.100305
170 Hasan, S., Sebo, P. & Osicka, R. A guide to polarized airway epithelial models for studies of host–pathogen interactions. *The FEBS Journal* **285**, 4343-4358 (2018). https://doi.org:10.1111/febs.14582
171 Jain, R. *et al.* Temporal relationship between primary and motile ciliogenesis in airway epithelial cells. *Am J Respir Cell Mol Biol* **43**, 731-739 (2010). https://doi.org:10.1165/rcmb.2009-0328OC
172 Wu, X., Peters-Hall, J. R., Bose, S., Peña, M. T. & Rose, M. C. Human Bronchial Epithelial Cells Differentiate to 3D Glandular Acini on Basement Membrane Matrix. *American Journal of Respiratory Cell and Molecular Biology* **44**, 914-921 (2011). https://doi.org:10.1165/rcmb.2009-0329OC
173 Hild, M. & Jaffe, A. B. Production of 3-D Airway Organoids From Primary Human Airway Basal Cells and Their Use in High-Throughput Screening. *Current Protocols in Stem Cell Biology* **37** (2016). https://doi.org:10.1002/cpsc.1
174 Zhou, J. *et al.* Differentiated human airway organoids to assess infectivity of emerging influenza virus. *Proceedings of the National Academy of Sciences* **115**, 6822-6827 (2018). https://doi.org:10.1073/pnas.1806308115
175 Sachs, N. *et al.* Long-term expanding human airway organoids for disease modeling. *The EMBO Journal* **38** (2019). https://doi.org:10.15252/embj.2018100300
176 Co, J. Y. *et al.* Controlling Epithelial Polarity: A Human Enteroid Model for Host-Pathogen Interactions. *Cell Reports* **26**, 2509-2520.e2504 (2019). https://doi.org:10.1016/j.celrep.2019.01.108
177 Newman, S. A. Inherency of Form and Function in Animal Development and Evolution. *Frontiers in Physiology* **10** (2019).
178 Newman, S. A. Inherency and homomorphy in the evolution of development. *Current Opinion in Genetics & Development* **57**, 1-8 (2019). https://doi.org:10.1016/j.gde.2019.05.006

179 Newman, S. A. ‘Biogeneric’ developmental processes: drivers of major transitions in animal evolution. *Philosophical Transactions of the Royal Society B: Biological Sciences* **371**, 20150443 (2016). https://doi.org:10.1098/rstb.2015.0443